ANNÉE 2013

THÈSE / UNIVERSITÉ DE RENNES 1
sous le sceau de l'Université Européenne de Bretagne

pour le grade de

DOCTEUR DE L'UNIVERSITÉ DE RENNES 1

Mention : Traitment du Signal et Télécommunications

Ecole doctorale Mathematiques, Informatique, Signal, Electronique et Télécommunications

présentée par

Qian WANG

Préparée à l'unité de recherche LTSI – INSERM UMR 1099
Laboratoire Traitement du Signal et de l'Image

Traitement et exploration d'images TDM pour l'évaluation des bioprothèses valvulaires aortiques

Thèse soutenue à Rennes
le 09 Décembre 2013

devant le jury composé de :

Christophe LOHOU
Professeur, Université d'Auvergne / *rapporteur*

Alain LALANDE
MCU-PH HDR Université de Bourgogne / *rapporteur*

Mireille GARREAU
Professeur, Université de Rennes 1 / *examinateur*

Huazhong SHU
Professeur, Southeast University / *examinateur*

Pascal HAIGRON
Professeur, Université de Rennes 1/ *directeur de thèse*

ANNÉE 2013

ANNÉE 2013

ANNÉE 2013

Traitement et exploration d'images TDM pour l'évaluation des bioprothèses valvulaires aortiques

Résumé

Le but de cette étude est d'évaluer la faisabilité de l'analyse tomodensitométrique 3D des bioprothèses aortiques pour faciliter leur évaluation morphologique durant le suivi et d'aider la sélection de cas et améliorer la planification d'une procédure valve-in-valve. Le challenge était représenté par le rehaussement des feuillets valvulaires, en raison d'images très bruitées.

Un angio-scanner synchronisé était réalisé chez des patients porteurs d'une bioprotèses aortique dégénérée avant réintervention (images in-vivo). Différentes méthodes pour la réduction du bruit étaient proposées. La reconstruction tridimensionnelle des bioprothèses était réalisée en utilisant des méthodes de segmentation de régions par "sticks". Après réopération ces méthodes étaient appliquées aux images scanner des bioprothèses explantées (images ex-vivo) et utilisées comme référence.

La réduction du bruit obtenue par le filtre stick modifié montrait meilleurs résultats en rapport signal/bruit en comparaison aux filtres de diffusion anisotropique. Toutes les méthodes de segmentation ont permis une reconstruction 3D des feuillets. L'analyse qualitative a montré une bonne concordance entre les images obtenues in-vivo et les altérations des bioprothèses. Les résultats des différentes méthodes étaient comparés par critères volumétriques et discutés. Les bases d'une première approche de visualisation spatio-temporelle d'images TDM 3D+T de la prothèse valvulaire ont été proposées. Elle implique des techniques de rendu volumique et de compensation de mouvement. Son application à la valve native a aussi été envisagée.

Les images scanner des bioprothèses aortiques nécessitent un traitement de débruitage et de réduction des artéfacts de façon à permettre le rehaussement des feuillets prothétiques. Les méthodes basées sticks semblent constituer une approche pertinente pour caractériser morphologiquement la dégénérescence des bioprothèses.

Mots clef : rehaussement d'image, segmentation, visualisation, bioprothèses aortiques, degeneration prothétique, valve-in-valve.

I - INTRODUCTION

Durant la dernière décennie, l'utilisation de bioprothèses valvulaires aortiques a considérablement augmenté. L'amélioration des techniques chirurgicales et la durabilité des valves ont probablement contribué cette augmentation. D'autre part, ces vingt dernières années, le risque de décès secondaire à une ré-intervention pour une chirurgie valvulaire aortique à parallèlement diminué. La mortalité opératoire des ré-interventions pour chirurgie valvulaire aortique élective est comprise entre 2 et 7%. L'amélioration de la qualité de vie des patients et ces bons résultats chirurgicaux contribuent à la large diffusion de l'implantation des bioprothèses, même chez des patients jeunes. Ce phénomène, associé à l'augmentation de l'espérance de vie dans les pays industrialisés, va probablement avoir des conséquences dans quelques années, quand de nombreux patients âgés présentant des comorbidités multiples vont nécessiter une ré-intervention pour dégénérescence de bioprothèse. Les données de la littérature montrent que le taux de mortalité peut augmenter à plus de 30% chez des patients à haut risque.

Avec l'apparition des valves percutanées pour traiter le rétrécissement valvulaire aortique chez les patients à haut risque opératoire ou récusés à la chirurgie, la communauté médicale a découvert une option séduisante, bien qu'encore débutante, pour traiter le même type de patients présentant une défaillance de bioprothèse. En effet, l'implantation de valves percutanées évite

une nouvelle sternotomie, une nouvelle circulation extra-corporelle et peut potentiellement réduire les coûts en accélérant la récupération du malade et en réduisant la durée du séjour hospitalisé. Les résultats préliminaires montrent que la procédure « valve-in-valve » est faisable, mais des études complémentaires sont nécessaires pour accepter définitivement cette technique moins invasive. Cependant, même si cela n'a pas été accepté de manière définitive par les autorités médicales ni par l'industrie, l'impression générale et les pratiques « sur le terrain » nous font considérer cette procédure comme un traitement prometteur. De multiples petites séries corroborent cette impression générale. En raison d'une meilleure qualité de vie après implantation de bioprothèse aortique, les chirurgiens cardiaques implantent aujourd'hui de plus en plus de matériel biologique, même chez les patients jeunes, au vu de la possibilité future d'implantation de prothèse par voie percutanée en cas de dégénérescence. En effet, cette future option déjà adoptée est responsable de l'extension des indications d'implantation de bioprothèses aux plus jeunes patients avec comme conséquence l'augmentation de l'incidence de la dégénérescence dans les années à venir.

La cause la plus fréquente de défaillance de bioprothèse est la dégénérescence des feuillets valvulaires. L'examen de référence de suivi des patients après remplacement valvulaire aortique reste l'échographie trans-thoracique (ETT), avec l'échographie trans-œsophagienne (ETO) en cas de doute à l'ETT. L'échographie est le gold-standard pour évaluer la fonction

des bioprothèses. Cependant, l'ETT et l'ETO restent limitées pour l'exploration morphologique des bioprothèses, spécialement en ce qui concerne les valvules des bioprothèses, à cause de leur finesse et de l'ombre acoustique causée par le stent ou par l'anneau de suture qui gêne souvent une bonne visualisation des feuillets. De plus, du fait de leur nature bidimensionnelle, il est généralement impossible de visualiser les feuillets qui ne sont pas orientés dans le plan de la sonde. Même l'échographie 3D garde, pour le moment, des applications limitées dans le cadre des bioprothèses aortiques, pour les mêmes raisons.

Ces dernières années, le scanner multi-coupes s'est avéré être un outil prometteur pour préciser des informations diagnostiques dans différentes situations cliniques, comme l'évaluation non invasive des coronaires, la fonction ventriculaire, la morphologie ventriculaire et la viabilité myocardique. Le scanner multi-coupes peut aussi aider à visualiser la morphologie et la mobilité des valves natives dans la sténose valvulaire et mesurer avec précision la surface d'ouverture des valves aortiques. Plusieurs études ont montré que le scanner multi-coupes peut aider à définir le mécanisme de dysfonction d'une prothèse valvulaire mécanique. Quelques études récentes ont montré comment le scanner 64 barrettes permet une meilleure visualisation des feuillets des bioprothèses aortiques par rapport à l'échographie et qu'il peut jouer un rôle pour définir le mécanisme de dysfonction.

Grâce à leur haute résolution spatiale, les images scanner nous permettent généralement une reconstruction 3D des structures d'intérêt. D'une manière générale, l'analyse 3D des images augmente la compréhension et facilite la planification adaptée de la procédure chirurgicale ou endovasculaire.

A l'heure actuelle, les outils disponibles pour l'analyse et le traitement des images tomodensitométriques ne permettent pas une reconstruction tridimensionnelle adaptée aux feuillets des bioprothèses en raison de leur finesse. Le péricarde bovin et les valves porcines sont en effet trop fins et les images scanner sont trop altérées par le bruit, les artéfacts des stents métalliques et les mouvements du cœur. Ceci rend difficile l'analyse 3D avec les outils dont nous disposons actuellement. De nouvelles méthodes permettant de traiter ces images haute résolution doivent donc être étudiées et proposées.

L'objectif de cette thèse est d'évaluer la faisabilité de l'analyse morphologique des bioprothèses valvulaires aortiques à partir du traitement et de l'exploration de l'imagerie scanner multi-coupes synchronisée. Après une présentation du contexte de nos travaux et de l'approche envisagée nous abordons plus précisément les questions liées au prétraitement des images, à la segmentation des structures d'intérêt, et à la visualisation spatio-temporelle.

II – CONTEXTE MEDICAL ET APPROCHE PROPOSEE

Après la présentation des différents types de bioprothèses disponibles et de leur évolution au cours des années, une analyse de la durabilité des bioprothèses en position aortique est réalisée. Plusieurs modalités en termes de dégénérescence peuvent intervenir sur les bioprothèses, mais la dégénérescence des feuillets valvulaires prothétiques reste la plus commune avec le développement de calcifications ou déchirures. L'apparition d'une micro-thrombose des feuillets dans le postopératoire immédiat, liée à un défaut de traitement anti- thrombotique, est à considérer comme un mécanisme favorisant le développement précoce d'une altération structurelle des feuillets.

L'option thérapeutique de choix pour traiter la dégénérescence structurelle d'une bioprothèse est la ré-intervention. Celle-ci est aujourd'hui une option à risque opératoire limité, mais en présence de facteurs aggravants (comorbidités multiples, urgence, etc..) elle peut devenir une intervention à très haut risque.

Le développement des procédures d'implantation endovasculaire (trans-cathéter) des valves a permis de considérer ce type d'implantation valable aussi dans les cas de dégénérescence de bioprothèse dans l'optique de traiter les patients à risque très haut ou prohibitif. La procédure valve-dans-valve représente une option thérapeutique intéressante mais plusieurs problèmes sont encore à considérer concernant la bonne sélection

des cas et la réalisation de la procédure qui reste empirique à l'heure actuelle. Une planification et optimisation de cette implantation pourrait améliorer les résultats.

Avec l'arrivée des bioprothèses trans-cathéter nous assistons à la naissance d'une nouvelle époque pour le traitement des maladies valvulaires guidé par l'image. Les différentes modalités d'imagerie deviennent de plus en plus nécessaires pour les praticiens de nouvelle génération, car la bonne compréhension structurale et morphologique de la pathologie permet une meilleure planification des procédures. Cela se traduit par une plus grande prise de conscience de la pathologie et devrait par conséquent faciliter la décision clinique et améliorer les résultats.

L'évaluation fonctionnelle des bioprothèses après remplacement valvulaire aortique s'appuie sur des paramètres échocardiographiques qui permettent, conjointement aux données cliniques, le suivi des patients. Toutefois, la fiabilité de l'échographie n'est pas la même lorsque l'on s'intéresse à la compréhension morphologique de la dégénérescence des bioprothèses qui pourrait être utile au cours du suivi standard ainsi que pour la prise de décision quant à la solution thérapeutique. Les mécanismes de défaillance tels que les calcifications ou les déchirures, la formation de pannus ou de thrombose des feuillets valvulaires devraient être détectée en pré-opératoire afin de choisir le traitement le plus adapté et de personnaliser la stratégie thérapeutique.

Dans ce contexte, l'un des points clefs de l'analyse morphologique 3D concerne la mise en œuvre de méthodes performantes pour le traitement des images préopératoires.

Dans notre étude, nous avons sélectionné des patients préalablement soumis au remplacement valvulaire aortique chirurgical par bioprothèse, hospitalisés pour dégénérescence de bioprothèse et en attente d'une ré-intervention. Ceci nous a permis de traiter et analyser les images préopératoires concernant les bioprothèses et de comparer nos résultats avec les images obtenues à partir des bioprothèses explantées après la chirurgie. Quatre patients atteints de dégénérescence de bioprothèse et éligibles pour une ré-intervention ont été considérés. Les bioprothèses dégénérées considérées se composaient de deux bioprothèses porcines Carpentier-Edwards Supra Annular Valve (23 et 25 mm), d'une bioprothèse péricardique 23 mm Edwards Perimount et d'une bioprothèse porcine 23 mm Medtronic Mosaic. Selon le cas, la ré-intervention a été effectuée à partir de 7 à 19 ans après l'implantation pour différentes raisons pathologiques.

Les protocoles d'acquisition utilisés, réalisés par un scanner multi-coupes à 64 détecteurs de 0,625 mm (General Electric VCT 64 ou Discovery 750HD), étaient les suivants :

- Protocole in-vivo : images préopératoires obtenues par un angio-scanner coronaire synchronisé à l'ECG et centré sur la bioprothèse avec une reconstruction rétrospective de plusieurs phases

du cycle cardiaque. La diastole (70% du cycle cardiaque) était considérée la plus adaptée pour analyser une bioprothèse avec ses feuillets en position de fermeture.

- Protocole ex-vivo : images postopératoires de la bioprothèse dégénérée explantée du patient. Un protocole rochers était réalisé de façon à obtenir des images haute résolution à utiliser comme référence.

Nous avons utilisé les données du scanner multi-coupes pour une évaluation morphologique tridimensionnelle des bioprothèses valvulaires aortiques, en particulier des feuillets prothétiques dégénérés.

L'approche proposée pour l'analyse morphologique des feuillets valvulaires est représentée par la figure 1. Les principales étapes intervenant dans le traitement des images sont les suivantes : (1) définition de la région d'intérêt (ROI) selon le type de stent de la bioprothèse, (2) prétraitement pour la réduction du bruit et le rehaussement des images, (3) segmentation des différentes composantes de la bioprothèse par un processus de croissance de régions (4) visualisation tridimensionnelle des résultats. Afin d'évaluer la performance de la segmentation des images « in-vivo » (images préopératoires), les méthodes de segmentation ont également été appliquées aux images « ex-vivo » (bioprothèses explantées).

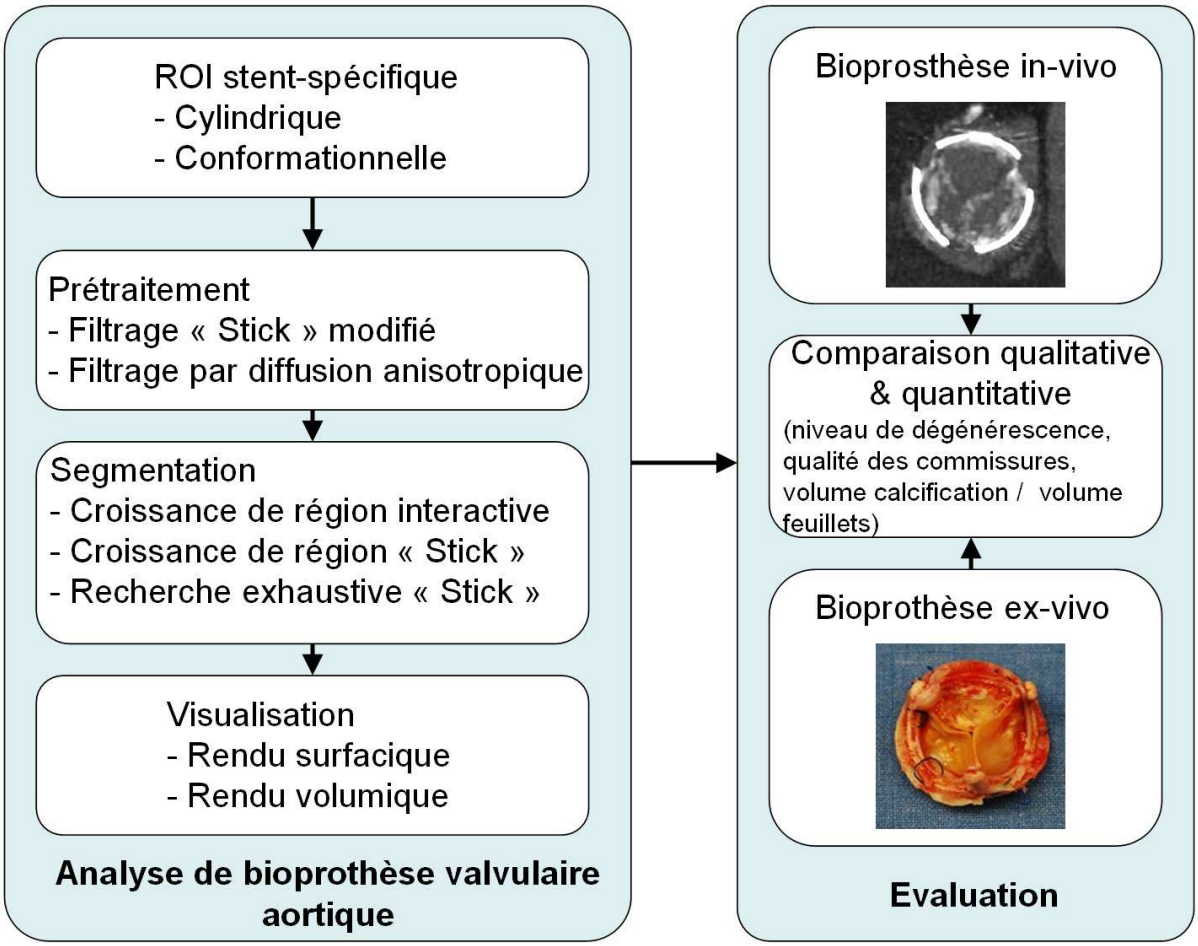

Fig. 1 : Approche proposée pour l'analyse morphologique des bioprothèses valvulaires aortiques dégénérées.

III – PRETRAITMENT

Les images scanner représentent des images nécessaires et relativement faciles à réaliser dans un contexte de bioprothèses altérées que ce soit dans l'optique d'une ré-intervention ou d'une procédure valve-in-valve. A l'heure actuelle, les outils d'analyse d'images disponibles ne permettent pas de traiter les images de façon à rehausser les feuillets prothétiques pour faciliter la segmentation de ces derniers. Différents types de méthodes de réduction d'artefacts et de bruit, applicables aux images scanner cardiaque, ont été présentées dans la littérature pour corriger ces altérations. Parmi celles-ci nous avons plus particulièrement relevé les méthodes ayant des propriétés directionnelles et fondées sur la diffusion anisotrope.

A. Région d'Intérêt

Afin de faire face aux difficultés rencontrées lors de la segmentation des images tomodensitométriques relatives à la bioprothèse (objets métalliques, finesses des feuillets, densité des composants valvulaires par rapport au stent), nous avons considéré une région d'intérêt (ROI). Bien que cette région doit inclure toutes les structures de la bioprothèse, elle doit également être aussi petite que possible. Dans cette région, qui est plus petite qu'un volume englobant cubique, la diminution du nombre de voxels doit permettre de simplifier le débruitage et la segmentation (notamment au niveau de la limite

externe des feuillets), et de diminuer le pourcentage d'artefacts métalliques et d'erreur de segmentations (principalement causées par le bruit).

La forme de cette région d'intérêt est fonction du type de la valve implantée. Nous avons considéré deux types de forme : (a) cylindrique, utilisée de préférence pour les stents métalliques incomplets et (b) conformationnelle pour les bioprothèses avec stent métallique complet (figure 2).

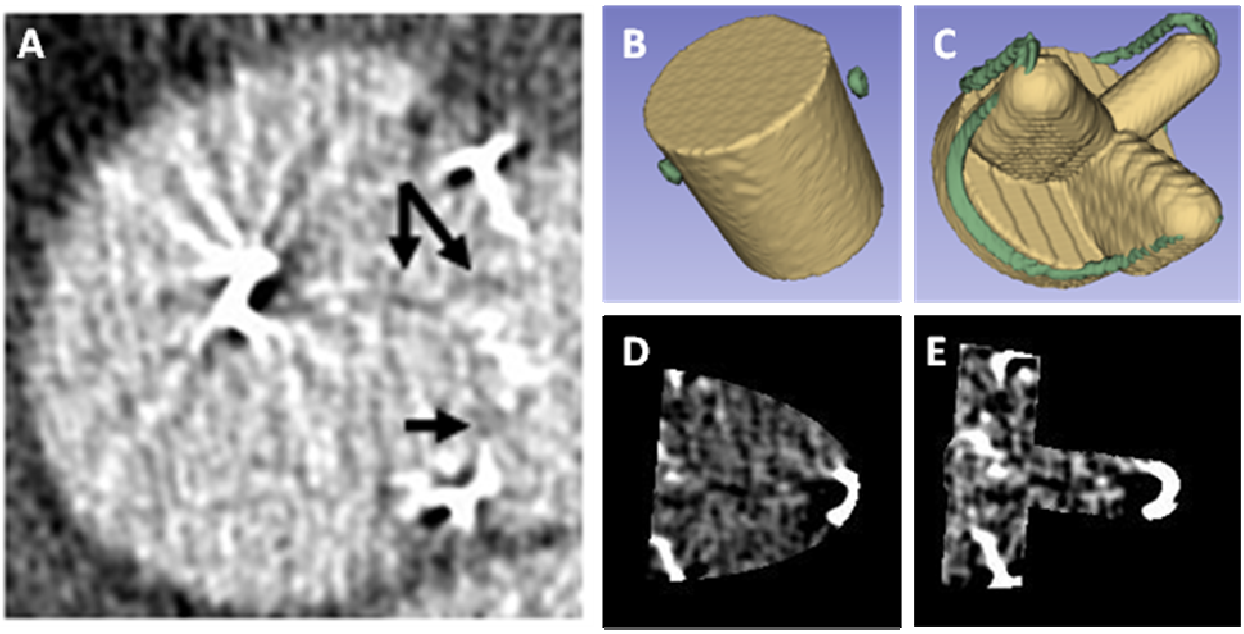

Fig. 2 : Région d'intérêt: image TDM dans un volume englobant cubique classique (A), ROI cylindrique (B) et conformationnelle (C), et illustration des images correspondantes (D et E respectivement).

B. Rehaussement et classification

Afin de réduire les hyperdensités parasites dans les images tomographiques, un prétraitement est nécessaire. Le but de cette étape est d'augmenter le

rapport signal/bruit (SNR) et d’améliorer le contraste des structures d'intérêt, notamment les feuillets valvulaires.

Nous avons opté pour des méthodes basées sur une adaptation des filtres de diffusion (technique de filtrage anisotrope) et sur une version modifiée et améliorée du filtre "stick", initialement décrit pour le filtrage d’images doppler afin de réduire les échos parasites et d’affiner l’analyse des structures minces. Pour sélectionner l’approche la plus appropriée avant l'étape de segmentation, nous avons considéré le SNR comme critère de performance.

Les *filtres de diffusion anisotrope* ont été présentés dans la littérature pour débruiter les images, notamment les images scanner cardiaques. Grâce à leur aptitude à analyser l'image dans différentes directions, ils permettent d'envisager le rehaussement et le débruitage d’images scanner, tout en conservant les détails des structures fines tels que les feuillets prothétiques. Un niveau de bruit trop élevé dans les images constitue toutefois une limitation pour les filtres de diffusion anisotrope, notamment avec formulation initiale proposée par Perona et Malik. Pour améliorer leur performance dans ces conditions, nous avons utilisé au niveau de la fonction de diffusion la fonction d'arrêt de Tukey et l'écart absolu médian (MAD) conjointement au gradient lissé (Catté_PM) ou à l'information de courbure (ACD). Un filtrage médian a de plus été utilisé pour compléter le processus de filtrage et réduire le bruit impulsionnel.

Le *filtre stick* repose quant à lui sur le partitionnement du voxel considéré en un ensemble de bâtonnets asymétriques pour effectuer un filtrage non-linéaire de l'image. En raison de son asymétrie, le filtre pourrait obtenir de meilleures performances en ce qui concerne la qualité des détails des structures fines (comme les feuillets valvulaires). Ce filtre a été adapté pour le prétraitement des images scanner de la dégénérescence des bioprothèses aortiques. Dans l'approche proposée, le filtre stick modifié implique une étape préalable de classification, fondée sur l'analyse de configurations particulières dans la région d'intérêt, suivie d'une étape de filtrage adapté à la classe des voxels (lumière vasculaire, feuillets, artefacts, ...).

Contrairement au filtre de diffusion, le nombre d'itérations ne constitue pas un paramètre sensible. Le filtre stick montre un comportement convergent après plusieurs itérations. Typiquement, le résultat converge après 5 itérations pour un SNR inférieur ou égal à 8 et après 3 itérations lorsque le SNR est supérieur à 10. L'inconvénient du filtre stick est sa complexité calculatoire (nombre d'opérations à réaliser). Le temps de calcul peut être raccourci par une ROI définie par le stent. Le nombre de voxels se réduit généralement à 40% du volume englobant cubique avec la ROI cylindrique et à 16% de ce volume avec la ROI conformationnelle.

C. Résultats

Pendant la ré-intervention le mécanisme de dégénérescence de chaque bioprothèse explanté était évalué. La figure 3 montre les 4 cas de dégénérescence. Les images du scanner synchronisé préopératoire (in-vivo) ont été d'abord analysées par le logiciel de la console scanner AW Volume Share (General Electric Healthcare workstation) avec des résultats qui n'étaient pas satisfaisants en ce qui concerne le rehaussement des feuillets prothétiques à cause de l'importante quantité de bruit et d'artefacts. Enfin, les images ont été traitées par les méthodes de filtrage.

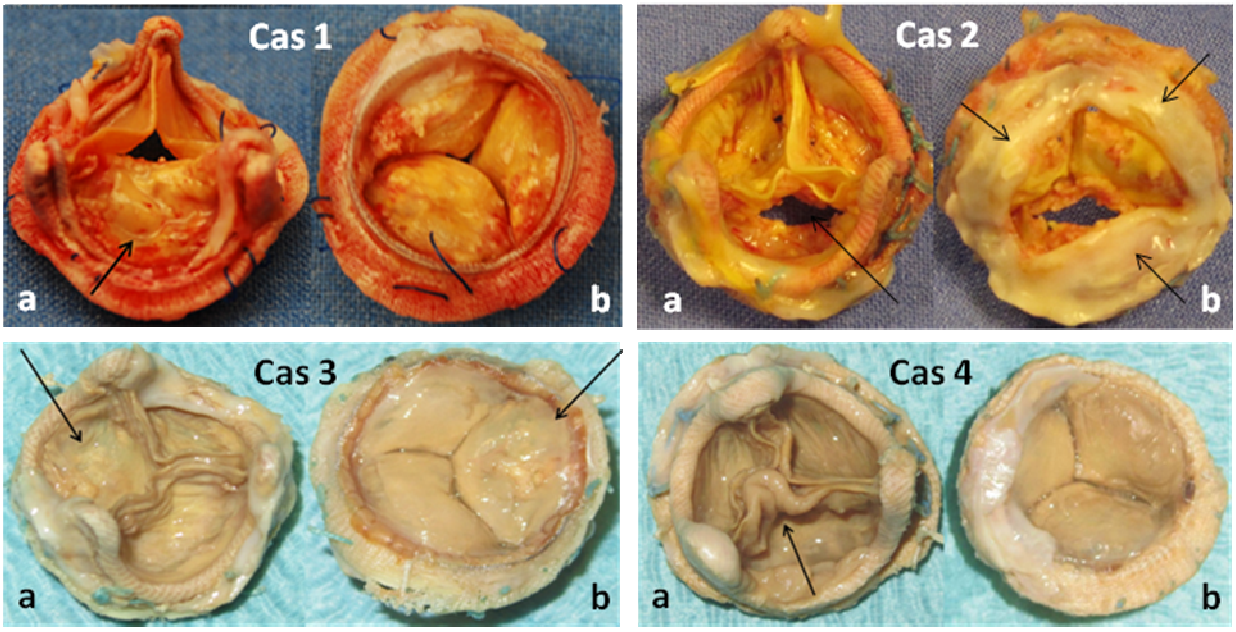

Fig 3 : Cas n°1 – bioprothèse péricardique montrant un prolapsus d'un feuillet calcifié. Cas n°2 – bioprothèse porcine présentant une déchirure d'un feuillet et la présence d'un pannus sous-valvulaire calcifié. Cas n°3 – bioprothèse porcine ayant un feuillet calcifié. Cas n°4 – bioprothèse porcine avec feuillet colonisé par une infection.

Les voxels spécifiques aux bioprothèses ont d'abord été sélectionnés en considérant la ROI définie par le stent. Une première appréciation qualitative

des résultats montre que le filtre Stick modifié rehausse mieux le contraste entre les feuillets valvulaires et les structures environnantes. En plus de cette évaluation qualitative, le SNR a été calculé à partir des images d'origine et des images traitées (figure 4). Cette évaluation objective montre que le filtre stick permet d'obtenir le meilleur SNR pour les quatre patients. Ce résultat est compatible avec l'appréciation subjective.

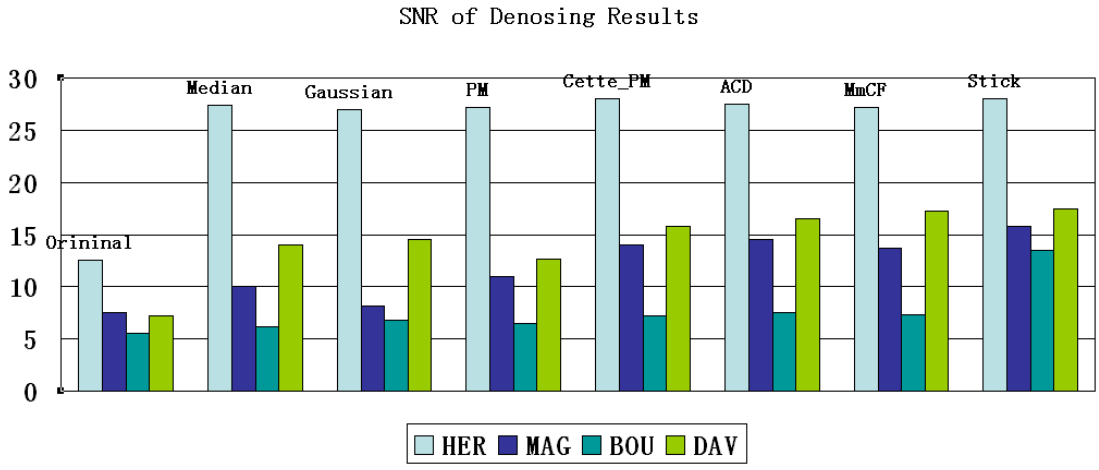

Fig. 4: Rapport signal/bruit (SNR) des images originales et obtenues après débruitage par différents filtres.

Le prétraitement des données représente une étape essentielle. En effet, les images tomodensitométriques des bioprothèses doivent être débruitées avant d'être segmentées en raison de la présence de bruit et d'artefacts. Différents filtres ont été testés en vue d'améliorer le contraste des feuillets valvulaires. Le filtre stick, modifié afin d'être appliqué aux images tomodensitométriques, a montré de meilleurs résultats visuels. Cette constatation a été confirmée par

les analyses objectives du SNR. Il est à noter que ce processus de filtrage est réalisé par le logiciel MatLab et nécessite un temps de calcul plus importants.

IV SEGMENTATION

La segmentation consiste à réaliser un partitionnement de l'image en ensembles de pixels/voxels, ou segments. De nombreuses méthodes ont été reportées dans la littérature. Les méthodes utilisées dans le cadre des images de scanner cardiaque font notamment appel à des techniques de type classification ou seuillage, de type région ou de type contour, ou à la combinaison de ces approches.

A. Méthodes proposées

Quatre types principaux de tissus sont identifiables selon la valeur de densité (Hounsfield Units - HU) mesurée au scanner. Par ordre décroissant de HU on reconnaît: le stent, les calcifications des feuillets, la lumière vasculaire et les feuillets valvulaires. Le premier élément, affichant des valeurs HU élevées, peut être aisément segmenté par seuillage. La segmentation envisagée est plus particulièrement centrée sur les feuillets bioprothétiques.

Trois méthodes de segmentation de régions ont été implémentées (avec différents niveau d'interactivité pour l'utilisateur) pour la segmentation des feuillets prothétiques.

1 - *Croissance de région "interactive" (IRG)*

Ce processus interactif vise à fournir une approche de référence pour l'évaluation des résultats. Un critère (seuil) d'agrégation des voxels très sélectif a volontairement été choisi afin d'obtenir des régions très homogènes. La contrepartie est la taille très restreinte de ces régions à l'issue de la croissance, et donc la nécessité de définir interactivement un nombre important de points germes pour obtenir une segmentation complète des structures d'intérêt. Cette segmentation est réalisée au moyen du logiciel 3D Slicer après une phase de prétraitement des images basé sur le filtrage par diffusion anisotrope.

Pour chaque composante prothétique, de multiples points germes (environ 20) ont été sélectionnés de façon interactive. L'algorithme par croissance de région a été appliqué (voisinage 26 connexes). Le critère d'agrégation des voxels s'appuie sur la moyenne et l'écart type de la valeur des voxels dans le voisinage cubique considéré. Les valeurs initiales des seuils d'agrégation fournies automatiquement par le logiciel est réajustées interactivement par l'utilisateur. L'extraction et la visualisation des résultats du maillage de surface 3D délimitant les régions ont été réalisées en utilisant l'algorithme du Marching Cube.

2 - *Croissance de région Stick (Stick RG)*

Afin d'améliorer la segmentation des structures fines, notamment des feuillets valvulaires prothétiques, nous avons développé une méthode par croissance

de région directionnelle basé sur un voisinage structuré en bâtonnets (voisinage stick) dans la région d'intérêt (ROI).

Un nombre très limité de points germes (en général 4 à 6) sont sélectionnés de manière interactive à l'intérieur des feuillets. Un ensemble de N voxels à l'intérieur des feuillets a été défini en tenant compte, pour chaque point germe, des voxels appartenant à leur voisinage défini par les sticks. Le critère de similitude prend en compte la cohérence des directions de sticks ayant des distributions de niveau de gris comparables (variations des valeurs le long du stick). Cette approche a été mise en oeuvre en utilisant les outils de développement logiciel MatLab. Lorsque le voxel appartient à la composante qui nous intéresse, il constitue un nouveau point d'origine. Ce processus est répété jusqu'à ce qu'aucun nouveau voxel ne soit marqué comme appartenant à la même classe que le point germe.

3 – *Recherche Exhaustive Stick (SES)*

Afin de réduire davantage le niveau d'interactivité dans le processus de segmentation, une exploration systématique de la ROI a été mise en place sans avoir besoin de définir les points germes.

En considérant les voxels situés dans la ROI, nous utilisons le résultat de la classification réalisée dans la phase de prétraitement. Le voisinage (typiquement 7 * 7 * 7 voxels) de tous les voxels à l'intérieur de la ROI est partitionné en un ensemble de sticks asymétriques et analysé afin de classer

les voxels comme appartenant à des structures fines (incluant les feuillets), à la lumière vasculaire, à des structures tubulaires (incluant le stent métallique complet) ou aux autres structures (incluant les calcifications et le stent métallique incomplet). En considérant les Sticks S_m présentant de faibles variations locales de valeurs, cette classification est ensuite affinée par seuillage afin d'identifier les voxels appartenant aux composantes de la bioprothèse : feuillets (valeurs moyennes locales faibles le long de S_m), stent métallique complet (valeurs moyennes locales élevées le long de S_m), calcifications et stent métallique incomplet (valeurs moyennes locales le long de S_m supérieures aux valeurs de la lumière artérielle). Pour cette opération trois seuils sont utilisés. Ils sont déterminés interactivement par simple pointage d'un voxel appartenant au stent, aux calcifications, et à la lumière artérielle. Cette méthode de segmentation simplifie le mode opératoire, mais peut s'avérer moins performante en présence de bruit et d'artefacts en raison de la définition globale des trois seuils.

B. Résultats

Après l'étape de prétraitement, les différentes méthodes de segmentation (IRG, Stick RG et SES) ont été appliquées aux images in-vivo (IV) et ex-vivo (EV). Nous présentons les résultats obtenus pour chaque patient (HER, MAG, BOU et DAV) en considérant le meilleur volume scanner (phase optimale) du

cycle cardiaque en fin de diastole, lorsque les valvules prothétiques sont fermées.

Le premier exemple est représenté par le cas de la bioprothèse péricardique (HER). Grâce à la haute qualité de ces images toutes les méthodes de segmentation donnent des résultats qualitativement similaires et satisfaisants (figure 5).

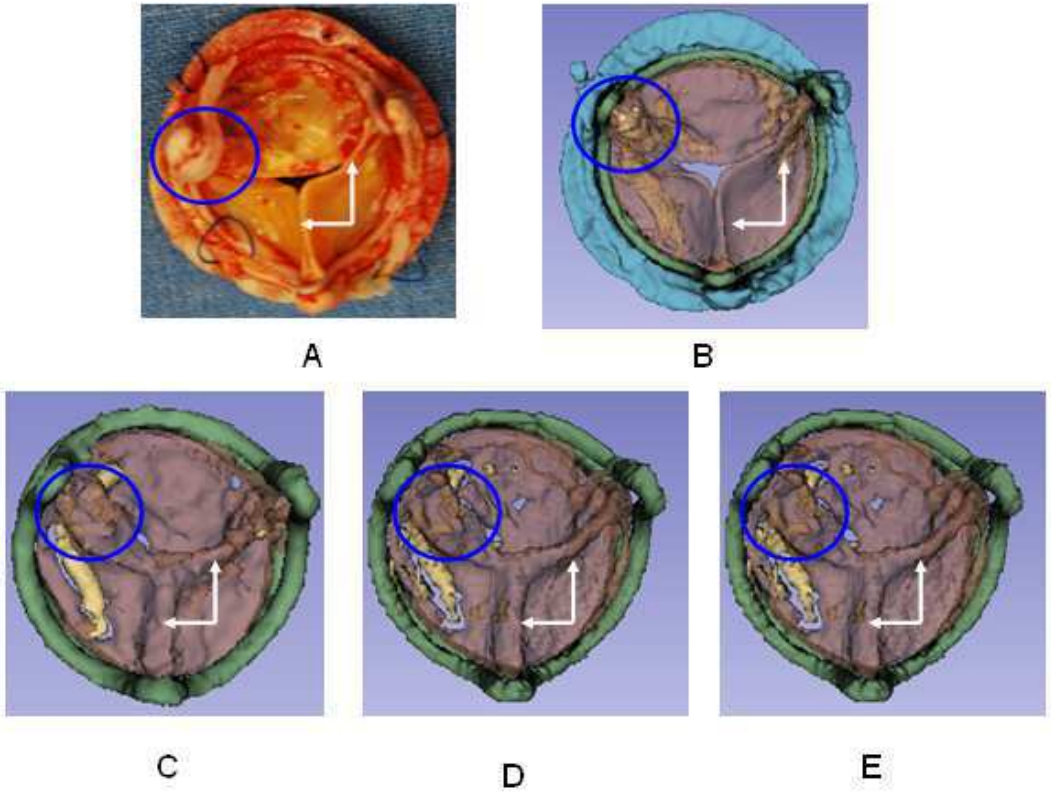

Fig. 5: Visualisation des résultats dans le cas n° 1 - HER. Bioprothèse explantée (A), segmentation des images ex-vivo (B), segmentation des images in-vivo par méthode IRG (C), Stick RG (D) et SES (E). La perte d'une commissure est indiquée avec les cercles bleus et la bonne coaptation des feuillets avec les flèches blanches.

Le deuxième exemple illustre les résultats obtenus dans les deux cas de bioprothèse porcine (BOU et DAV). Bien que les images initiales étaient faiblement contrastées et très bruitées dans la zone d'intérêt, les bords des

feuillets semblent bien détectés. Néanmoins, par rapport à la segmentation interactive (IRG), les méthodes basées sur les sticks (Stick RG et SES) ne permettent pas une description complète des feuillets (figure 6).

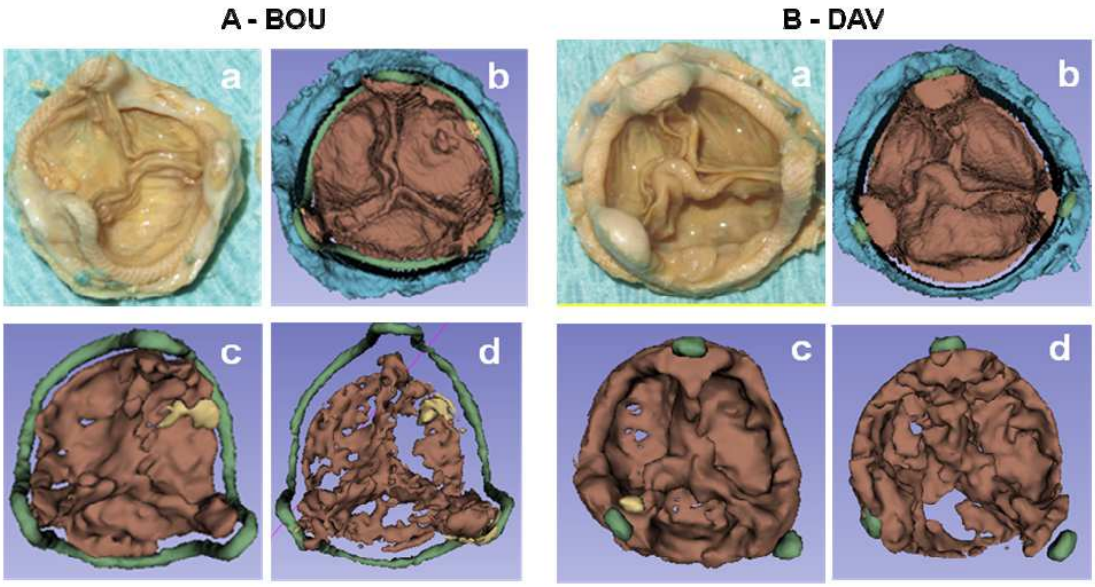

Fig. 6: Visualisation des résultats dans les cas n°3 – BOU (A) et 4 – DAV (B). Bioprothèse explantée (a), segmentation des images ex-vivo (b), segmentation des images in-vivo par méthode IRG (c) et Stick RG (d).

Au vu de ces résultats (BOU et DAV), nous observons que les feuillets n'étaient pas entièrement segmentés : ils apparaissent avec des trous ou des pièces manquantes. La raison pourrait être liée à la présence de calcifications et à un effet de volume partiel. Pour remédier à ce défaut de segmentation, dans certains cas, on pourrait procéder de la manière suivante :

- segmentation automatique basée sur Stick RG (ou SES) pour décrire les principales composantes de la bioprothèse ;
- segmentation interactive (IRG) pour compléter la description des parties manquantes des feuillets.

Dans le cas 2 – MAG d'une bioprothèse porcine, en raison de la présence de structures à très faible contraste, la segmentation des feuillets était particulièrement complexe. L'IRG donnait les meilleurs résultats, mais pas entièrement satisfaisants dans ce cas. Une amélioration manuelle à dû être mise en place.

La principale difficulté était dans ce cas le haut niveau de bruit et des frontières entre les structures très peu contrastées (absentes localement). Tous les voxels de valeurs faibles situés dans la ROI ont été classés comme feuillets. En outre, il existe de nombreuses régions incomplètes dans les feuillets.

La visualisation des résultats de segmentation a été réalisée par rendu volumique (figure 7). La présence d'un pannus sous-valvulaire calcifié est caractéristique dans ce cas et responsable de l'obstruction de la valve.

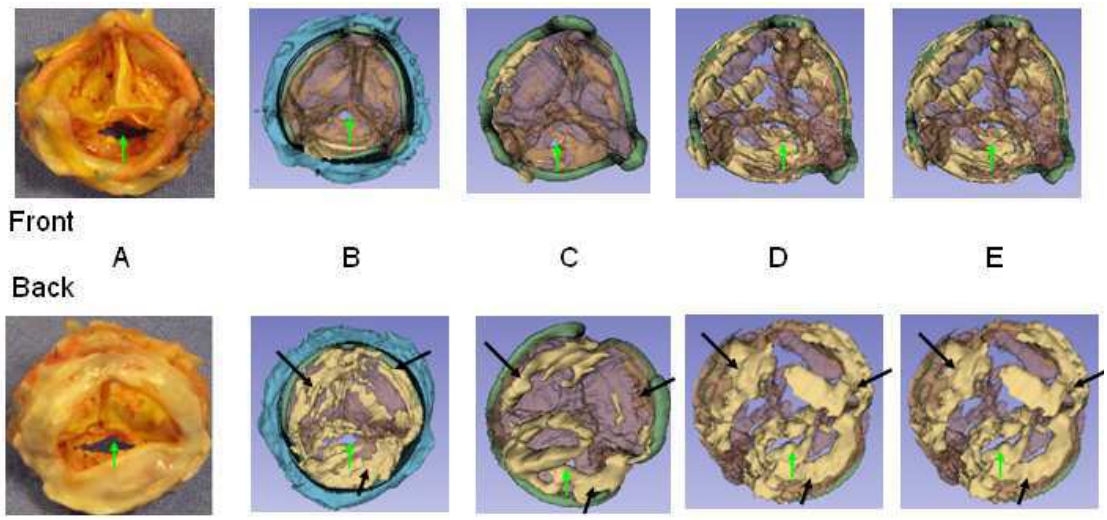

Fig. 7: Visualisation des résultats de segmentation du cas n° 2 - MAG. Bioprothèse explantée (A), images ex-vivo segmentées (B), images in-vivo segmentées par la méthode IRG (C), Stick RG (D) et SES (E). Le pannus calcifié est indiqué par les flèches noires et la déchirure des feuillets par les flèches vertes.

Une analyse volumétrique a ensuite été menée afin de comparer objectivement les résultats obtenus par les trois méthodes sur les images in-vivo (IV) et ex-vivo (EV). Le critère utilisé pour évaluer les résultats était le volume des composants de la bioprothèse. Les résultats de cette analyse sont présentés en figure 8 (les volumes sont exprimés en mm^3).

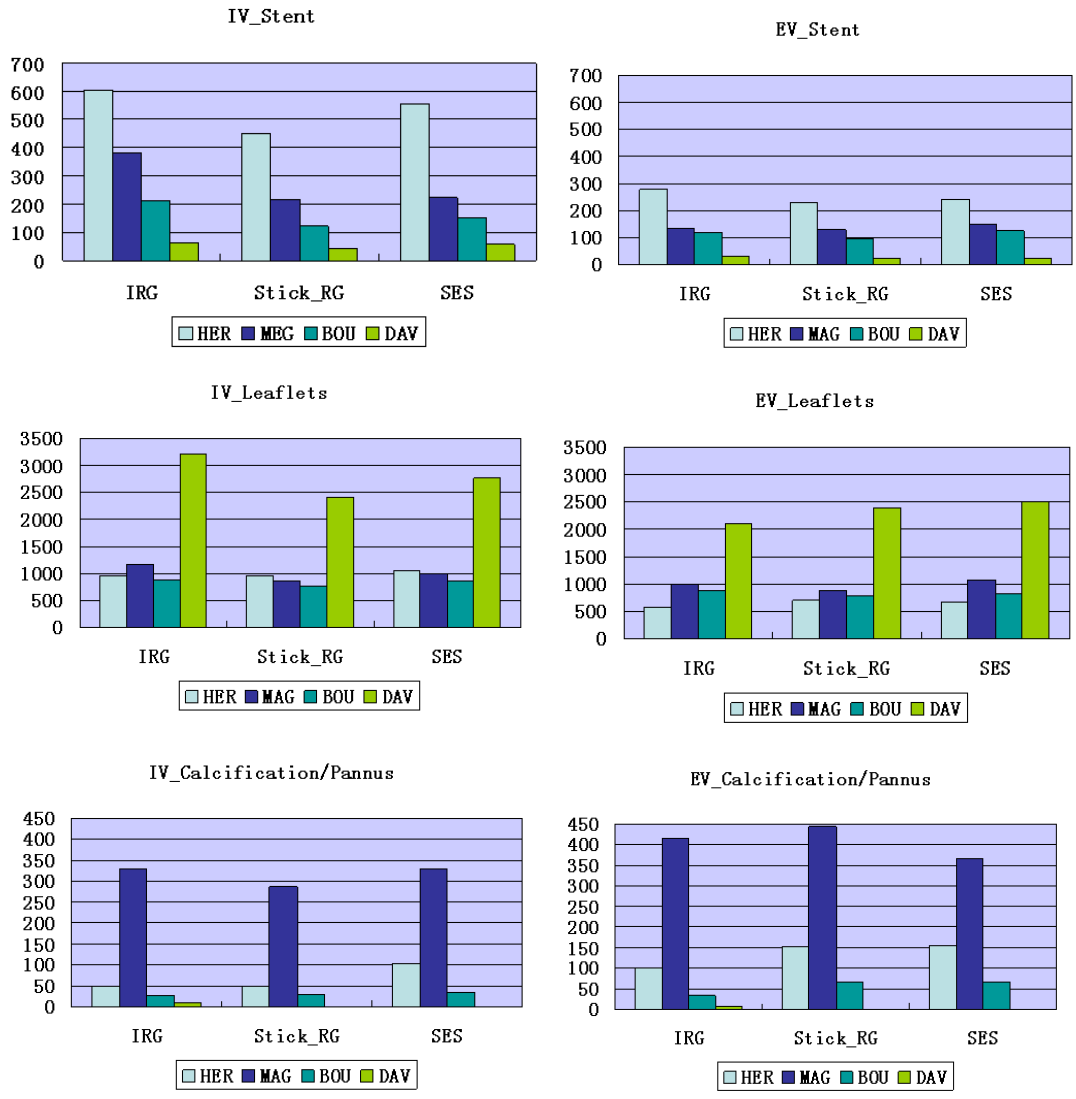

Fig. 8: Analyse volumétrique des composantes des bioprothèses.

Une correction de la différence de volume entre les données in- et ex-vivo pour les feuillets prothétiques était envisagée en considérant le stent comme structure de référence. L'estimation du taux de correction permettant de compenser des distorsions pouvant être liés à différents facteurs (mouvement des structures, conditions anatomo-physiologiques in-vivo vs. ex-vivo), pourrait être assimilée à un étalonnage. L'application de ce taux de correction dans le cas HER semble réduire les différences entre les volumes des feuillets in-vivo et ex vivo (figure 9).

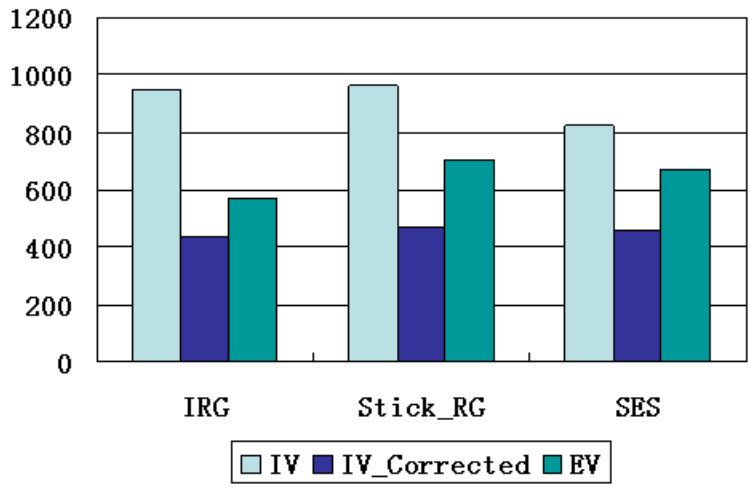

Fig. 9: Application du taux de correction dans le cas n°1.

C. Discussion

Dans cette étude, nous avons testé trois méthodes de segmentation par région d'images tomodensitométriques sur des bioprothèses aortiques dégénérées. Ces méthodes, d'approche différente, semblent donner des résultats comparables. Il s'agit de méthodes de segmentation

semi-automatique. La méthode IRG nécessite plus d’interaction en comparaison avec les méthodes stick RG et SES.

Parmi les images analysées, les meilleurs résultats ont été obtenus dans le cas de la bioprothèse péricardique. La raison en est attribuée en partie à l'épaisseur du tissu valvulaire. En effet, les feuillets valvulaires péricardiques sont plus épais que les feuillets valvulaires d’origine porcine. Des volumes plus élevés ont été observés dans certains composants des bioprothèses in-vivo, en comparaison aux bioprothèses ex-vivo. Plusieurs facteurs expliquent cette différence. En effet, outre le fait qu’il n’existe pas d’acquisition spécifique pour analyser les bioprothèses, la résolution d'image n'est pas la même in-vivo et ex-vivo. Les acquisitions ex-vivo ont été réalisées par un protocole haute résolution afin d’optimiser la qualité des images, alors que les acquisitions in-vivo ont été réalisées par le protocole standard des scanners coronaires couplés à l’ECG. Lors de cet examen, les mouvements cardiaques et la superposition du sang engendrent des différences volumiques non négligeables. Pour faire face à ce problème, nous proposons un facteur de correction qui pourrait représenter un moyen intéressant pour réduire les différences de volume, mais il faudrait le valider à plus grande échelle.

Notre étude suggère que l'analyse 3D préopératoire des bioprothèses dégénérées est faisable, mais les images TDM ont besoin d’un traitement supplémentaire. Une fois améliorées, les images peuvent être segmentées et les reconstructions qui en résultent peuvent aider à visualiser directement la

morphologie des feuillets et pourraient jouer un rôle dans la compréhension du mécanisme de dégénérescence des bioprothèses. De plus, ces méthodes arrivent à identifier la présence de calcifications des feuillets ainsi que la présence d'un pannus sous valvulaire.

V. VISUALISATION

La dégénérescence structurelle d'une bioprothèse s'accompagne de défauts fonctionnels au cours du temps. La compréhension précise du disfonctionnement de la bioprothèse pourrait fournir à terme des éléments d'aide à la décision pour la prise en charge clinique de la pathologie. Dans cet objectif la visualisation vient compléter l'ensemble de la chaine de traitement. Elle est considérée ici comme un élément pouvant permettre de pallier aux difficultés de segmentation de l'imagerie scanner préopératoire d'une part, et de restituer plus complètement l'information spatio-temporelle fournie par certains examens d'imagerie scanner multi-détecteurs d'autre part.

Dans l'étude précédente nous avons présenté des visualisations des résultats de la segmentation réalisée pour une seule phase du cycle cardiaque, la diastole. L'objectif est ici de reconsidérer la question de la visualisation de jeux de données dans le cas d'un examen d'imagerie scanner multiphasique. L'hypothèse sous-jacente est, qu'en présence de données spatio-temporelles, un processus de visualisation correctement élaboré pourrait permettre d'interpréter le mouvement des feuillets valvulaire et de suppléer en partie le processus de segmentation.

A. Visualisation spatio-temporelle

Les techniques de visualisation par ordinateur se sont largement développées ces dernières années. Le rendu visuel est généralement défini comme un processus permettant de générer une image à partir d'un modèle ou d'une description de scène. Ceux-ci peuvent être issus d'un examen d'imagerie tridimensionnelle. Pour les applications médicales on distingue plusieurs approches dont les plus utilisées sont la projection d'intensité maximale, le rendu surfacique et le rendu volumique. Le rendu volumique ne requiert pas une segmentation ou binarisation préalable du volume image décrivant les structures d'intérêt. Nous nous sommes plus particulièrement intéressés au rendu volumique direct qui implique un schéma de lancer de rayon simplifié et la possibilité de d'intégrer des fonctions de transfert sur les niveaux de gris permettant d'affecter des niveaux de transparence / opacité variables en fonction de la nature des tissus et de la répartition spatiale des structures.

La visualisation des structures valvulaires reste un problème ouvert. Elle pose notamment des difficultés liées: (i) à la correction des artefacts d'acquisition multiphasique et à la compensation des variations d'intensité inter-phases dues à la diffusion du produit de contraste dans les structures vasculaires, (ii) à l'élaboration des fonctions de transfert impliquées dans le processus de rendu, et (iii) au contrôle de la pose de la caméra virtuelle, impliquant la

compensation de certains mouvements de structures, en l'occurrence celui de la racine aortique , afin d'isoler le mouvement des feuillets valvulaires.

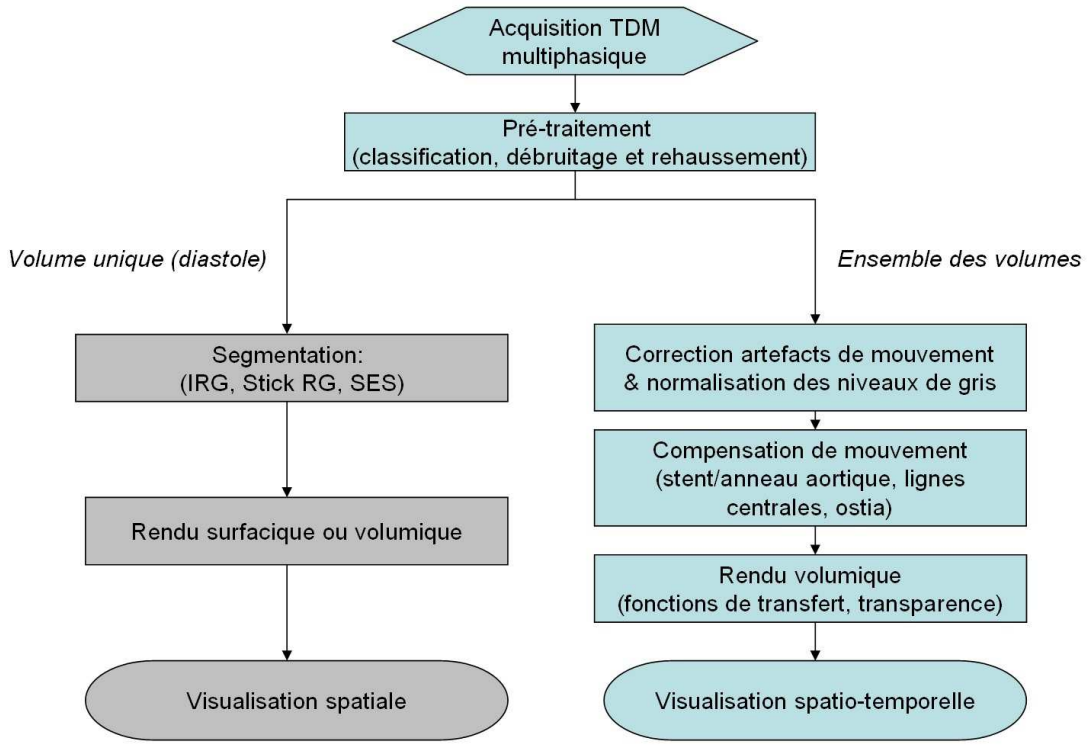

Fig. 10 : Processus de visualisation spatio-temporelle (en bleu).

Le processus de visualisation élaboré est représenté figure 10. A l'issue de l'acquisition multiphasique certains volumes sont affectés d'artefacts de reconstruction qui se traduisent par un décalage latéral d'un ensemble de coupes. On peut espérer qu'avec les progrès sur les dispositifs d'imagerie ces phénomènes disparaitront à terme. Ces artefacts de mouvement ont été corrigés en estimant le déplacement correctif à partir du coefficient de corrélation normalisé entre les coupes voisines et décalées qui ont été repérées interactivement. Par ailleurs les niveaux de gris dans les images

tridimensionnelles ont été normalisés en considérant les distributions de niveaux de gris dans la zone des feuillets valvulaires afin de compenser variations d'intensités inter-phases.

Une part importante des travaux a été consacrée à l'élaboration des fonctions de transfert pour le rendu visuel. Celles-ci prennent en compte la répartition spatiale des structures d'intérêt à partir de la classification réalisée dans la phase de pré-traitement des images et la nature de ces structures pour leur affecter des niveaux de transparence/opacité variables. Il en résulte que la visualisation n'impose pas une segmentation complète des structures. Pour les configurations ambigües (lumière vasculaire proche des feuillets vasculaires, structures de forte densité incluant les calcifications) les voxels ne sont pas rendus complètement transparents, afin de ne pas perdre d'information. L'interprétation est laissée à l'utilisateur lors de la visualisation renforcée par la dimension temporelle.

Dans les données considérées les mouvements des structures d'intérêts, *i.e.* des feuillets valvulaires, sont observés dans une structure elle même en mouvement, racine aortique et aorte ascendante. Afin d'interpréter correctement le mouvement des feuillets il est nécessaire de contrôler la pose de la caméra virtuelle utilisée pour la visualisation et de l'asservir ou la solidariser à la structure aortique afin de compenser son mouvement dans le rendu visuel. Cette compensation de mouvement est réalisée en déterminant la pose de la caméra par rapport à des caractéristiques structurelles liées

cinématiquement à la racine aortiques : stent de la bioprothèse, anneau valvulaire, ostia coronaires.

B. Résultats

Le processus de visualisation proposé a été testé sur une acquisition muliphasique de 10 volumes dans un cas de bioprothèse dégénérée. Même si ce n'était pas l'objet de ce travail, il a aussi été testé sur une acquisition multiphasique de 8 volumes dans un cas de valve native dégénérée qui présente intrinsèquement des épaisseurs de feuillet plus épais que la bioprothèse. Les résultats sont présentés respectivement par les figures 11 et 12. Ces figures permettent de comparer qualitativement les résultats obtenus par le processus décrit précédemment avec les résultats obtenus sans normalisation inter-phase des niveaux de gris et avec une compensation de mouvement basée sur la définition interactive d'un volume image englobant la structure d'intérêt pour chacune des phases.

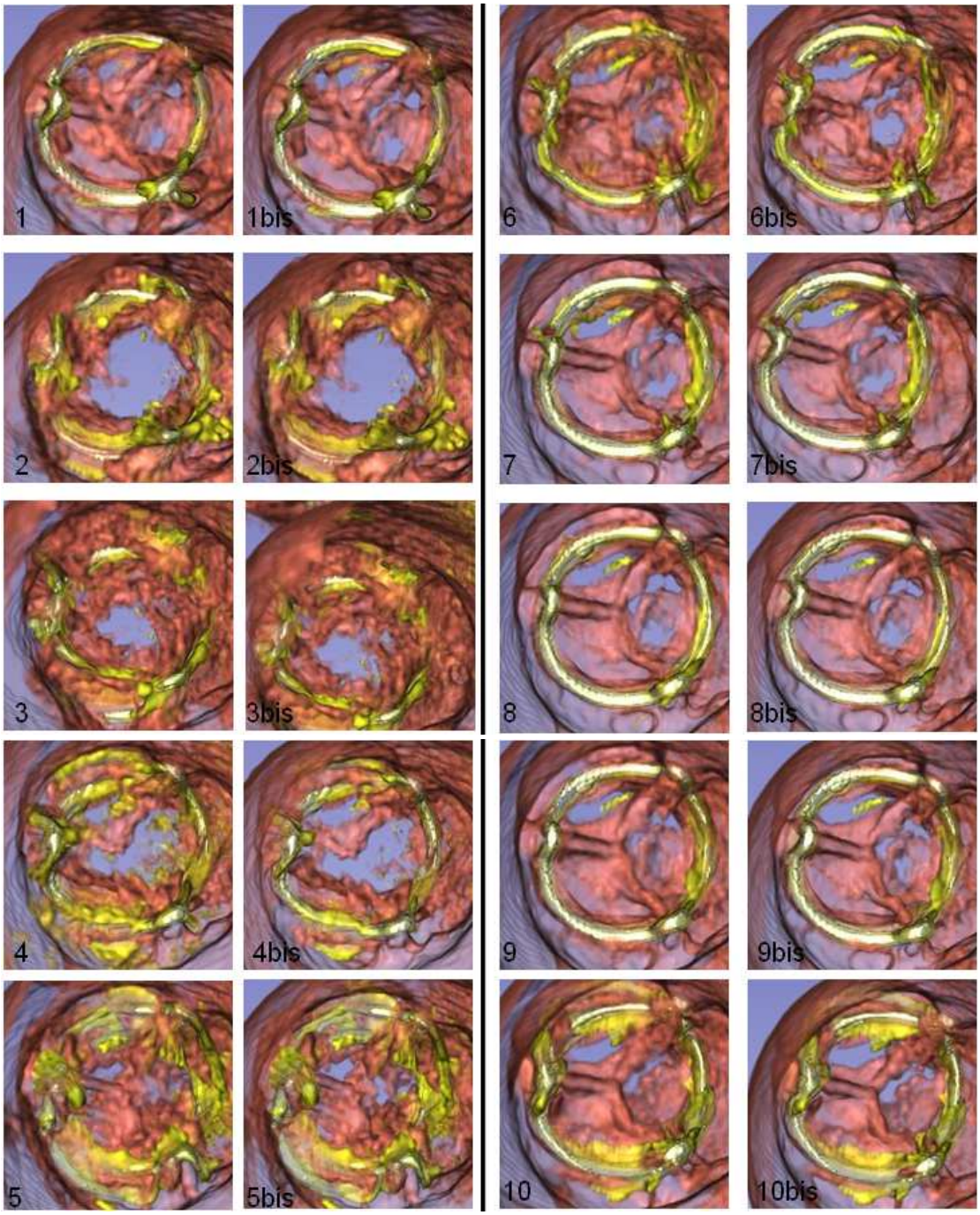

Fig. 11 : Visualisation saptio-temporelle de la bioprothèse pour le cas HER avec la méthode proposée et, à titre comparatif, visualisation avec compensation de mouvement grossière et sans normalisation inter-phase des niveaux de gris.

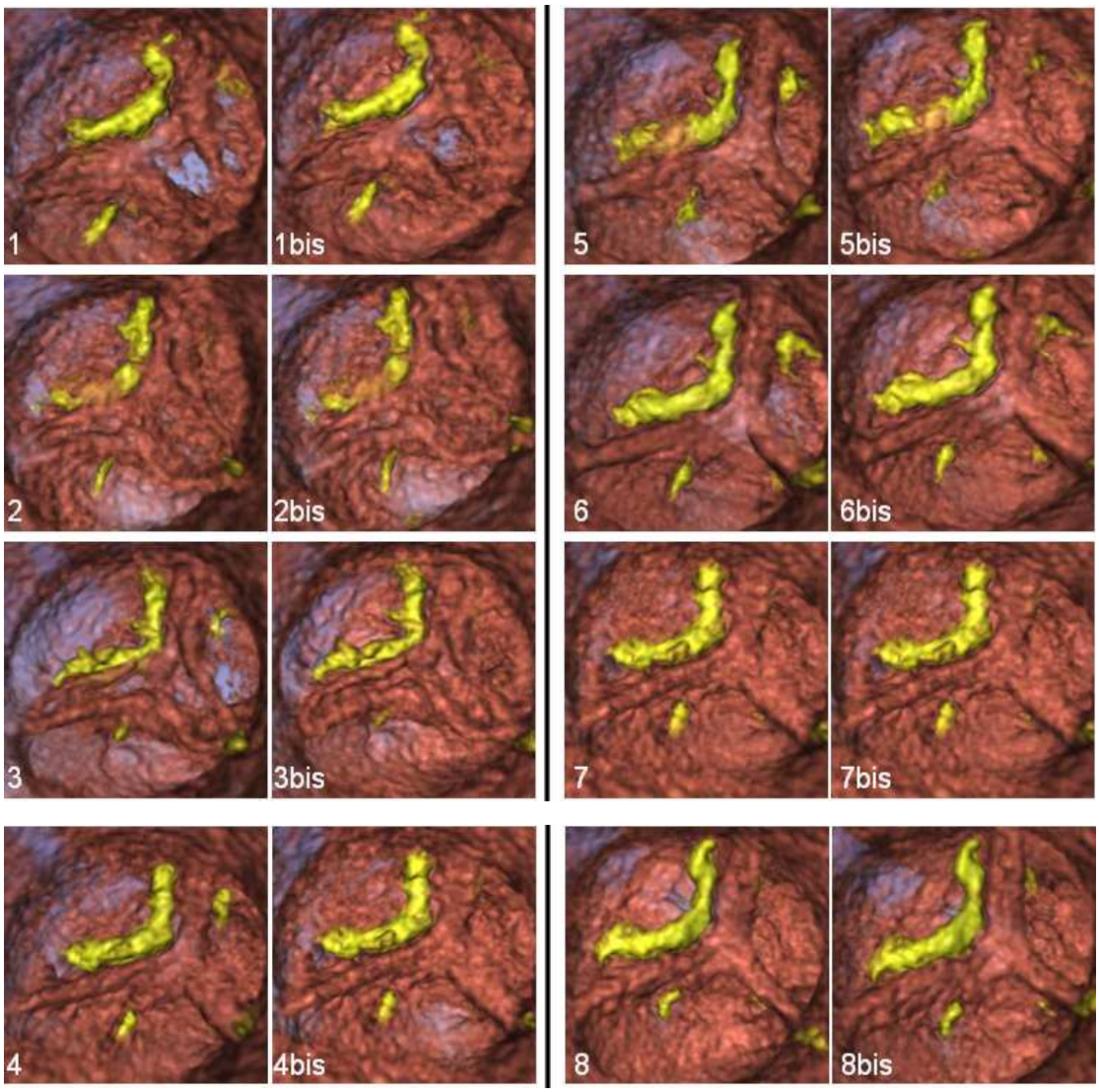

Fig. 12 : Visualisation saptio-temporelle dans le cas d'une valve native avec la méthode proposée et, à titre comparatif, visualisation avec compensation de mouvement grossière et sans normalisation inter-phase des niveaux de gris.

Dans les deux cas (bioprothèse, valve native), la séquence spatio-temporelle complète a pu être visualisée à partir des données fournies par la phase de pré-traitement uniquement. Dans le cas de la bioprothèse, même si certaines zones des feuillets apparaissent transparentes on distingue les mouvements de fermeture et d'ouverture des feuillets ainsi que les zones calcifiées et non

calcifiées. Ces mouvements pourraient à terme être analysés plus finement et quantifiés pour caractériser l'altération fonctionnelle de la bioprothèse. Dans le cas de la valve native, même si la compensation de mouvement est moins contrôlée (en raison de l'absence de stent), le rendu semble de meilleure qualité (en raison de l'épaisseur des feuillets valvulaires) et on peut clairement observer la paroi artérielle, le mouvement des feuillets altéré par la présence de calcifications importantes.

VI. CONCLUSION ET PERSPECTIVES

Même si s'échocardiographie reste la référence pour l'analyse fonctionnelle des bioprothèses dégénérées, ces dernières années ont vu naître un intérêt particulier concernant l'analyse morphologique de la valve aortique par images scanner.

Dans cette thèse nous avons proposé une nouvelle approche pour l'analyse morphologique des bioprothèses valvulaires aortiques dégénérées par segmentation et visualisation d'images tomodensitométriques.

Le rehaussement des images et la réduction du bruit est fondée sur une approche de filtrage stick modifiée. Elle a montrée de meilleurs résultats en rapport signal/bruit en comparaison aux filtres de diffusion anisotrope. Les méthodes de segmentation ont permis une reconstruction 3D des feuillets. L'analyse qualitative a montré une bonne concordance entre les images obtenues in-vivo et les altérations des bioprothèses. Les résultats des différentes méthodes ont été comparés par critères volumétriques et discutés. Les bases d'une première approche de visualisation spatio-temporelle de l'imagerie TDM dynamique de la prothèse valvulaire ont été proposées. Elle implique des techniques de rendu volumique et de compensation de mouvement. Son application à la valve native a aussi été envisagée.

Nos résultats préliminaires suggèrent la possibilité d'améliorer le rehaussement des feuillets bioprothétiques aortiques en appliquant les méthodes de traitement envisagées pour réduire le bruit, segmenter et visualiser les images scanner préopératoires. Parce qu'à ce jour l'analyse morphologique des feuillets des bioprothèses est complexe voire impossible avec d'autres techniques d'imagerie, nous croyons que dans un avenir proche l'exploration et l'interprétation d'images scanner à haute résolution pourrait jouer un rôle important chez les patients ayant une bioprothèse aortique dégénérée pour améliorer la compréhension du mécanisme de dysfonctionnement.

Des études supplémentaires sont nécessaires pour améliorer et valider ces résultats. Sous réserve d'une validation plus poussée des méthodes de traitement d'image proposées, vraisemblablement accompagnée d'une adaptation des protocoles d'acquisition, une analyse de la dégénérescence des bioprothèses pourrait être envisagée sur des séries plus importantes.

Processing and exploration of CT images for the assessment of aortic valve bioprostheses.

Abstract

The aim of the study was to assess the feasibility of CT based 3D analysis of degenerated aortic bioprostheses to make easier their morphological assessment. This could be helpful during regular follow-up and for case selection, improved planning and mapping of valve-in-valve procedure. The challenge was represented by leaflets enhancement because of highly noised CT images.

Contrast-enhanced ECG-gated CT scan was performed in patients with degenerated aortic bioprostheses before reoperation (in-vivo images). Different methods for noise reduction were tested and proposed. 3D reconstruction of bioprostheses components was achieved using stick based region segmentation methods. After reoperation, segmentation methods were applied to CT images of the explanted prostheses (ex-vivo images).

Noise reduction obtained by improved stick filter showed best results in terms of signal to noise ratio comparing to anisotropic diffusion filters. All segmentation methods applied to the best phase of in-vivo images allowed 3D bioprosthetic leaflets reconstruction. Explanted bioprostheses CT images were also processed and used as reference. Qualitative analysis revealed a good concordance between the in-vivo images and the bioprostheses alterations. Results from different methods were compared by means of volumetric criteria and discussed. A first approach for spatio-temporal visualization of 3D+T images of valve bioprosthesis has been proposed. Volume rendering and motion compensation techniques were applied to visualize different phases of CT data. Native valve was also considered.

ECG-gated CT images of aortic bioprostheses need a preprocessing to reduce noise and artifacts in order to enhance prosthetic leaflets. Stick based methods seems to provide an interesting approach for the morphological characterization of degenerated bioprostheses.

Key Words: image enhancement, segmentation, visualization, aortic bioprosthesis, prosthetic degeneration, valve-in-valve.

Contents

I. INTRODUCTION....1

II. CONTEXT....5

2.1 AORTIC VALVE BIOPROSTHESES....5

2.1.1 Types of Devices....6

2.1.2 Mechanisms of Bioprosthesis Failure....13

2.2 “VALVE-IN-VALVE” PROCEDURE....19

2.3 3D CARDIAC IMAGING....23

2.4 MULTE SLICE CT MSCT FOR CARDIAC IMAGING....25

2.4.1 ECG gated cardiac CT....25

2.4.1.1 General principles....25

2.4.1.2 Cardiac gating....28

2.4.1.3 Clinical indications....32

2.5 CONCLUSIONS AND PROPOSED APPROACH....34

REFRENCES....36

III. PREPROCESSING....39

3.1 NOISE AND ARTIFACT ANALYSIS....40

3.1.1 Noise and metal artifacts in MSCT images....40

3.1.2 Motion-related imaging artifacts....41

3.1.3 Spatial resolution....41

3.2 STATE OF THE ART: MSCT IMAGE PREPROCESSING....43
3.2.1 Metal artifacts reduction....43
3.2.2 Noise reduction....44
3.2.2.1 Hessian based filters....45
3.2.2.2 Partial differential equations (PDE) based filters....49
3.2.2.3 Noise reduction in LDCT images....53
3.3 ROI DEFINITION....55
3.4 DENOISING....59
3.4.1 Anisotropic Diffusion Filters....63
3.4.2 Stick Filter....65
3.4.2.1 Original Stick filter....65
3.4.2.2 Stick based preprocessing....67
3.5 RESULTS....75
3.5.1 Degeneration assessment at reoperation....75
3.5.2 Results of denoising....79
3.6 CONCLUSION....86
REFERENCES....87

IV. SEGMENTATION 91

4.1 STATE OF THE ART....92
4.1.1 Boundary-based (Contour-based) methods....93
4.1.2 Region based methods....94
4.1.3 Model based methods 96
4.1.4 Segmentation and visualization....97
4.2 METHODS....99
4.2.1 Isotropic region growing....99
4.2.2 Stick region growing....100

4.2.3 Stick exhaustive search.....106
4.3 RESULTS.....108
4.4 VOLUMETRIC ANALYSIS.....117
4.5 DISCUSION.....120
REFERENCES.....125

V VISUALIZATIONS 127
5.1 STATE OF THE ART.....129
5.1.1 Rendering.....129
5.1.1.1 Ray tracing.....131
5.1.1.2 Maximum intensity projection (MIP).....132
5.1.1.3 Direct volume rendering.....132
5.1.2 Camera positioning.....134
5.2 METHODS.....136
5.2.1 Motion artifact correction and grey level normalization.....137
5.2.2 Rendering.....141
5.2.3 Motion Compensation.....146
5.3 RESULTS.....153
5.4 CONCLUSION.....158
REFERENCES.....159
VI CONCLUSION AND PERSPECTIVES.....163

I – INTRODUCTION

During the last decade, the relative use of bioprosthetic aortic valves has clearly increased. Improvements in surgical techniques and valve durability are likely to have fueled this increase. On the other hand, over the last 2 decades, the mortality risk of redo aortic valve surgery has decreased similarly. The operative mortality for an elective redo aortic valve surgery is reported to range from 2% to 7%. Together with the best postoperative quality of life, these good surgical results contribute to the large diffusion of bioprostheses implantation even in younger patients. This phenomenon, associated to the increased life expectancy in industrialized countries, will probably show its consequences in the next years when a large number of elderly patients with associated comorbidities will need a re-intervention for bioprosthesis degeneration. Literature data show that mortality rate can increase to more than 30% in high-risk and non-elective patients. With the introduction of the transcatheter aortic valve to treat native aortic valve stenosis in high or prohibitive surgical risk patients through a less invasive technique, medical community has discovered a seducing but still emergent option to treat bioprosthesis failure in the same kind of patients. In fact transcatheter valve implantation avoids re-sternotomy and cardiopulmonary bypass and can potentially reduce resource utilization by accelerating patient recovery and reducing length of hospital stay. Preliminary results showed that this “valve-in-valve” procedure is feasible, but additional data should be verified to definitively accept this less invasive option. However, even if not yet officially recognized from authorities and manufacturers, the general feeling and the ‘real life’ practice consider this procedure as a potential treatment and multiple small series are going to be reported. Because of the best quality of life for patients after bioprosthetic aortic valve replacement, cardiac

surgeons are implanting today more and more biological devices, even in younger patients, taking into account the possibility of a transcatheter procedure in case of degeneration. Indeed, this “accepted future option” is responsible for a further diffusion of bioprostheses implantation in younger patients with consequent increasing incidence of failure in the next years.

The most frequent failure modality for bioprostheses is represented by leaflet degeneration. The current reference standard for follow-up in patients after aortic valve replacement remains trans-thoracic echocardiography, with trans-esophageal exploration in case of questionable findings at trans-thoracic. Echocardiography represents the gold standard for functional assessment of bioprostheses. However, both trans-thoracic and trans-esophageal echocardiography have limited usefulness for the morphological assessment, especially concerning bioprosthetic leaflets, because of their thickness and the acoustic shadowing from stent or suture ring that often prevents good leaflet visualization. Furthermore, given their two-dimensional imaging nature, it is generally impossible to directly image the leaflets that are not oriented in the imaging plane. Even the new 3D echocardiography has, for the moment, limited application on the aortic bioprostheses also because of the anterior position.

In recent years, multi-detector computed tomography has emerged as a promising tool to provide precise diagnostic information in different clinical situations, such as non-invasive evaluation of coronary disease, ventricular morphology and function and myocardial viability. Multi-detector CT can also help visualize the morphology and motion of native and diseased stenotic aortic valves and precisely measure aortic valve opening areas. Several studies suggest that multi-detector CT can help assess mechanism of dysfunction in mechanical prosthetic heart valve disorders.

Few recent studies have showed that 64 multi-detector CT allows better visualization of the bioprosthetic valve leaflets comparing to echocardiography and that it could play a role in clarifying the mechanism of dysfunction.

In general clinical practice CT scan images normally allow a tridimensional reconstruction of the structures of interest, thanks to their high spatial resolution. The 3D analysis of these images should improve the users understanding and facilitates the planning of surgical/interventional procedures on these structures.

In this context, the starting idea of this research work was that the tridimensional reconstruction of bioprosthetic structures, in particular of prosthetic leaflets, could make easier the morphological analysis of degenerated bioprostheses during normal follow-up and be used for patients' selection, improved planning and mapping of valve-in-valve procedure.

Currently, the available tools to analyze and process CT scan images do not allow an efficient and effective tridimensional reconstruction of the bioprostheses leaflets because of their thickness. Bovine pericardium and porcine valve leaflets are in fact too thin and CT images are altered by noise, stent metal artifacts and heart beat. This makes difficult the automatic analysis with available tools and new methods to process these high resolution images have to be considered.

The aim of this study was to assess the feasibility to analyze and morphologically characterize 3D MSCT images of degenerated bioprostheses. Multiple methods for noise reduction, segmentation and visualization are available in literature. After a presentation of the context of our work and the proposed approach, in the following we deal with issues of pre-processing and enhancement of CT images, of segmentation of bioprothesis, and of spatio-temporal visualization of valve structures. For each of these issues we present related works, our contributions and results.

II – CONTEXT

In this chapter, we introduce the context of our work. We more precisely present aortic valve bioprosthesis, with the types of devices and the mechanisms of bioprosthesis failure, the valve-in-valve procedure, as well as the cardiac imaging techniques, including MSCT scan and gating. At the end of this chapter, we introduce the proposed approach to analyze thin cardiovascular structures as valve leaflets from MSCT data.

2.1 AORTIC VALVE BIOPROSTHESES

Aortic valve replacement represents a standardized and safe operation for the treatment of severe aortic valve disease and, at the same time, one of the most frequent procedures in cardiac surgery. For the Euro Heart Survey on Valvular Heart Disease, that has prospectively collected data from patients with aortic valve disease and treated during the period April-July 2001 in 92 institutions from 25 european countries, the aortic valve stenosis represents the most frequent valve disease (33.9% of total), followed by mitral regurgitation (24.8%) [2.1]. Moreover, in patients with aortic valve stenosis the native valve was replaced by a bioprosthesis in 50% of cases; a mechanical prosthesis was used in 49% of patients. Homograft and autograft represented the 0.6% and the 0.4, respectively. On the contrary, in patients with aortic insufficiency a mechanical prosthesis was mostly used (76.5%), probably

because of the younger age of these patients. Observed operative mortality was 3.1% in cases of aortic valve stenosis and 3.4% in cases of aortic insufficiency.

2.1.1 Types of Devices

Bioprostheses are generally constituted by animal heterograft (porcine valve leaflets or bovine pericardium). Over the past 40 years, advances in tissue fixation methodology and chemical treatments to prevent calcification have yielded improvements in the longevity of bioprostheses. All heterograft valves are preserved with glutaraldehyde, which cross-links collagen fibers and reduces the antigenicity of the tissue. Calcification occurs when nonviable glutaraldehyde-fixed cells cannot maintain low intracellular calcium. Calcium-phosphate crystals form at the phospholipid-rich membranes and their remnants, and collagen also calcifies. Pericardial prostheses are fixed in pressure-free conditions. Porcine prostheses fixed at zero pressure retain the collagen architecture of the relaxed aortic valve cusp. Higher fixation pressures cause tissue flattening and compression with loss of transverse cuspal ridges and collagen crimp. Multiple chemical treatments have been proposed to decrease the calcification process that invariably leads to material failure and valvular dysfunction.

Today, multiple anti-calcification protocols used to treat bioprostheses are protected by patent.

Stented bioprostheses

Stented bioprostheses represent in terms of numbers, the most used biological vascular devices. This subgroup includes valvular devices realized using a rigid artificial structure (stent) including a metallic part that represents the support for the biological tissue (leaflets). First-generation bioprostheses were preserved with high-pressure fixation and were placed in the annular position. They include the Medtronic Hancock Standard and Modified Orifice and the Carpentier-Edwards Standard porcine prostheses, not more used in clinical practice.

Second-generation prostheses are treated with low or zero-pressure fixation. Several second-generation prostheses may also be placed in the supra-annular position, which allows placement of a slightly larger prosthesis in order to reach a best effective orifice area with consequent hemodynamic advantages and lower risk of patient/prosthesis mismatch. These bioprostheses have largely been used in clinical practice (Fig. 2.1); in fact most part of durability data with long term follow-up, up to 25 years, come from the analysis of patients populations having a second generation device [2.2]. Porcine second-generation prostheses include the Medtronic Hancock II and Carpentier-Edwards Supra-annular (SAV) valves. Second-generation

pericardial prostheses include the Carpentier-Edwards Perimount and Mitroflow Synergy (Sulzer Carbomedics, Austin, TX) valves.

Fig. 2.1: Second generation bioprostheses

Third generation prostheses (Fig. 2.2) incorporate zero- or low-pressure fixation with anti-mineralization processes that are designed to reduce material fatigue and calcification. They include the porcine Medtronic Mosaic and St. Jude Epic constituted by porcine aortic valve leaflets mounted into a low profile stent, and the pericardial Carpentier Edward Magna, Sorin Mitroflow and St. Jude Medical Trifecta. The last two bioprostheses are characterized by pericardium mounted externally to the stent in order to obtain a larger effective orifice area with consequent better hemodynamics.

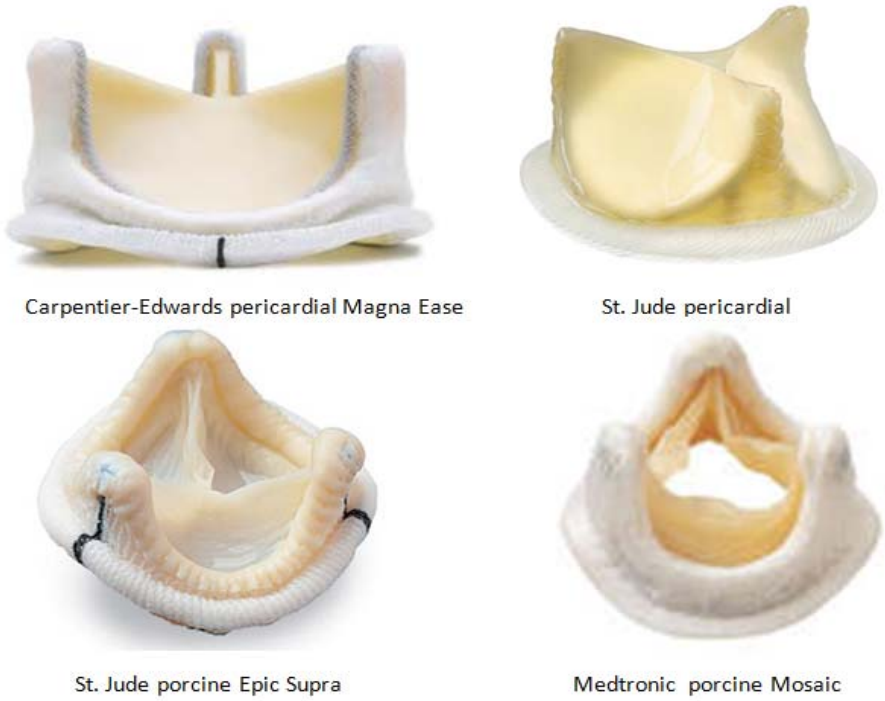

Fig. 2.2: Third generation bioprostheses

Stentless bioprostheses

Stentless porcine valves (Fig. 2.3) have gained popularity in cardiac surgery due to pioneering work by David at the Toronto General Hospital in 1988 [2.3]. Since they do not have obstructive stents and strut posts, stentless valves provide residual gradients and effective orifice areas that are similar to freehand allografts. Since stentless valves are more difficult to implant and require a longer cross-clamp time, the risks of operation must be matched to a specific benefit the patient may receive with a stentless valve. There is conflicting evidence that the use of stentless valves results in improved left ventricular mass regression over stented bioprostheses. There is also no evidence that incremental improvements in left ventricular mass provide

additional clinical benefit. Thus, the routine use of stentless bioprostheses cannot be recommended for most patients with small aortic roots with the currently available data. At this time, stentless porcine valves are most useful in a relatively younger patient with a small aortic root who is active and likely to be limited by the elevated residual gradient a stented bioprosthesis will create.

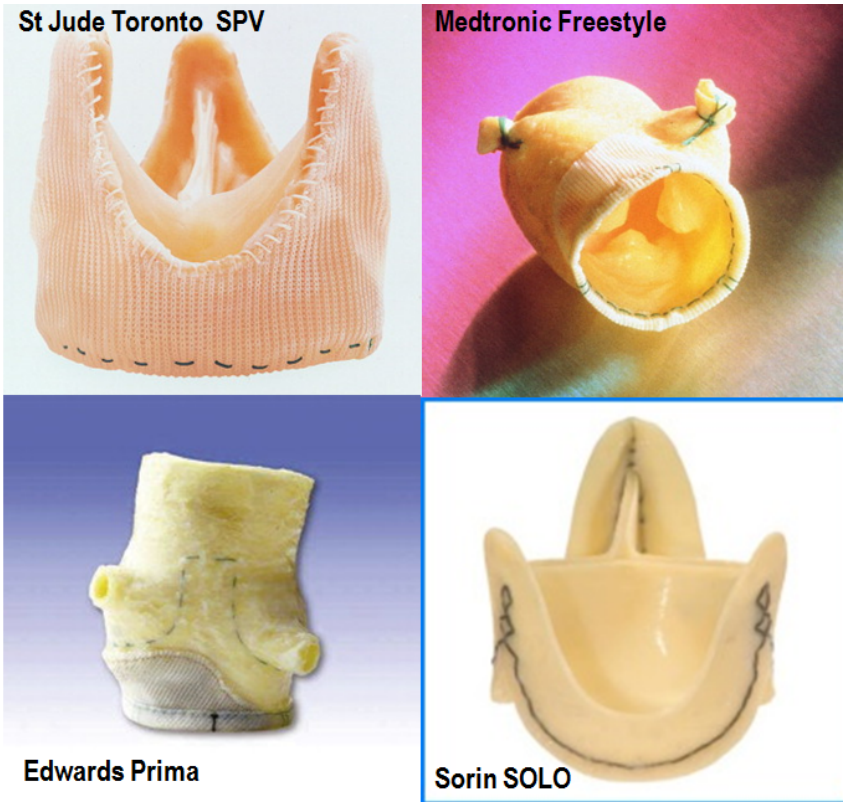

Fig. 2.3: Stentless bioprostheses

The first stentless device used in modern clinical practice was the St Jude Toronto SPV [2.4]. Other devices in this class are represented by the Medtronic Freestyle, the Edwards Prima and the Sorin Solo.

Homografts and autografts

Other substitutes that could be used to replace the aortic valve in some particular cases are the homo- and auto-grafts.

Fig. 2.4: Aortic homograft

The homograft is represented by a complete cryopreserved human aortic root (Fig. 2.4). It is real tissue transplantation and it is treated to reduce antigenicity before its implantation. After, it doesn't need immunotherapy. Implantation involves not only the diseased valve but also the aortic root with coronary arteries reimplantation, with a consequent increased operative risk comparing to simple aortic valve replacement.

The most important interest is represented by the high resistance to infections that explains their potential use in case of destroying infective endocarditis. Homografts have also been used, during a short time, for aortic root

replacement in young patients for their best durability comparing to second generation bioprostheses. However, the best results of third generation bioprostheses together with the technical difficulties to reoperate the severe calcified degenerated homografts, have contributed to strongly decrease their use in clinical practice.

The autograft is represented by the use of autologous pulmonary root to replace native aortic root. The native pulmonary root is replaced with a homograft (Ross procedure). This operation is limited to few selected cases and represents a rare choice in cardiac surgery for adults.

2.1.2 Mechanisms of Bioprosthesis Failure

In fact, the number of deaths during follow-up due to non-cardiac causes will mask the true incidence of non-fatal events related to the prosthesis (such as structural degeneration and related reoperation) [2.5-2.6].

Time-related structural valve dysfunction leading to regurgitation or stenosis is the major drawback of bioprosthetic valves. Fortunately, the vast majorities of valve failures are nonfatal and progress slowly; if identified in a timely manner, an elective redo surgery can be performed with relative safety. Structural valve dysfunction is age-dependent. In fact, it is nearly uniform by 5 years in patients younger than 35 years of age, but occurs in only 10% in those older than 65 years of age within 10 years.

Failure modes can be influenced by: 1) host metabolic pathways; 2) bioprosthesis engineering and chemistry (e.g., leaflet suturing material, stent post flexibility, prosthesis fabric covering, leaflet fixation process); and 3) mechanical loading effects (e.g., leaflet flexural stress/strain).

Broadly speaking, bioprosthetic valve failure can be the result of calcification, wear and tear, pannus formation, thrombosis, and/or endocarditis (Fig. 2.5).

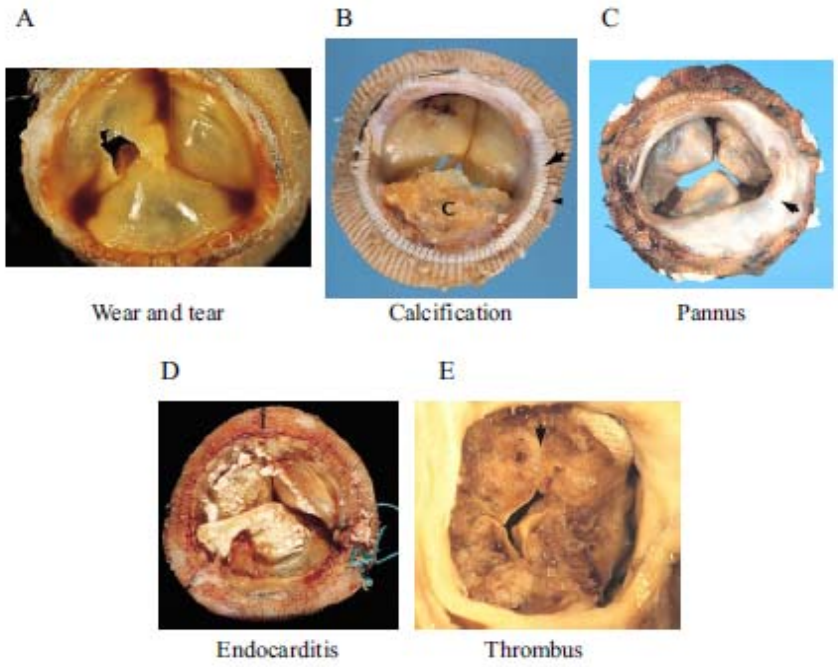

Fig. 2.5: Mechanisms of bioprosthesis failure

Leaflet tissue deterioration, whether calcific or non-calcific, is the major cause of bioprosthetic valve failure [2.7-2.10]. Although the glutaraldehyde fixation process of bioprosthetic heart valves is intended to promote tissue durability by creating stable cross links between collagen fibers and render the heterograft material biologically inert, residual glutaraldehyde-derived polymers may serve as calcium-binding sites that promote calcium-phosphate precipitates. Furthermore, toxic glutaraldehyde may result in cell death of bioprosthetic valve leaflets and host fibroblasts/macrophages. The mitochondria of dead cells, rich in phosphate, can be an additional source of calcium-binding sites. For these reasons, anticalcification treatments (e.g., Edwards ThermaFix, Medtronic AOA) serve to reduce potential binding sites

by: 1) residual glutaraldehyde substraction, 2) phospholipid extraction; and/or 3) terminal liquid sterilization. Calcific deposits have a propensity to develop in areas where leaflet flexion and stress are greatest: at the basal and commissural attachment points. Approximately three-fourths of patients with leaflet calcification and tears suffer from aortic regurgitation [2.7-2.10]. The presence of calcification is a common finding in explanted bioprosthesis, especially in the first and second generation devices. Schoen and colleagues proposed a classification of bioprostheses calcifications (Tab. 2.1) [2.11-2.12].

Tab. 2.1: grading of calcification in bioprostheses degeneration

Grading of Calcification (Shoen et al.)	
Grade 0	No calcification
Grade 1	Small, isolated calcific nodules
Grade 2	Moderate, patchy nodules up to 1mm in length
Grade 3	Severe nodules up to 2 mm in length
Grade 4	Very severe, diffuse nodules capable of puncturing through the cusp surface

Leaflet tears represent a very frequent failure modality. Even for this type of lesion a classification has been proposed (Tab. 2.2) [2.13].

Tab. 2.2: grading of tears in bioprostheses degeneration

Grading of Tears (According to Ishihara et al.)	
Type I	Linear tears involving the free edge of cusp
Type II	Linear tears running parallel to the sewing ring, along the basal regions of cusp
Type III	Large round or oval perforations occupying the central regions of the cup
Type IV	Small and multiple pinhole like fenestrations in the cusp

The prolapse of one or more valve leaflets is considered by some authors as a specific lesion, while others will consider it as a consequence of a leaflet tear. However, the prolapse consists in the excessive movement of one or more valve leaflets toward the outflow of the left ventricle. The lesion determining the prolapse can be an important vertical tear of the leaflet free edge or a disconnection of the leaflet from its suture line on the stent (Fig. 2.6).

Fig. 2.6: leaflet tears in degenerated porcine bioprosthesis

Pannus represents a host tissue response and develops at the host-prosthesis interface. Early pannus is composed of myofibroblasts, fibroblasts and capillary endothelial cells. Overtime pannus may calcify. Some pannus formation over the suture is normally expected and functions to form a non-thrombogenic surface. When exuberant, however, it may extend to the leaflets and contribute to leaflet stiffening and dysfunction. Pannus formation is

usually mild and can be detected in the vast majority (~70%) of explanted valves.

A classification has also been proposed for this type of lesion (Tab. 2.3) [2.14]; according to this classification, only in the two last grades (a pannus which extends for more than 2 mm inside the effective orifice area) will result in significant hemodynamic effects and may result in valve dysfunction.

Tab. 2.3: grading of pannus in bioprostheses degeneration

Grading of Pannus (Modification from Butany et al.)	
Grade 0	No pannus
Grade 1	Mild and involving part of the circumference of the valve ring
Grade 2	Moderate and extending up to 2 mm onto the surface of the cusp
Grade 3	Severe and extending beyond 2 mm of onto the surface of the cusp
Grade 4	Very severe and surrounding the flow and nonflow surfaces of the cusp, causing the cusp to shorten

It should be noted that a mild pannus can be virtually observed in all bioprostheses after the first year post-implantation. It has been suggested also a temporal correlation with the anatomo-pathological grade of pannus. In fact, in a series of explanted pericardial bioprostheses (Carpentier-Edwards Perimount) [2.14], the prostheses presenting a pannus grade 1 were implanted 4.4 years before, while valves showing a pannus grade 2 were implanted 9.1 years before. A similar period of time had elapsed between the implant and the evidence of pannus grade 3 or 4. This suggests that the operating time of the valve is not sufficient to justify the size of the pannus overgrowth. Some additional factors are involved in the pathogenesis of the

pannus (probably hemodynamic, metabolic and immune) and these factors vary from patient to patient and realize the differences between the various cases. These mechanisms, however, remain largely unknown.

Thrombosis and endocarditis occur less frequently than the aforementioned modes of bioprosthetic failure, occurring at a rate of 0.2% per year and 1.2% per year, respectively [2.15]. They represent usually sub-acute or acute failure modalities and they need a rapid treatment comparing to other leaflets failures.

Prosthetic valve thromboembolism is a complex phenomenon, occurring through an interaction between prosthesis type and patient-related factors. The pathologic events leading to thromboembolism start immediately after surgery. Damaged paravalvular tissue and deposition of fibrinogen on the valve surface activate platelets as soon as blood starts flowing across the valve leading to immediate platelet adhesion and aggregation. Within 24 h after surgery, platelet deposition on the Dacron sewing ring can be imaged radiographically.

2.2 VALVE-IN-VALVE PROCEDURE

Although, as described above, the risk of reoperation of bioprosthesis is gone considerably decreasing during the last few years (down to 2% of reported operative mortality), on the other hand it is known that the mortality rate can reach up to 30% for patients at high surgical risk because of multiple co-morbidities and non-elective conditions.

Already used for the treatment of patients with native aortic valve stenosis and considered at excessive surgical risk, the TAVI procedure (Transcatheter Aortic Valve Implantation) has been proposed for use in the context of the bioprosthesis degeneration in patients similarly considered at excessive operative risk.

Such a procedure (called Valve-in-Valve) provides for the implantation of a transcatheter valve within the degenerated bioprosthesis already in place, which is therefore not removed but, similarly to what happens in the TAVI procedure for the native aortic valve, constitutes the support for the transcatheter valve (Fig. 2.7).

Fig. 2.7: Edwards Sapien transcatheter valve deployed into a bioprosthesis

This procedure is still not yet recognized as indication by the producers of the transcatheter valve devices and by regulatory authorities of the United States of America. Currently, the major manufacturers of transcatheter valve (Edwards Inc. and Medtronic Inc.) have applied to obtain the CE mark for the Valve-in-Valve procedure; for this purpose clinical trials are in progress in order to verify the reproducibility and the safety of this procedure in sufficiently large series of patients. The first clinical experiences have demonstrated the technical feasibility.

In 2007, Wenaweser et al. [2.16] reported the first case of a transcatheter valve implanted into a degenerated surgical aortic bioprosthesis using a Medtronic CoreValve system (Fig. 2.8).

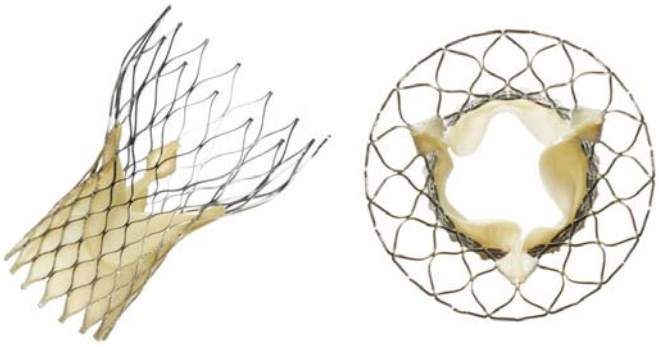

Fig. 2.8: Medtronic CoreValve transcatheter valve

Since then, numerous case reports have been described also with the use of the other available device Edwards Sapien (Fig. 2.9) and through different accesses as trans-femoral, trans-apical and trans-axillary [2.17-2.25].

Fig. 2.9: Edwards Sapien transcatheter valve

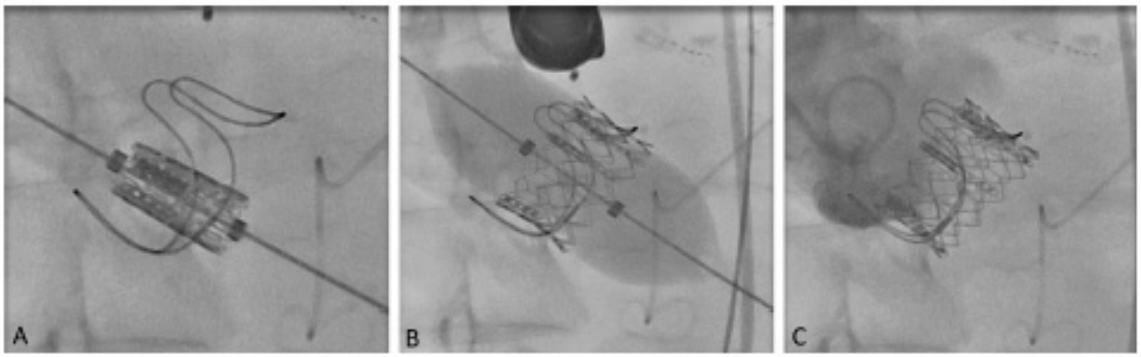

Fig. 2.10: valve-in-valve procedure using Edwards Sapien transcatheter valve. Intraoperative fluoroscopy during (A) device positioning, (B) valve deployment and (C) control aortography

For the planning and implementation of the Valve-in-Valve procedure (Fig. 2.10), the assessment of exact dimensions and mechanical characteristics of the degenerated bioprosthesis inside which we intend to expand the transcatheter prosthesis is foundamental. In a stented bioprosthesis we can distinguish the external diameter (A) from the internal diameter (B) of the stent and from the diameter of the suture ring (D), as shown in Fig 2.11.

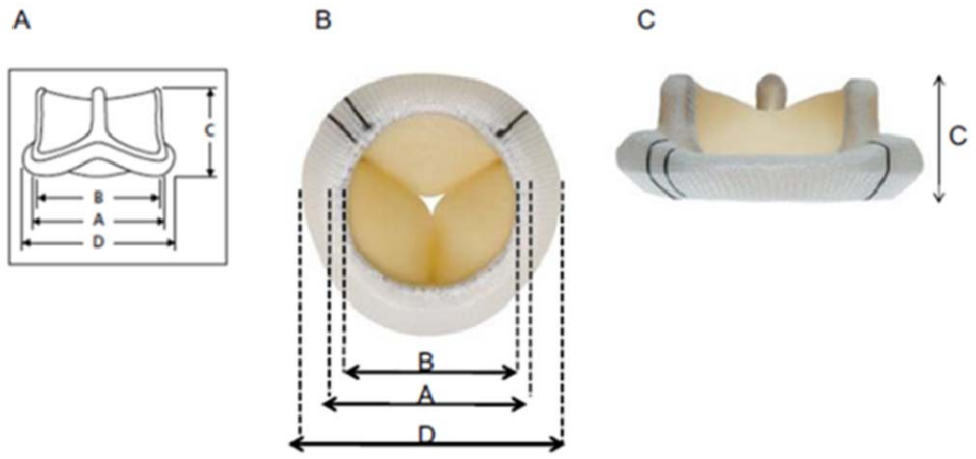

Fig. 2.11 : Bioprosthesis different diameters can change according to valve type

It is evident that the internal diameter of the stent has the greater importance for the size selection of the transcatheter prosthesis to implant. MSCT allow to accurately measure the diameter of the landing zone of the transcatheter prosthesis.

2.3 3D CARDIAC IMAGING

Cardiac imaging techniques have had a great development in the last years. In this section, we present the main 3D imaging modalities and we focus on multi-slices CT (MSCT) techniques (imaging and gating).

Threedimensional (3D) echocardiography offers the ability to improve and expand the diagnostic capabilities of cardiac ultrasound. However, as with any emerging technology, the enthusiasm to embrace a new technique must be tempered by a critical appraisal of the evidence supporting its use. At the moment, it represents a new safe, non-invasive imaging modality that is complementary and supplementary to 2D imaging and that provides improved accuracy and reproducibility over 2D methods for left ventricular volume and function calculation and for the mitral valve functional assessment [2.26]. Limitations of 3D echocardiography includes poor visualization of anterior structures of the heart, suboptimal images due to poor ECG triggering in patients with arrhythmias, reduced spatial and temporal resolution with narrow angled acquisitions as well tissue dropout. Anterior cardiac structures such as the aortic and tricuspid valves due to their increased distance from the probe cannot be visualized as well as posterior structures such as the mitral valve [2.27]. Finally, at the moment echocardiography remain the gold standard to analyze aortic bioprosthesis function, but can't be used for the morphological tridimensional analysis of bioprosthetic leaflets yet.

Magnetic resonance imaging (MRI) [2.28] is an imaging methodology based on aligning the spin axis of nuclei within molecules of the object being visualized using both powerful superconducting magnets and radio frequency signals and detectors. MRI in cardiac imaging is growing, because its outstanding differentiates in soft tissues. There is a promising future in cardiac MRI by more efficient scans, increasing availability of scanners and more widespread knowledge about its clinical application. The quality of MRI Images may be reduced by the continuous movement of vascular structures and current implementations for cardiology uses are sometimes limited by lengthy protocols, claustrophobia and contraindications based on some complex metallic implants such as metal stent of aortic valve prosthesis.

Computed tomography (CT) angiography [2.29] is an imaging methodology using a ring-shaped machine with an X-Ray source spinning around the circular path so as to calculate (Generally use Fourier filter back projection) the X-Ray density voxels inside circular path. Because of the incredible developments in CT technology, Cardiac CT imaging is growing. Currently, multi-slicer computed tomography (MSCT), or known as “multi-detectors CT (MDCT)”, have 64 or more detectors in nowadays. They are allowing to make a cardiac imaging in a very short time: we can get 3D+T cardiac image sets.

2.4 MULTI-SLICE CT (MSCT) FOR CARDIAC IMAGING

2.4.1 ECG-Gated Cardiac CT [2.30]

MSCT was presented to cardiac imaging in 1999. The current generation of MSCT systems is capable of acquiring 4 to 64 sections of the heart simultaneously with ECG gating in either a prospective or retrospective mode. MSCT differs from single detector–row helical or spiral CT systems principally by the design of the detector arrays and data acquisition systems, which allows the detector arrays to be configured electronically to acquire multiple adjacent sections simultaneously. In the current 64-row MSCT systems, the thickness of slice can be of 0.6 mm at least.

2.4.1.1 General Principles

The basic principles of MDCT are relatively simple (Fig. 2.12 A). The X-ray point source and the detector array are placed on opposite sides of the patient on a ringlike structure called the gantry. The gantry rotates around the patient, who is located on a table at its center. The table moves at constant speed along the axis of the gantry. X rays are emitted toward the patient, penetrate the patient, and are captured by one or more detectors. This process generates a series of helical projections of the patient’s attenuation properties.

Images representing X-ray attenuation at each point in the volume traversed by the photons are then mathematically reconstructed from the helical projection data (Fig. 2.12 B).

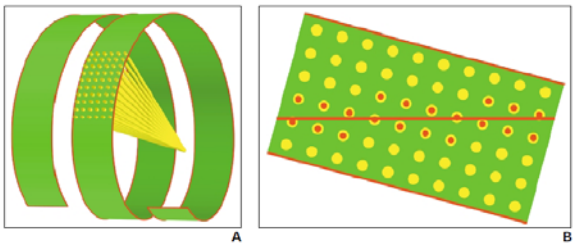

Fig. 2.12: Drawings show helical projections from MDCT. A, Detectors follow 3D helical path, with table advancing at constant speed while gantry is rotating. Tube emits X-ray radiation (*yellow*) that is recorded by detectors. Resulting set of projections has helical configuration in space. B, Images are reconstructed from projection data by linear interpolation from projections closest to image plane. Advanced algorithms correct for cone-beam geometry.

Effective slice thickness using a single-slice detector scanner is determined by collimation, whereas in multidetector scanners it is determined by both the detector configuration and the reconstruction method. The table travel per complete rotation of the gantry divided by the X-ray beam width is called the “beam pitch.” The beam pitch conforms to the current industry standard of pitch. In multidetector scanners, another definition of pitch is sometimes used: the table travel per complete rotation of the gantry divided by the detector width, called the “detector pitch.” With a (beam) pitch of 0, there is no table motion and scanning is axial. With a pitch of 1, the table displacement for each rotation is equal to the *z*-axis dimension of the array of active rows of detectors. A pitch greater than 1 implies gaps in the helix of projections, whereas a pitch between 0 and 1 implies overlap between the projections (Fig. 2.13).

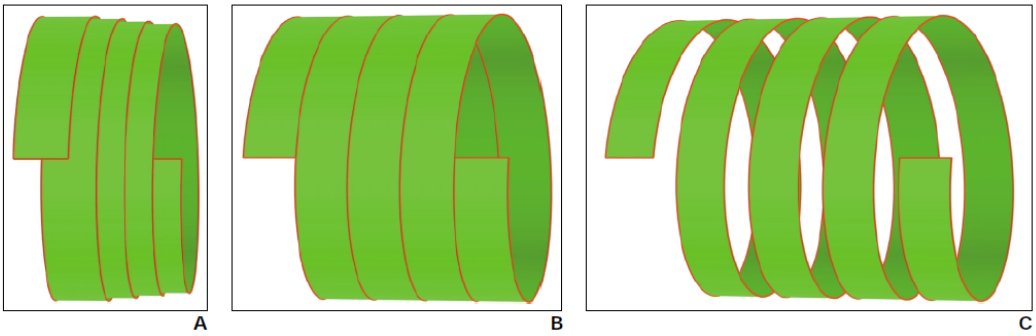

Fig. 2.13: Drawings show that relation of table movement with respect to gantry rotation is described by beam pitch. A, Pitch of 0.5:1 indicates 50% overlap in projection data. B, Pitch of 1:1 indicates neither overlap nor gap in data. C, Pitch of 1.5:1 indicates 50% gap in data.

Images are reconstructed from linear interpolation of projection data from rays that are the closest to the image plane, using algorithms to correct for cone-beam geometry. A minimum of 180º of projection data are mathematically required to reconstruct a complete image. Thus, slice thickness increases with pitch, which determines how much the table travels during a 180º rotation. The thinnest slice is equal to the height of a single row of detectors (the detectors are actually wider than the slice to compensate for geometric magnification).

Thicker slices can be generated mathematically by combining the thinner slices. The determinants of in-plane resolution are focal spot size, detector width and geometry, reconstruction algorithm, and image matrix size. The determinants of longitudinal *z*-axis resolution are focal spot size, detector height and collimation, and reconstruction algorithm. The determinants of temporal resolution are gantry rotation speed and reconstruction algorithm.

2.4.1.2 Cardiac Gating

Gating techniques are used to improve temporal resolution and minimize imaging artifacts caused by cardiac motion. Two approaches to cardiac gating are typically used: prospective ECG triggering and retrospective ECG gating. The least cardiac motion occurs during diastole, when the ventricles are passively filling. A comparison between prospective and retrospective ECG-gating is presented in Tab. 2.4 [2.31].

Tab. 2.4: Comparison of different parameters between prospective and retrospective ECG-gating.

Parameters to be compared	Retrospective ECG-gating		Prospective ECG-gating	
	Pros	Cons	Pros	Cons
Scanning protocols	Axial helical scan allows acquisition of volume data	Exposure takes place during the entire cardiac cycle and only a portion of data is used for reconstruction	Exposure only occurs at a selected cardiac cycle (late diastolic phase)	Axial non-helical scan with most of the manufacturers; thus no volume data is available
Image quality (assessable segments)	98-100%	Affected by heavy calcification and high heart rate	95-99%	Affected when heart rate is >70 bpm
Effect of heart rate	Diagnostic accuracy is high even in higher heart rate; Independent of heart rate with dual source CT	Diagnostic accuracy slightly decreases with increasing heart rate (70-100 bpm)	High assessable segments and diagnostic value in low heart rate	Limited to heart rate <70 bmp; Limited to regular and stable heart rate
Diagnostic value	High sensitivity and specificity, especially very high negative predictive value	Sensitivity is affected by heavy calcification	High diagnostic accuracy, although the data is scarce at the moment	Very limited data available
Radiation dose	Online tube current modulation could reduce radiation dose	High radiation dose with range of 7.6-31.8 mSv	Significant reduction of with range of 2.1-9.2 mSv	
Cardiac functional assessment	Available as volume data are acquired		Functional assessment is only available with 256- or 320-slice CT	Unavailable with 64-slice CT scanners

Prospective ECG triggering uses the ECG signal to control scanning, so that X rays are generated and projection data are acquired only during cardiac diastole, more than half the rotation of the gantry. The total number of slices

produced per heartbeat during this half rotation of the gantry is proportional to the number of rows of active detectors. Because an axial scanning method (rather than helical) is typically used and the table has to move by the total collimation width after each acquisition, one heartbeat typically has to be skipped between each acquisition. About 12 cm of scanning is required to cover most heart sizes, which requires approximately 48 heartbeats for single-slice CT (5-mm collimation), 24 heartbeats for 4-slice MDCT (2.5-mm collimation each row), 12 heartbeats for 16-slice MDCT (1.25-mm collimation each row) and 6 heartbeats for 64-slice MDCT (0.625-mm collimation each row). Thus, multidetector technology can obtain the entire scan during one breath-hold. The start of the diastolic phase of the cardiac cycle is estimated from the prior three to seven consecutive heartbeats and occurs approximately 450 msec before the R wave on the ECG.

Prospective triggering techniques have important limitations. They are sensitive to heart rate changes and arrhythmias, but they have limited spatial *z*-axis resolution in order to cover the entire heart in a single breath-hold. They are effective only for heart rates of less than 70 beats per minute and perform poorly with arrhythmias, such as in atrial fibrillation. To overcome these limitations, retrospective ECG gating techniques are commonly used, at the expense of a higher radiation dose.

Retrospective gating techniques allow faster continuous cardiac volume coverage, improved *z*-axis resolution, and imaging of the entire cardiac cycle

for functional analysis. In retrospective techniques, partially overlapping MDCT projections are continuously acquired, and the ECG signal is simultaneously recorded. Algorithms are then used to sort the data from different phases of the cardiac cycle by progressively shifting the temporal window of acquired helical projection data relative to the R wave (Fig. 2.14).

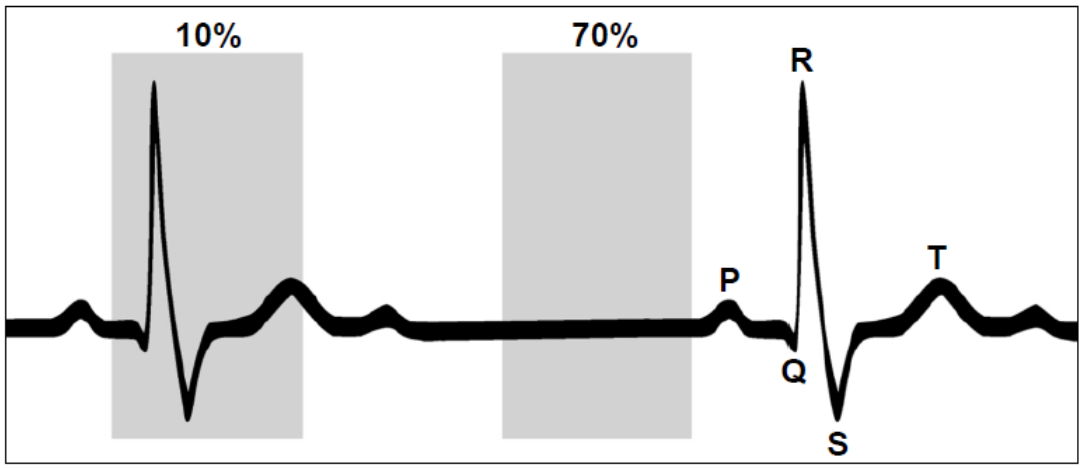

Fig. 2.14: Temporal window for reconstruction from projection data is approximately 250 msec. Drawing shows that center of window can be located anywhere during heart cycle. Left box has its center at 10% of R-R interval, which is during systole. Right box has its center at 70% of R-R interval, which is during diastole and is most common motion-free imaging temporal window for heart.

Every position of the heart must be covered by a detector row at every point during the cardiac cycle. This means that the scanner table must not advance more than the total width of the active detectors for each heartbeat. Helical pitch can be varied proportionally to the heart rate to achieve continuous volume coverage. Typical pitch for an average heart rate of 70 beats per minute is 0.3:1, with a total scanning time of about 20 sec for a 16-slice MDCT scanner using 0.625-mm collimation.

Two main algorithmic approaches are used to perform retrospective cardiac gating: partial scanning and segmented adapted scanning. To reconstruct an image, a minimum helical projection data segment of 180º must be available for every fan angle, corresponding to a rotation of 180º plus the breadth of the fan beam, so approximately two thirds of a full gantry rotation is required (Fig.2.15 A). This technique is called *partial scanning*. Temporal resolution is therefore two thirds of rotation time. Parallel beam geometries and rebinning techniques can be used to decrease the minimum data segment to 180º, with a temporal resolution of half the rotation time, or 250 msec for 16-slice MDCT scanners. The partial scanning technique is typically used in patients with heart rates between 40 and 75 beats per minute. To improve temporal resolution, *segmented adaptive reconstruction* can be used, which involves combining shorter segments of projection data from two of more subsequent cardiac cycles (Fig. 2.15 B). Temporal resolution is equal to that of the longest projection data segment. Maximum values for temporal resolution are 125 msec for segmentation over two cardiac cycles and 65 msec over four cardiac cycles. Either volume coverage or longitudinal resolution may need to be reduced to maintain a low pitch and still scan in a single breath-hold.

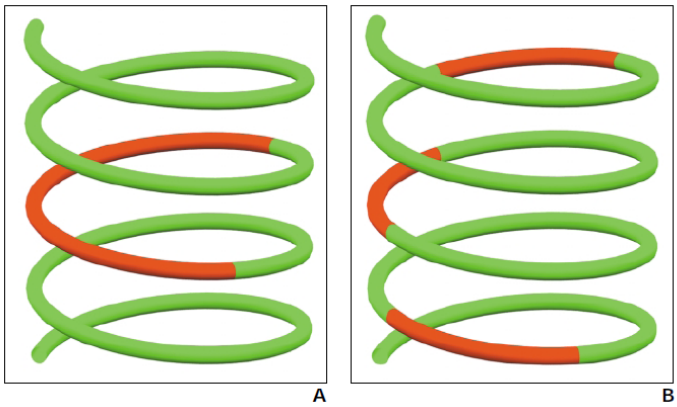

Fig. 2.15: Drawings show two types of retrospective reconstruction algorithms. A, In partial scanning algorithm, continuous segment of projection data at single heartbeat is used to reconstruct image. B, In segmented adaptive algorithm, different segments of projection data from same phase of cardiac cycle at successive heartbeats are used to reconstruct image. Cardiac cycle and gantry rotation must not be synchronized for different segments to cumulatively cover large enough range of projection angles to reconstruct image from data.

Several elements of cardiac CT can be optimized to produce the best possible images at the lowest dose of radiation, such as patient position, heart rate, pitch, collimation and dosimetry.

2.4.1.3 Clinical Indications

The two most important clinical indications for cardiac CT are calcium scoring and coronary CT angiography. CT may also be used to characterize coronary plaque and to evaluate cardiac function, myocardial perfusion, infarcts, tumors, pericardial disease, postsurgical complications and congenital malformations. The exact roles of coronary CT angiography for atherosclerotic heart disease and patient selection criteria for coronary CT angiography are under investigation.

2.5 CONCLUSION AND PROPOSED APPROACH

With the advent of trans-catheter valve we are witnessing the birth of a new era for the management of valve diseases based on imaging. Imaging modalities are becoming more and more necessary for new generation practitioners because the good structural and morphological understanding allow a better planning of the procedures. This translates into a greater awareness of the pathology and should consequently facilitate clinical decision improving results.

The functional assessment of bioprostheses after aortic valve replacement is represented by echocardiographic parameters that allow patients follow-up together with the clinics. But the reliability of echocardiography is not the same when we look at the morphological understanding of the bioprosthetic degeneration that could be useful during standard follow-up as well as for the decision making of a therapeutic solution. Failure mechanisms such as leaflet calcifications or tears, pannus formation or leaflets thrombosis should be preoperatively detected in order to choose the best adapted treatment.

In this context, some methods to allow 3D leaflets analysis should be considered. It becomes necessary to provide morphological images of aortic bioprostheses, easy to be realized and processed, in order to obtain information about anatomical images weakly contrasted.

MSCT scan images of the bioprosthesis can be easily obtained because all patients with a failing aortic bioprosthesis, waiting for reoperation or considered for a valve-in-valve procedure receive a MSCT for complementary information such as coronary assessment, cardiac structures relations or vascular assessment.

The overall approach (Fig. 2.16) we propose to analyze thin cardiovascular structures as valve leaflets in MSCT data, is composed of: (a) the definition of a Region of Interest (ROI) depending on the type of bioprosthesis stent implanted in the patient, (b) a preprocessing step to reduce noise in the original CT images, (c) the segmentation of valve bioprosthesis components mainly based on a region growing process and (d) the visualization of the bioprosthesis components.

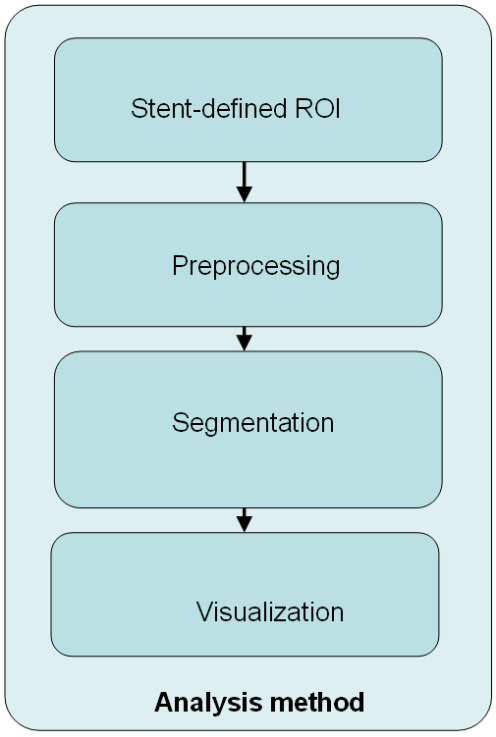

Fig 2.16: Bioprosthetic aortic valve analysis from MSCT data.

REFERENCES

[2.1]. Iung B, Baron G, Butchart EG, et al. A prospective survey of patients with valvular heart disease in Europe: the Euro Heart Survey on valvular heart disease. Eur Heart J 2003;24:1231-43.

[2.2]. Ruggieri VG, Flecher E, Anselmi A, et al. Long-Term Results of the Carpentier-Edwards Supraannular Aortic Valve Prosthesis. Ann Thorac Surg. 2012 Jul 7.

[2.3]. Lupinetti FM, Lemmer JH Jr. Comparison of allografts and prosthetic valves when used for emergency aortic valve replacement for active infective endocarditis. Am J Cardiol 1991; 68: 637.

[2.4]. David TE, Armstrong S, Sun Z. The Hancock II bioprosthesis at ten years. Ann Thorac Surg 1995;60:S229-34.

[2.5]. Grunkeimeier G, Jin R, Eijkemans J et al. Actual and actuarial probabilities of competing risks: apples and lemons. Ann Thorac Surg 2007;83:1586-1592.

[2.6]. Grunkemeier G, Takkenberg J, Jamieson WR et al. Reporting “actual freedom” should not be banned. J Thorac Cardiovasc Surg 2008;135:460-462.

[2.7]. Butany J, Nair V, Leong SW, et al. Carpentier-Edwards Perimount valves—morphological findings in surgical explants. J Card Surg 2007;22:7–12.

[2.8]. Butany J, Vanlerberghe K, Silver MD. Morphologic findings and causes of failure in 24 explanted Ionescu-Shiley low-profile pericardial heart valves. Hum Pathol 1992;23:1224 –33.

[2.9]. Roselli EE, Smedira NG, Blackstone EH. Failure modes of the Carpentier-Edwards pericardial bioprosthesis in the aortic position. J Heart Valve Dis 2006;15:421–7, discussion 427–8.

[2.10]. McGonagle-Wolff K, Schoen FJ. Morphologic findings in explanted Mitroflow pericardial bioprosthetic valves. Am J Cardiol 1992;70:263–4.

[2.11]. Schoen FJ, Levy RJ: Founder's Award, 25th Annual Meeting of the Society for Biomaterials, perspectives. Providence, RI, April 28-May 2, 1999. Tissue Heart Valves: current challenges and future research perspectives. J Biomed Mater Res 1999;47:439.

[2.12]. Schoen FJ, Levy RJ, Nelson AC et al. Onset and progression of experimental bioprosthetic heart valve calcification. Lab Invest 1985;52:523.

[2.13]. Ishihara T, Ferrens VJ, Boyce SW et al. Structure and classification of cuspal tears and perforations in porcine bioprosthetic cardiac valves implanted in patients. Am J Cardiol 1981;48:665-78.

[2.14]. Butany J, Nair V, Leong S et al. Carpenier-Edwards Perimount valves – morphological findings in surgical explants. J Card Surg 2007;22:7-12.

[2.15]. Grunkemeier GL, Jin R, Starr A. Prosthetic heart valves: objective performance criteria versus randomized clinical trial. Ann Thorac Surg 2006;82:776–80.

[2.16]. Wenaweser P, Buellesfeld L, Gerckens U et al. Percutaneous aortic valve replacement for severe regurgitation in degenerated bioprosthesis: the firs valve in valve procedure using the CoreValve revalving system. Catheter Cardiovasc Interv 2007;70:760-4.

[2.17]. Klaaborg KE, Egeblad H, Jakobsen CJ et al. Transapical transcatheter treatment of a stenosed aortic valve bioprosthesis using the Edwards Sapien transcatheter heart valve. Ann Thorac Surg 2009;87:1943-6.

[2.18]. Attias D, Himbert D, Hvass U et al. Valve-in-valve implantation in a patient with stentless bioprosthesis and severe intraprosthetic aortic regurgitation. J Thorac Cardiovasc Surg 2009;138:1020-2.

[2.19]. Schmoeckel M, Boeckstegers P, Nikolau K et al. First successful transapical aortic valve implantation after aortic allograft replacement. J Thorac Cardiovasc Surg 2009;138:1016-7.

[2.20]. Dainese L, Fusari M, Trabattoni P et al. Redo in aortic homograft replacement: transcatheter aortic valve as a valid alternative to surgical replacement. J Thorac Cardiovasc Surg 2010;139:1656-7.

[2.21]. Ferrari E, Marcucci C, Sulzer C et al. Which available transapical transcatheter valve fits into degenerated aortic bioprosthesis? Interact Cardiovasc Thorac Surg 2010;11:83-5.

[2.22]. Webb JG, Wood DA, Ye J et al. Transcatheter valve-in-valve implantation for failed bioprosthetic heart valves. Circulation 2010;121:1848-57.

[2.23]. Seiffert M, Franzen O, Conradi L et al. Series of transcatheter valve-in-valve implantations in high-risk patients with degenerated bioprostheses in aortic and mitral position. Catheter Cardiovasc Interv 2010;76:608-15.

[2.24]. Ruggieri VG, Bedossa M, Verhoye JP. Urgent transaxillary valve-in-valve procedure using the Edwards 16F expandable introducer. Catheter Cardiovasc Interv 2012 in press.

[2.25]. Verhoye JP, Ruggieri VG, Paramythiotis A et al. Trans-apical valve in homograft. J Heart Valve Dis 2012 in press.

[2.26]. Hung J, Lang R, Flachskampf F, Shernan S.K, McCulloch M.L, Adams D.B, Thomas J, Vannan M, Ryan T. 3D Echocardiography: A Review of the Current Status and Future Directions. J Am Soc Echocardiogr 2007;20:213-233.

[2.27]. Sugeng L., Shernan S.K., Weinert L., Shook D., Raman J., Jeevanandam V., et-al. Real-time three-dimensional transesophageal echocardiography in valve disease: comparison with surgical findings and evaluation of prosthetic valves. J Am Soc Echocardiogr. 2008; 21:1347-54.

[2.28]. Hendee.W., Morgan.C., Magnetic Resonance Imaging Part I—Physical Principles. West J Med. 1984: 141 (4): 491–500.

[2.29]. Matthew J. B., Stephan A., Roger S. Blumenthal et al. Assessment of Coronary Artery Disease by Cardiac Computed Tomography. Circulation. 2006;114:1761-1791.

[2.30]. Desjardins B, Kazerooni E.A. ECG-Gated Cardiac CT. AJR:182, April 2004 : 993-1010.

[2.31]. Sun Z. Multislice CT angiography in cardiac imaging: prospective ECG-gating or retrospective ECG-gating? Biomed Imaging Interv J 2010; 6(1):e4.

III - PREPROCESSING

Multi Slice Computed Tomography (MSCT) shows a high spatial resolution and can also be used to acquire spatio-temporal data during the cardiac cycle. In this work we are interested in using MSCT data to analyse and to assess the morphology and pathological features of aortic valve bioprosthesis including thin structures such as leaflets. Fig. 3.1 illustrates original noisy MSCT images showing stent with high density and possible artifacts (A), low contrasted leaflets (B), calcifications on leaflets (C) and pannus under stent (D).

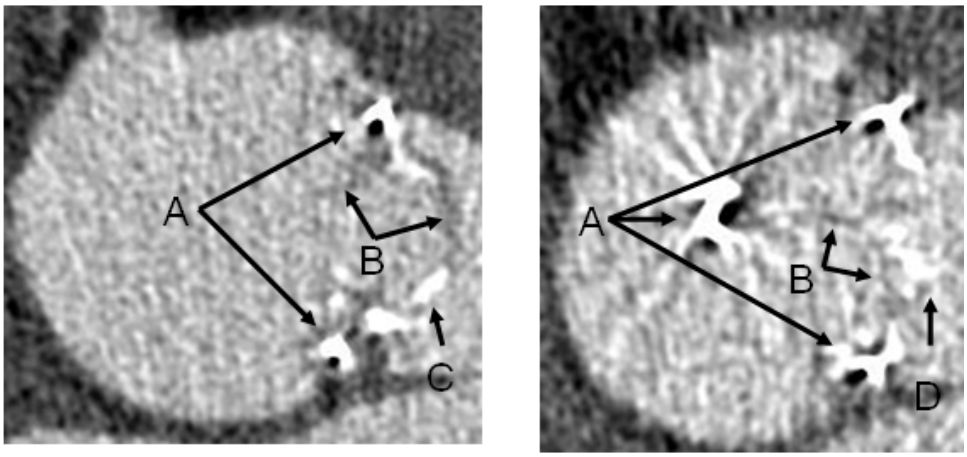

Fig. 3.1: Two MSCT slices of aortic valve prosthesis with high level noise, showing stent (A), leaflets (B), calcification (C) and pannus (D).

Because of their low density, leaflets (B) appear as dark structures in MSCT images. Due to their thin structure, they can be observed as regions of a few voxels of thickness in their non degenerated part. In addition images are altered by metal artifacts and noise that need to be reduced while keeping details of leaflets.

3.1 NOISE AND ARTIFACTS ANALYSIS

3.1.1 Noise and metal artifacts in MSCT images

The main source of noise in CT is quantum noise [3.1-3.3]. It results from statistical fluctuations in the number of X ray quanta. In MSCT images, noise is emerging from several sources: detector elements, signal transmission, reconstruction and processing methods, etc. Due to these complex dependencies, the noise distribution model is usually unknown.

Streak artifacts constitute a kind of directed noise, like metal artifacts, that results in general from an inconsistency in projection sample measurements. Such inconsistencies may arise from patient motion, data under-sampling or when only few quanta reach the detector [3.1-3.3]. This happens mainly when highly attenuating objects, like bones or metallic stents, are scanned (Fig 3.1).

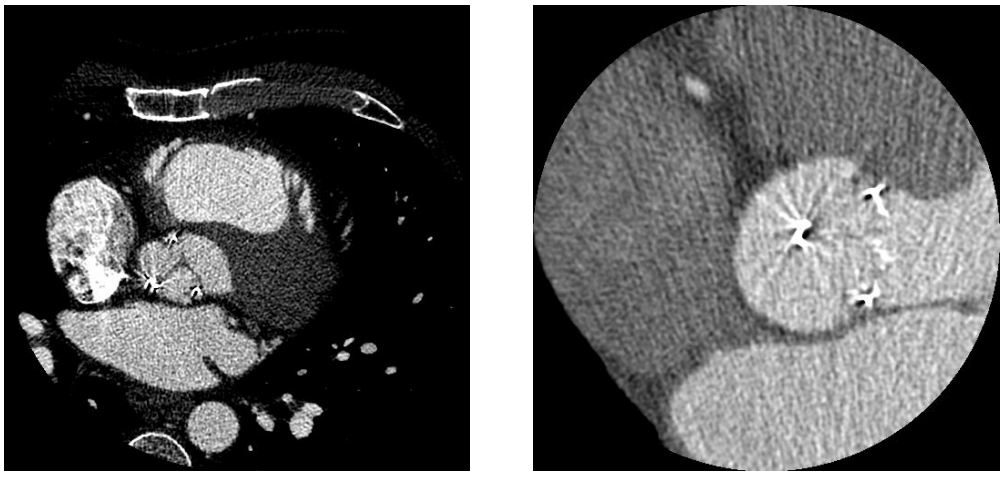

A B

Fig. 3.2: Noises in MSCT images of bioprosthesis. We can see noise and metal artifacts in both images. Image B shows strong directional noise.

Bioprosthesis can have complete or incomplete metallic stents. Because of the higher atomic number, the metal object attenuates X-rays in the diagnostic energy range much more than soft tissues and bone, and much fewer photons can reach detectors [3.4]. When metal is present, pronounced dark and bright streaks are produced in reconstruction with conventional filtered back projection. These artifacts seriously degrade image quality, particularly near the metal surfaces. Primary applications of metal artifact reduction include dental, orthopedic, oncologic imaging. Metal artifact reduction in MSCT images of aortic valve prosthesis is a new issue in cardiac CT imaging.

3.1.2 Motion–related Imaging Artifacts

Although cardiac CT imaging has a very high temporal resolution (between 80ms and 330ms), this is not enough to avoid the motion–related imaging artifacts of leaflets. MSCT demands a 65 bpm heart rate limitation (for the coronary arteries) [3.5]. The motion–related imaging artifacts may cause false segmentation of moving leaflets (both bioprosthesis and native), increasing the thickness value.

3.1.3 Spatial resolution

Currently, the spatial resolution of MSCT can reach values down to 0.3 mm per

pixel and 0.6 mm for z-axis [3.5]. Analyzing aortic valve bioprosthesis, the problem is represented by leaflets thickness. Depending from the type of bioprosthesis, pericardial or porcine, and from the manufacturer, leaflet thickness is submillimetric. In the process of filtered back projection (FBP), voxels, whose spaces include both leaflets and vascular lumen with radio contrast dye, may be affected by partial volume effect.

3.2 STATE OF THE ART: MSCT IMAGE PREPROCESSING

Maintaining information details while reducing noise and artifacts is essential in the processing of ECG-gated MSCT images. However, the noise and metal artifacts in MSCT images cannot be accurately modeled into one specific distribution [3.6, 3.7]. When considering thin structures it can be difficult to distinguish informative anatomical/pathological features from noise/artifact. In the following we present some pre-processing methods reported in the literature to reduce metal artifacts and noise.

3.2.1 Metal artifact reduction

Metal objects in the field of interest cause inconsistencies of the acquired data set. During the image reconstruction using the standard filtered back projection (FBP), these inconsistent values lead to metal artifacts that overlay the whole image as star shaped streaks. To enhance the image quality and to ensure a correct diagnosis, metal artifact reduction (MAR) techniques are required. In the last three decades, many MAR methods have been presented. One popular strategy is the substitution of metal influenced Radon values with surrogate values [3.4]. This technique first separates metal data from uninfluenced values in Radon space. A re-computation of the influenced data

is possible, e. g. using detector based interpolation [3.8], sinogram-gradient based interpolation [3.9, 3.10], wavelets [3.11] or an adapted inclusion of the metal influenced data [3.12]. However, even with high level interpolation residual inconsistencies may remain. Since the standard FBP is very susceptible also to residual inconsistencies, a more appropriate reconstruction method is required to reduce or rather avoid metal artifacts.

Projection-based method for reducing metal artifacts caused by hip prostheses in multi-slice helical CT was presented [3.13]. The proposed method is based on reformatted projection, which is formed by combining the projection data at the same view angle over the full longitudinal scan range. Detection and segmentation of the metal were performed on each reformatted projection image. Two dimensional interpolation based on Delaunay triangulation was used to fill voids left after removal of the metal in the reformatted projection. The corrected data were then reconstructed using a commercially available algorithm. The main advantage of this method is that both the detection of the metal objects and the interpolations are performed on complete reformatted projections with the entire metal region.

3.2.2 Noise reduction

In order to reduce the noise in CT images a preprocessing step is usually implemented. The goal of this preprocessing is to increase the signal to noise

ratio (SNR) as well as to increase the contrast of the structures of interest.

Classic smoothing filters, such as Median filter and Gaussian blur, may not give acceptable results. We present in the following some of the filtering approaches reported in the literature such as Hessian based filters and anisotropic diffusion filters that, in our opinion, could be interesting to reduce noise in MSCT images of thin structures.

3.2.2.1 Hessian based filters

This class of filters is also called “vessel enhancing filters”. They have strong abilities of keeping small vessel details while reducing noise in the image. Lorenz filter [3.14], Frangi filter [3.15] and Sato filter [3.16] were proposed for noise reduction and segmentation in medical images of vessels.

3D Hessian matrix is defined as follows:

$$H_\sigma = \sigma^2 \begin{pmatrix} \frac{\partial^2 u_\sigma}{\partial x^2} & \frac{\partial^2 u_\sigma}{\partial x \partial y} & \frac{\partial^2 u_\sigma}{\partial x \partial z} \\ \frac{\partial^2 u_\sigma}{\partial x \partial y} & \frac{\partial^2 u_\sigma}{\partial y^2} & \frac{\partial^2 u_\sigma}{\partial y \partial z} \\ \frac{\partial^2 u_\sigma}{\partial x \partial z} & \frac{\partial^2 u_\sigma}{\partial y \partial z} & \frac{\partial^2 u_\sigma}{\partial z^2} \end{pmatrix}$$

Where $u_\sigma = I * G_\sigma$ is the convolution between the original image and a Gaussian function.

$\lambda_1, \lambda_2, \lambda_3$ are the 3 matrix eigenvalues (they are defined as $|\lambda_1| < |\lambda_2| < |\lambda_3|$). The eigenvector associated with the smallest eigenvalue points out the direction with the smallest curvature of Hessian matrix (direction of vessel). Other 2 eigenvectors define a plane orthogonal to the vessel direction.

When considering voxels within an ideal tubular structure, the eigenvalues behave typically as follows:

$\lambda_1 \approx 0$, $|\lambda_1| << |\lambda_2|$, and $\lambda_2 \lambda_3 > 0$

Thus, the relations between the eigenvalues are summarized in table 3.1.

Tab. 3.1: Possible patterns in 2D and 3D, depending on the value of the eigenvalues (H=high, L=low, N=noisy, usually small). The eigenvalues are ordered as: $|\lambda_1| < |\lambda_2| < |\lambda_3|$ [3.15].

$2D$		$3D$			orientation pattern
λ_1	λ_2	λ_1	λ_2	λ_3	
N	N	N	N	N	noisy, no preferred direction
		L	L	H-	plate-like structure (bright)
		L	L	H+	plate-like structure (dark)
L	H-	L	H-	H-	tubular structure (bright)
L	H+	L	H+	H+	tubular structure (dark)
H-	H-	H-	H-	H-	blob-like structure (bright)
H+	H+	H+	H+	H+	blob-like structure (dark)

The vesselness function is defined as:

$v_0(s) = 0$ if $\lambda_2 > 0$ or $\lambda_3 > 0$ (the tubular is a dark structure)

$$v_0(s) = (1 - \exp(-\frac{R_A^2}{2\alpha^2}) \exp(-\frac{R_B^2}{2\beta^2})(1 - \exp(-\frac{s^2}{2c^2})) \quad (3.1)$$

Where:

$$R_A = \frac{|\lambda_2|}{|\lambda_3|} \quad \text{and} \quad R_B = \frac{|\lambda_1|}{|\lambda_2\lambda_3|}$$

are used to classify tubular structure and streak artifacts.

$S = \sqrt{\lambda_1^2 + \lambda_2^2 + \lambda_3^2}$ is used to classify vessel and non-stationary streak.

Because of the different size of arteries in images, the vesselness function is modified as:

$$v = \max_{\alpha_{\min} \le \alpha \le \alpha_{\max}} v_0(s, \alpha)$$

Where $\alpha_{\min}$ and $\alpha_{\max}$ are the minimum and maximum radius of arteries in original CT set.

Hessian based filters show a good adaptability to tubular structures such as vessels. But in the case of aortic valve prosthesis, some components, like leaflets, cannot be featured by cylindrical patterns.

3.2.2.2 Partial differential equations (PDE) based filters

The anisotropic diffusion filters are non-linear filters based on partial differential equations. They have been proposed for noise reduction and segmentation in different types of cardiac images, especially in high level noise CT images and ultrasound images.

The main idea of anisotropic diffusion filters is that image features, such as

discrete gradient, modified curvature or local variance, can be used to derive different intensities of diffusion in different directions.

Perona-Malik (PM) Model [3.17] was the first introduced anisotropic diffusion filter in 1990. All of other anisotropic diffusion filters were developed from this filter. In PM Model, the values of resulting voxels I_p^{t+1} are calculated as:

$$I_p^{t+1} = I_p^t + \frac{\lambda}{|\eta_p|}\sum_{q\in\eta_p} c(\nabla I_{p,q}^t)\nabla I_{p,q}^t \quad , \qquad (3.2)$$

where η_p is the neighborhood of the current voxel and $|\eta_p|$ is the number of voxels in η_p . I_p^t is the current value of the voxel. $\nabla I_{p,q}^t$ is the discrete gradient along the q[th] direction (defined by the current voxel and neighboring voxels). *c(x)* is the function used to control the rate of diffusion along different directions. It can take different expressions such as:

$$c(x) = \frac{1}{1+(x/k)^2} \quad \text{or} \quad c(x) = \exp(-(x/k)^2) ,$$

K is a parameter to control the diffusion intensity in directions. It is determined by the intensity of noise. If the voxels are inside different objects, $\nabla I_{p,q}^t >> k$, $c(\nabla I_{p,q}^t) \to 0$, the processing of diffusion is stopped. If the voxels are inside different objects, $\nabla I_{p,q}^t \le k$, the diffusion is increased. The higher is k (use of a more strength diffusion), the more smoothed are the images after an iteration.

λ is an additional parameter to control overall diffusion intensity. It is determined by the level of noise. A quick diffusion ($\lambda = 1$) is set when the noise is low and a slaw diffusion is applied when the noise level is high.

Classical Anisotropic diffusion operators as PM model can enhance edge while

denoising the image. The main drawback with PM model is the determination of the parameter k in the case of images with high level of noise. Thus, when the value of k is high to denoise the image, $c(\nabla I_{p,q}^t)$ and $\nabla I_{p,q}^t$ may give both high outputs for the noise voxels. After some iterations, some sharp impulse noises may appear. These impulse noises can not be smoothed by PM model itself.

Catté_PM model [3.18] was presented in 1992. It uses a Gaussian convolution Function to improve the performance of PM model in case of strong Gaussian noise:

$$I_p^{t+1} = I_p^t + \lambda \sum_{q \in \eta_p} (\alpha_p^t + \alpha_q^t) \nabla I_{p,q}^t \tag{3.3}$$

where：

$\alpha_p^t = c(|\nabla (G_\sigma * I)|)$, $G_\sigma(x) = (2\pi\sigma)^{-0.5} \exp(-x^2 / 4\sigma)$ is the Gaussian function with variance σ. "*" is convolution.

In addition to the strong assumption on noise distribution, which introduces a new parameter σ, the difficulty of determining the parameter k is not solved in Catté_PM model.

Fourth-order partial differential equation (F_PED) [3.19] was presented in 2000. It introduced fourth-order partial differential equation in the diffusion equation. This filter can reduce staircase but it may produce strong impulse noise (salt and pepper noise) during filtering.

To deal with impulse noise appearing during diffusion, Anisotropic Median

Diffusion (AMD) model [3.20] introduced a median filtering after diffusion iteration:

$$I_p^{t+1} = \underset{q \in W}{Median}(I_p^{t+1}, I_q^{t+1}) \tag{3.4}$$

W is the neighborhood used in additional Median filter.

Tukey's Biweight function (also known as bisquare function) [3.21] was introduced to perform a piecewise-smoothing:

$\rho(x,\sigma) = \frac{x^2}{\sigma^2} - \frac{x^4}{\sigma^4} + \frac{x^6}{3\sigma^6}$ when $|x| < \sigma$ and $\rho(x,\sigma) = \frac{1}{3}$ in other cases. Fig 3.3 shows its curve.

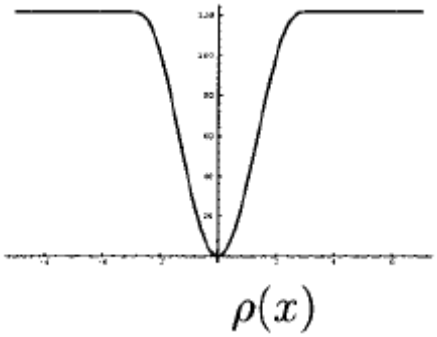

Fig 3.3: Curve of Tukey's Biweight function.

Because its good performance in terms of robustness and edge keeping, AMD model combined this function with the classifier c(x) used to distinguish edge and noise:

$$\begin{aligned} &c(x) = 1 \quad \text{when} \quad |\nabla I| \le k \\ &c(x) = \frac{25}{16k}\left(1 - \left(\frac{\nabla I}{\sqrt{5}k}\right)^2\right)^2 \quad \text{when} \quad k < |\nabla I| \le \sqrt{5}k \\ &c(x) = 0 \quad \text{when.} \quad |\nabla I| > \sqrt{5}k \end{aligned} \tag{3.5}$$

When the gradient is smaller than k, the neighboring voxel is considered to has

a large probability to be inside the same object as the current voxel, the diffusion is not limited; When the gradient is between k and $\sqrt{5}k$, the probability is less and the diffusion is limited; when the gradient is bigger than $\sqrt{5}k$, it is considered that the neighboring voxel belongs to an other object and the diffusion is stopped.

[3.21] also presented a method to determine parameter k using median absolute deviation (MAD):

$$k = \frac{1}{0.6745} median(|\nabla I_i| - median(\nabla I_i))|_{I \in ROI} \quad (3.6)$$

which is the MAD of the discrete gradient in the region of interest.

Kernel anisotropic diffusion (KAD) [3.22] was presented to preprocess images with high level of noise. It incorporates a kernelized gradient operator in the diffusion, leading to more effective edge detection and providing a better control of the diffusion process. The main drawback of this approach is the size of the kernel. The large size of the kernel required to reduce noise is not well adapted to the processing of thin structures.

Anisotropic Curvature Diffusion, which is based on a modified curvature diffusion equation (MCDE) [3.23-3.25], has been introduced to overcome impulse noise enhancement in anisotropic diffusion filter. In anisotropic curvature diffusion, the discrete gradient $\nabla I_{p,q}^t$ used in PM Model was replaced by a curvature function:

$$I_p^{t+1} = I_p^t - \frac{\lambda}{N} \sum_{q \in \eta_p} c(Curv(L_{p,q}^t)) Curv(L_{p,q}^t) \quad (3.7)$$

where $L^t_{p,q}$ is the line defined by the current voxel and a direction given by a voxel of the neighborhood η_p. $Curv(L^t_{p,q})$ is the discrete curvature at the voxel along this line.

Vessel enhancing diffusions (VED) [3.26] use the diffusion direction based on vessel function defined by Frangi filter (introduced in section 3.3.2.1). The partial differential equation of VED can be espressed as:

$$I_p^{t+1} - I_p^t = div(D \times \nabla I_p^t) \tag{3.8}$$

Where:

$$D = Q\lambda' Q^T$$

Q is Eigenvector matrix of Hessian matrix.

Min-Max curvature flow [3.27, 3.28] was presented as a class of PDE-based algorithms suitable for image denoising and enhancement in 1995.

These techniques are applicable to both impulse noise and full-image continuous noise. It applies a variant of the curvature flow algorithm on 2D images where diffusion is turned on or off depending of the scale of the noise that one wants to remove.

The value of voxels after filtering is defined as follow:

$$I_t = F(\kappa)|\nabla I| \tag{3.9}$$

$$\kappa = div\left(\frac{\nabla I}{|\nabla I|}\right)$$

Max min flow is defined as:

$$F(\kappa) = \begin{cases} \max(\kappa, 0) & \text{if } a(x,y) < G(x,y) \\ \min(\kappa, 0) & \text{otherwise,} \end{cases}$$

where a(x, y) is the average value of image intensity I(x, y) in a small neighborhood around the pixel (x, y), and G(x, y) is defined as the average intensity evaluated in the direction perpendicular to the gradient direction.

And Min Max curvature flow is defined as:

$$F(\kappa) = \begin{cases} \kappa & \text{if } |\nabla I| < T \\ \min/\max \text{ flow} & \text{otherwise,} \end{cases} \tag{3.10}$$

where T is some threshold value set on the local gradient magnitude to enhance selected regions. Pixels at which the gradient magnitude is greater than T are preferred and are diffused using the min/max flow. The remaining points are diffused using the plain curvature flow.

Anisotropic diffusion filters may be suitable for reducing noise in MSCT data of bioprosthesis thanks to their ability of keeping the details of structures along different directions.

The main drawback of these filters is their limited performance in case of high level noise. Although modified models introduced different features and improved diffusion equations, this limitation still exists and has to be considered, especially in the case of cardiac MSCT images.

3.2.2.3 Noise reduction in LDCT images

Reducing dose during CT imaging is new challenge. In recent years, some specific techniques have been proposed for improving the quality of Low Dose

CT (LDCT) images which include very high level quantum noise.

For instance, a hybrid approach, making use of low-pass and directional filters from previously segmented regions (both non-structured and structured), has been described [3.29].

In 2010, a filter named SharpView CT applies a multi-frequency analysis to divide the image into several subbands and separately process them before re-combination [3.30].

In 2011, a weighted intensity averaging over large-scale neighborhoods (WIA-LN) was proposed for processing abdominal LDCT images, which can be deemed as a large-scale nonlocal means (LNLM) [3.31].

The weighted large-scale averaging in the LNLM method relies on the information redundancy property within a local neighborhood to suppress mottled noise without obvious loss of image details. Nevertheless, the LNLM method is not effective in suppressing the non-stationary streak artifacts in thoracic CT images [3.31].

A qualitative and quantitative study performed on a thoracic phantom and a comparison with the HDCS filter [3.32] was reported. Results obtained on real data with an expert-based evaluation, show that the proposed method achieved effective noise/artifact reduction in thoracic LDCT images with little compromise in contrast.

3.3 ROI DEFINITION

In order to deal with the difficulties mentioned in previous sections of pre-processing and segmentation of the CT images of the bioprosthesis, we considered a region of interest (ROI). While this region should include all the structures of the bioprosthesis, it also should be as small as possible. In this region which has to fit to the bioprosthesis, decreasing the number of voxels may make denoising and segmentation much easier, and the amount of metal artifacts and false segmentations will be decreased.

We considered two kinds of shape for the ROI: a cylindrical shape preferentially for incomplete metallic stents and a conformational shape for complete metallic stents (Fig. 3.4). These two kinds of ROI are both defined by the metal part of the bioprosthesis stent.(Fig. 3.5).

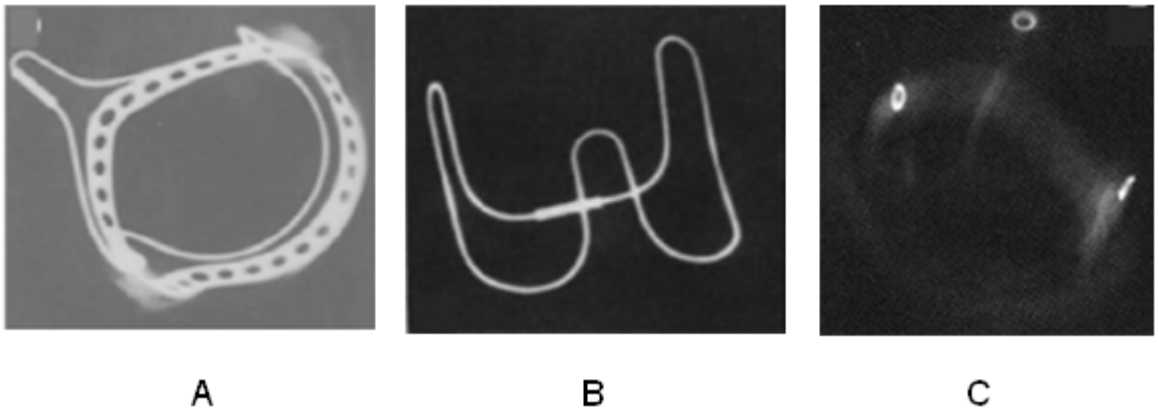

Fig. 3.4: Radiological images of bioprostheses with complete metallic stent (A and B) and incomplete metallic stent (C).

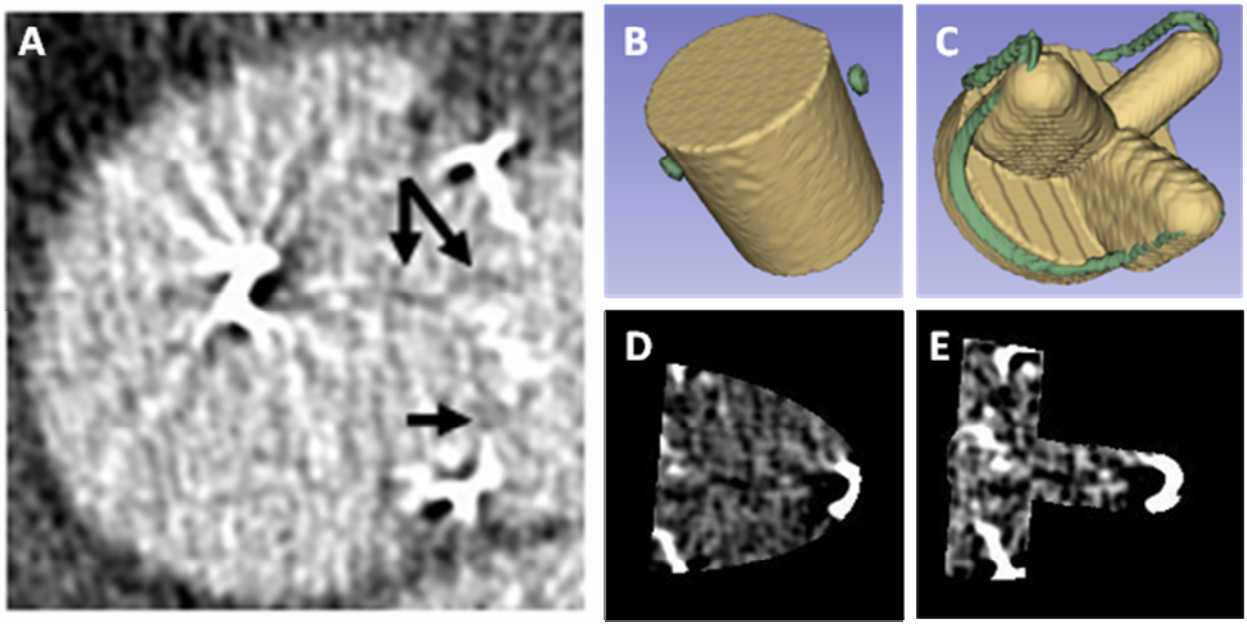

Fig. 3.5: Regions of interest: a slice in a classical cubic ROI (A), Cylindrical (B) and conformational (C) stent defined ROI, and illustration of the corresponding CT observations (D and E respectively) within one of the original CT slices.

In classical cubic ROI metal artifacts and noise textures in vascular lumen are difficult to distinguish from the leaflets (pointed by black arrows). In stent defined ROI the number of voxels is decreased. Metal artifacts outside the bioprosthesis structure are excluded by the ROI. During segmentations based on region growing, ROI can also limit the growing process in the volume image. The parameters of the cylindrical ROI include the top surface position (the center of a cylindrical area), direction of the cylinder axis, radius and height of the cylinder. They are determined from the segmentation of the stent from preoperative (in-vivo) CT images. At this step, a coarse segmentation based on a simple operation of thresholding is performed.

The center of the top surface is obtained from the center of the 3 metal points

of the incomplete metallic stent, and the cylinder radius is taken as the maximum distance between the metal points and the center.

The direction of the plane defined by the 3 metal points of the stent is used to determine the direction of the cylinder axis. The height of the cylinder is determined assuming a prior knowledge on the bioprosthesis features. In order to completely include the leaflets, which are moving structures, a margin on the cylinder height was considered.

The *conformational* ROI is also estimated by considering a prior knowledge about the bioprosthesis. We assume that the type and the main geometrical features of the bioprosthesis placed in the patient are known. A simple geometrical model of the different structures is used to construct a volumetric model of the bioprosthesis. This model determines the conformational ROI. In this ROI the volume of the leaflets is expanded with spatial margins in order to take into account their different spatial configurations resulting from their motion in in-vivo conditions.

The stent is used to fit the conformational ROI model to the bioprosthesis observed in the CT images. The metal part of the stent, which is characterized by high gray levels, is coarsely segmented thanks to a simple image thresholding operation. The parameters of the ROI, such as its size, position, direction and rotation can then be determined from the segmented stent.

A 3D Hough transform [3.33] is used to identify the bottom circle of the metallic stent (Fig.3.6), and thus to determine the position, radius, height and direction

of the stent and ROI. The rotation is determined by detecting the missing parts of the circle.

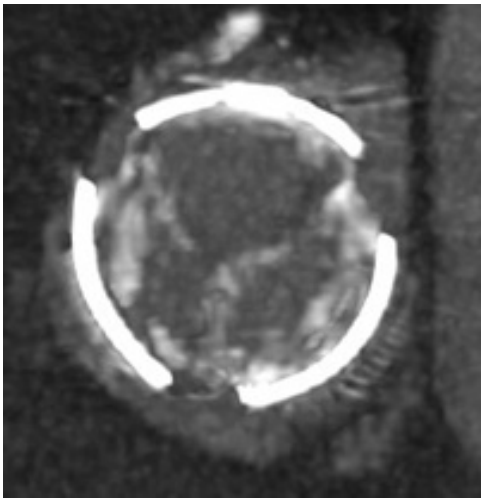

Fig 3.6: Circle of the metallic stent used to determine the features of the conformational ROI.

3.4 DENOISING

As already mentioned, the level of noise in the considered MSCT images is high. The aim of the preprocessing step is to enhance the image, in other words to reduce the noise while keeping as much as possible the information on the structures of interest. To quantitatively assess this level of noise, we considered the signal-noise ratio (SNR). It is also used as a performance criterion to compare the image resulting from different image processing algorithms.

SNR shows the ratio between energy of signal and noise. Nevertheless, “energy” is difficult to define in the case of images. We used the definition given in [3.34]:

$$SNR = 10 * \log_{10}\left(\frac{Max(Var_i)}{Min(Var_i)}\right)\Big|_{i \in ROI} \quad , \qquad (3.11)$$

where Var_i is the local variance in the structures of interest. In this definition the maximum variance is assumed to be caused by the presence of an edge (energy of the signal) whereas minimum variance is caused by noise (energy of noise).

Due to their size and density, the critical components are the leaflets. Structures with high density, such as stent and calcifications, would drive to artificially high SNR values and could be un-relevant regarding valve leaflets. Thus, voxels

representing stent, calcification and pannus are not considered in the computation of SNR. Voxels located at the boundary between leaflets and vascular lumen are used to obtain the maximum variance whereas voxels located in the vascular lumen are used to obtain minimum variance.

Fig. 3.7 shows examples of MSCT images of bioprosthesis in four different cases: HER, MAG, BOU and DAV.

Compared with common MSCT images of the native valve, these images include a high level of noise. SNR varies from 6 to 8 in the case of bioprothesis whereas it is about 15 in the case of the native valve.

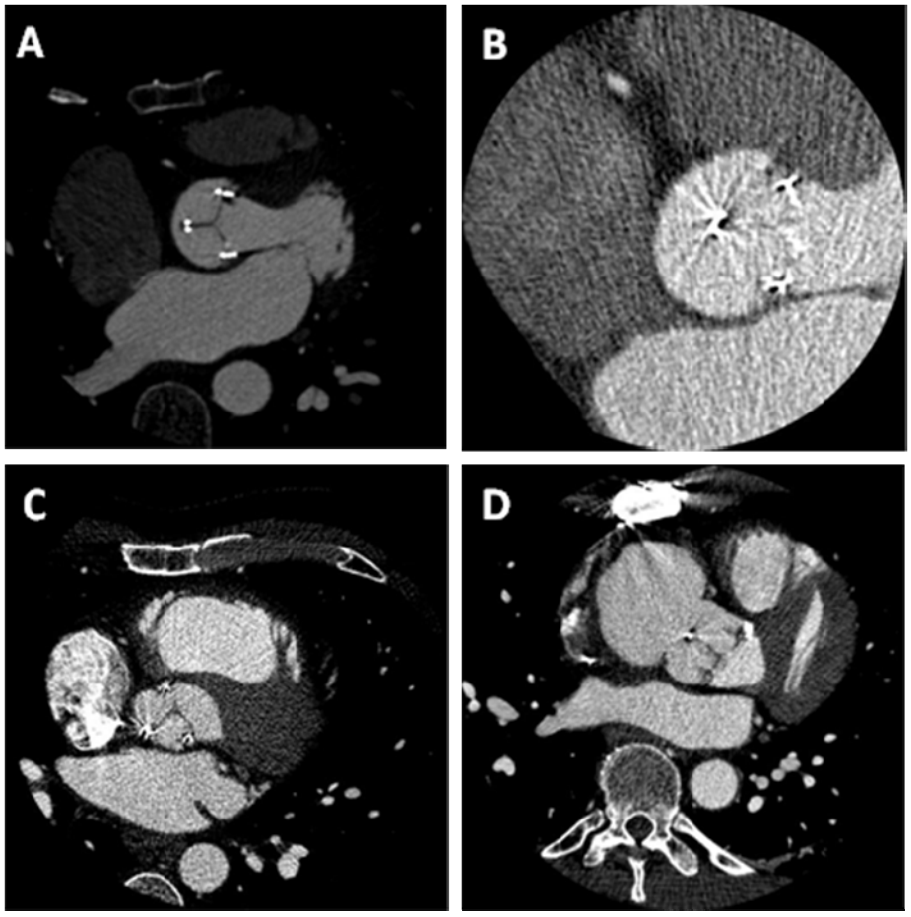

Fig 3.7: Slices form MSCT data sets: HER (A), MAG(B), BOU(C) and DAV(D).

In order to reduce noise and metal artifacts while retaining the details of thin structures like leaflets we focused on two kinds of filters thanks to their ability of directional analysis.

In Section 3.4.1, we describe how anisotropic diffusion filter can be applied and adapted to noise reduction in bioprosthesis images. Modified classifier based on Tukey's Biweight, median absolute deviation (MAD) and median filtering processes, as well as the determination of their parameters are more precisely peresented..

In Section 3.4.2, we propose a new approach based on stick filters which was initially introduced to process ultrasound images. Features along sticks are used to classify voxels within different structures and different noise reducing processes are designed. Following the approach introduced by Frangi with the vesselness measure in the case of tubular structures, we introduce the notion leafletness measure in the stick filter.

3.4.1 Anisotropic Diffusion Filters

Thanks to the ability of anisotropic diffusion filters to analyze densities in different directions, they have good performance particularly in the case of vascular images. High level of noise is a limitation of anisotropic diffusion filters. To improve their performance, robustness and impulse noise reduction, we used a modified diffusion equation including Tukey's biweight formulation,

median absolute deviation (MAD) and median filtering, originally introduced in Anisotropic Median Diffusion (AMD) approach with PM model (section 3.3.2.2)

In most cases, the values of resulting voxels I_p^{t+1} in anisotropic diffusion filters can be written as:

$$I_p^{t+1} = I_p^t + \frac{\lambda}{|\eta_p|}\sum_{q\in\eta_p} c(F(I_{p,q}^t))F(I_{p,q}^t) \tag{3.12}$$

where $F(I_{p,q}^t)$ is the function chosen to chraracterize voxels values. It can be discrete gradient (PM model), Gaussian convoluted discrete gradient (Catté_PM model) or modified curvature (ACD). η_p is the neighborhood of the current voxel and $|\eta_p|$ is the number of voxels in η_p. We tipically considered a 3*3*3 cubic neighborhood. Larger η_p may smooth edge too much, especially in image including high level noise.

c(x) is the classifier used to distinguish edge and noise. In all anisotropic diffusion filters we used the modified classifier introduced in AMD:

$c(x) = 1$ when $F(I_{p,q}^t) \le k$

$c(x) = \frac{25}{16k}(1-(\frac{\nabla I}{\sqrt{5}k})^2)^2$ when $k < F(I_{p,q}^t) \le \sqrt{5}k$ (3.13)

$c(x) = 0$ when. $F(I_{p,q}^t) > \sqrt{5}k$

where k is a parameter used to control the diffusion intensity in directions. It can be determined by the median absolute deviation:

$$k = \frac{1}{0.6745} median(F(I_i) - median(F(I_i)))|_{I_i\in ROI} \tag{3.14}$$

where $F(I_i)$ denotes the features of all the voxels located in the ROI. Although edge voxels have features with higher values, they are much less

than vascular lumen and leaflets voxels (about 5% or less). The inclusion of edge voxels in this calculating process should not affect MAD results. After each iteration, k should be refreshed. The number of iteration can be a critical parameter.

λ is another parameter to control diffusion intensity. Value of λ can be determined according to SNR. It was set at 1 (fast diffusion) for a low level of noise. In the case of images showing a high level of noise, λ was set at 0.5 (low diffusion).

In case of low SNR impulse noise may be amplified by the filtering process. All of anisotropic diffusion filter might have this drawback.

In order to reduce impulse noise (Fig. 3.8) generated by the filtering process (normally after 6 or 8 iterations), we introduced a median filter in the process:

$$I_p^{t+1} = \underset{q \in W}{Median}(I_p^{t+1}, I_q^{t+1}) \tag{3.15}$$

where p indicates the noise voxel and q the neighboring voxel located in neighborhood W.

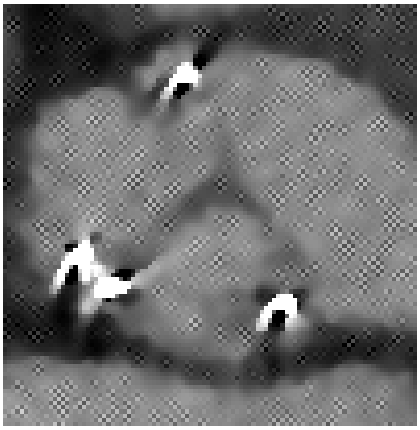

Fig. 3.8: impulse noises amplified during diffusion filtering.

Equations 3.11-3.15 introduced modified classifier, median absolute deviation and median filtering into anisotropic diffusion filter in our experiments we used different models: PM, catté_PM, ACD models and min-max curvature flow.

3.4.2 Stick Filter

Original Stick filter is a non-linear filter which was presented as a boundary and line detector in 1998 [3.35]. The main idea of this filter is to divide the cubic neighborhood of the considered voxel into a set of sticks, and to use local features (variance, maximum difference between voxels, curvature) to combine intensities along the different directions of the sticks.

3.4.2.1 Original stick filter

Stick filter was first introduced to reduce strips-like noise in ultrasound images [3.36]. The neighborhood of the current voxel is divided into a set of sticks (Fig. 3.9) to perform a non-linear filtering of the image. The output I' at the current voxel is defined as:

$$I' = \frac{1}{W}\sum_{i=1}^{N} g_i \overline{I_i} \quad \text{and} \quad W = \sum_{i=1}^{N} g_i \tag{3.16}$$

where $\overline{I_i}$ denotes the local mean value along the i^{th} stick, N is the number of sticks, $g_i = \frac{L}{\sum_{j=1}^{L}(I_{i,j} - \overline{I_i})^2}$ is the reciprocal of local variance along the i^{th} stick and L is the length of stick, used to classify edge and noise.

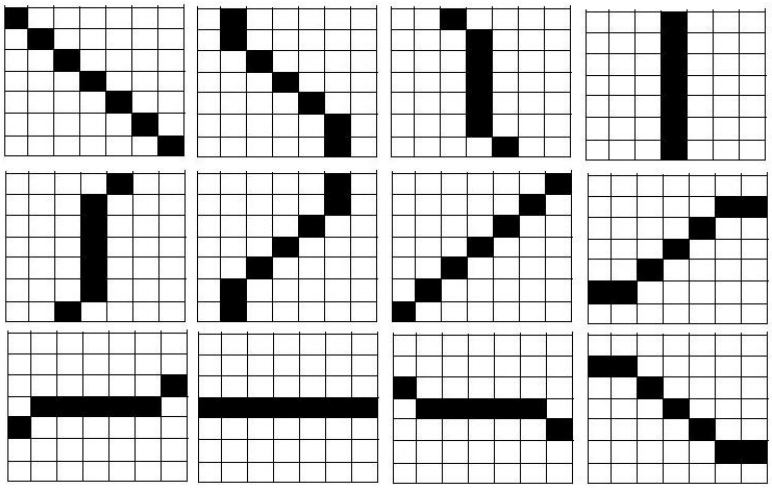

Fig. 3.9: 7 voxels-length 2D symmetric sticks set.

Stick filtering approach has also been used with a neighborhood divided into a set of asymmetric sticks (Fig. 3.10). Because of this asymmetric configuration, the filter could get better performance in terms of keeping details of thin structure while denoising the image.

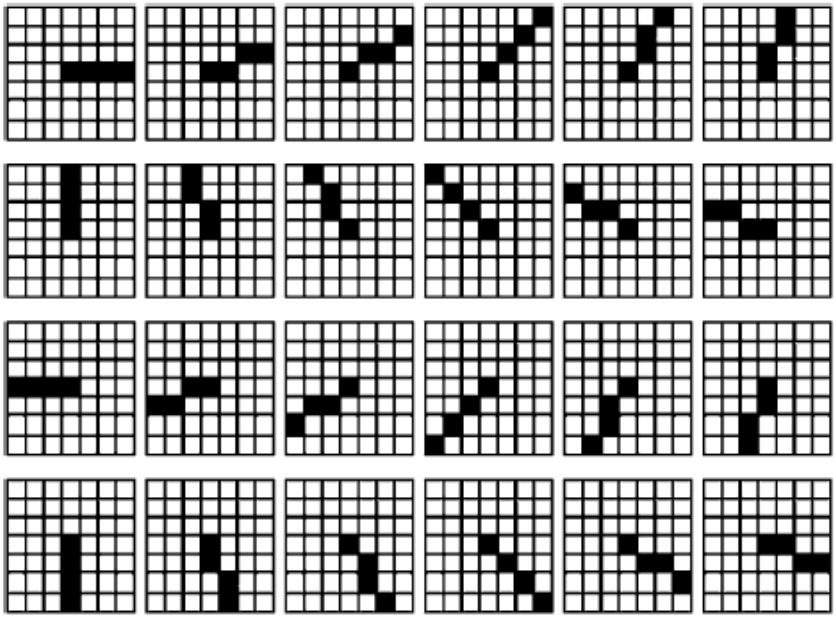

Fig. 3.10: 4 voxels-length 2D asymmetric sticks set

3.4.2.2 Stick based pre-processing

Local analysis of gray level changing along sticks could be helpful to classify the current voxels into different structures, such as leaflets, vascular lumen, noise and metal artifact. According to the measure designed to characterize the distribution of voxel values along the sticks, especially in the area of leaflets, different combinations of image values could be implemented to reduce noise and artifact and to enhance relevant information.

Classification of structures

We divided the cubic neighborhood of each voxel in the ROI into a set of asymmetric sticks. The length of stick L should be longer than half of the thickness of leaflets observed in MSCT data, to make sure that for voxels inside leaflets, there is at least one stick crossing the edge between vascular lumen and leaflets.

Different gray level features are first measured along different configurations of sticks subsets according to prior knowledge about the morphological properties of the structures we want to classify.

In sticks set, the stick orthogonal to edge should have the shortest length inside leaflets. For the i^{th} stick we calculate the maximum MG_i of the magnitude of local differences of gray levels between the current voxel and j^{th} voxel along the stick:

$$MG_i = \max_{j=1}^{L}\left(\frac{|I_{i,j} - I_{i,1}|}{dis_{i,j}}\right) \tag{3.17}$$

where $dis_{i,j} = \sqrt{(x_{i,j} - x_{i,1})^2 + (y_{i,j} - y_{i,1})^2 + (z_{i,j} - z_{i,1})^2}$

We define S_M as the stick with the maximum *MG* value and S_m as the stick with the minimum *MG* value.

If there is no high variation of gray levels in the set of sticks, *i.e.* when MG_i is less than a threshold T_{MG}, we assume that the voxel belongs to the vascular lumen. If all of the sticks in the considered set show high variation of gray levels, *i.e*. when MG_i is higher than the threshold T_{MG}, we assume that we are in the case of an impulse noise voxel.

For the sticks with high *MG* values (sticks crossing edge), we select the stick S_M with the maximum *MG*. We assume the direction of this stick S_M is orthogonal to an edge. The current voxel and the direction given by S_M define a plane in which we consider a set of coplanar sticks S_{MC}. When the coplanar sticks S_{MC} have low *MG* values, *i.e. MG* values are less than the threshold T_{MG}, we assume that the current voxel is close to the edge of a thin structure like a leaflet. It can be located either inside this thin structure, *i.e.* inside the leaflet, or outside the thin structure, *i.e.* inside the vascular lumen. (Fig. 3.11 A)

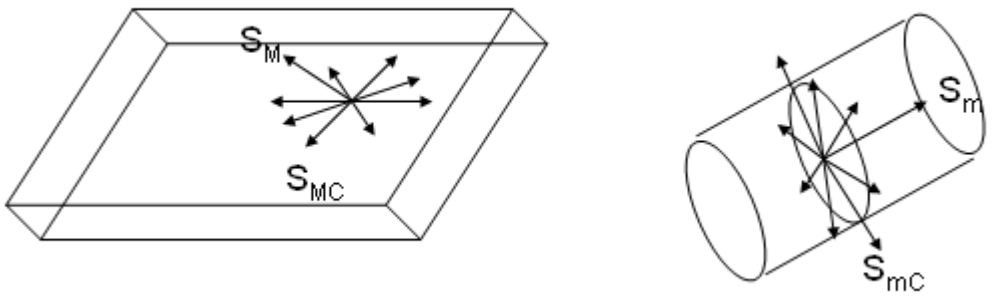

A B

Fig. 3.11: Sticks perform in thin structure (S_M /S_{MC})(A) and in tubular structure (S_m / S_{mC})(B).

Moreover small vessels or artifacts are characterized by tubular or elongated shapes. The sticks lying in this kind of structures should have low *MG* values. We consider in this case S_m, the stick with the minimum *MG* value defined previously. The current voxel and the direction given by S_m define a plane in which we consider a set of coplanar sticks S_{mC}. We assume that the current voxel belongs to a small vessel or an artifact when S_m has low *MG* value, *i.e. MG* is less than the threshold T_{MG}, while the coplanar sticks S_{mC} have high *MG* values, *i.e. MG* values are higher than the threshold T_{MG}.(Fig. 3.11 B)

The classification process can be summarized by the flowchart reported in Fig. 3.12.

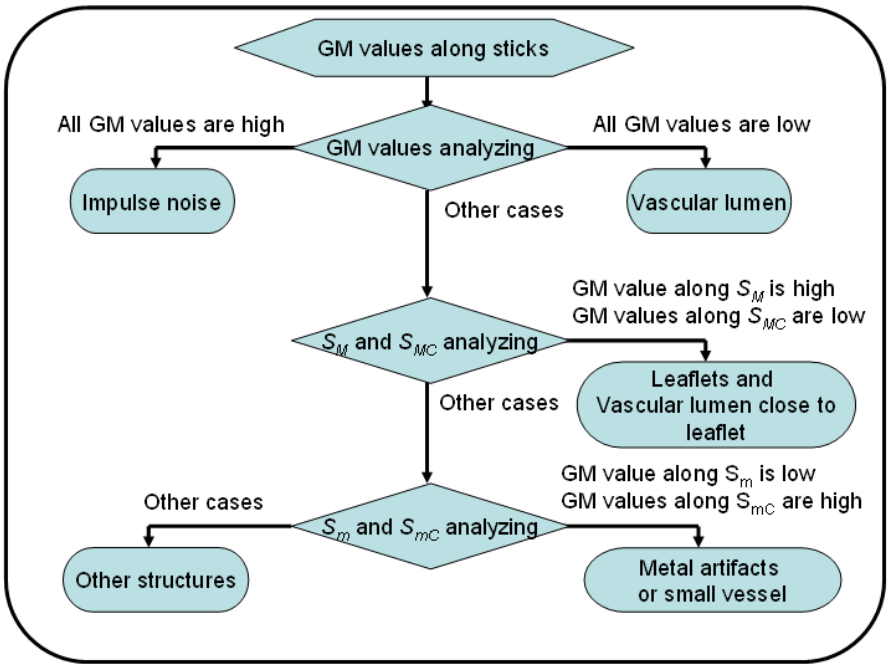

Fig. 3.12: the flowchart of classification of different structures in images.

Table 4.2 summarizes the heuristics used to design the classifier according to the features measured along the sticks: local mean along S_m, *MG* values along S_M and S_{MC}, *MG* values along S_m and S_{mC}.

Tab. 3.2: Possible structures depending on *MG* values along S_M, S_{MC}, S_m and S_{mC} sticks (H=high, L=low).

Possible structures	**Value of voxel**	***MG* values along:**			
		S_M	S_{MC}	S_m	S_{mC}
Vascular lumen	H	L	L	L	L
Leaflets	L	H	L		
Impulse noise		H	H	H	H
Small vessel or Artifacts		H		L	H
Others					

The “high” and “low” values of *MG* are fixed by the threshold T_{MG}. We propose to determine this threshold T_{MG} adaptively from the level of noise in the images. For the determination of T_{MG} we considered a cylindrical ROI. We estimate T_{MG} by calculating the median of *MG* values of all the sticks for all the voxels inside the cylindrical ROI:

$$T_{MG} = median(MG_i) \mid i \in ROIc \tag{3.18}$$

Noise reduction

According to the classification of the structures described previously, different noise reduction processes have been implemented. We describe them for the different cases:

- Vascular lumen

The values of resulting voxels *I'* are obtained from the following Stick filter, which is a modified version of the original stick filter:

$$I' = \frac{1}{W}\sum_{i=1}^{N} g_i I_{Medi} \quad \text{and} \quad W = \sum_{i=1}^{N} g_i \tag{3.19}$$

where $I_{Medi} = \underset{j=1}{\overset{L}{median}}(I_{i,j})$ is the median value along the i^{th} stick. To reduce the staircasing due stick filtering, the weighting function g_i is given by the Tukey’s biweight function:

$g_i = 1$ when $\mathrm{var}_i \le k$

$g_i = \frac{625}{256k}(1-\frac{\text{var}_i}{5k})$ when $k < \text{var}_i \le 5k$ (3.20)

$g_i = 0$ when. $\text{var}_i > 5k$

$\text{var}_i = \frac{1}{L}\sum_{j=1}^{L}(I_{i,j} - \bar{I}_i)^2$ with $I_{i,j}$, the value of the j^{th} voxel along the i^{th} stick.

The Mediane Absolute Deviation of local variances along all sticks inside the ROI is used to automatically determine k:

$k = \frac{1}{0.894} median(\text{var}_i - median(\text{var}_i))|_{I \in ROI}$ is given by absolute median diviation.

The filtering process is applied to the ROI. When part of stick is outside the ROI, we use original image voxels to complete it.

- Leaflets and vascular lumen close to leaflets

The stick filtering defined in equation 3.19 is applied here only on the set of S_{MC} coplonar sticks (sticks inside leaflet or vascular lumen). The stick filtering operation is then given by:

$I' = \frac{1}{W}\sum_{i=1}^{N} g_i I_{Medi}$ and $W = \sum_{i=1}^{N} g_i$ (3.21)

where I_{Medi} is the median value along the i^{th} stick, N' is the number of S_{MC} sticks $N' = (2L-1)^2$), and gi is defined as previously.

- Impulse noise

To remove impulse noise, we use a median filter with a minimum size neighborhood (of size 3*3*3).

- Metal artifacts

We use a weighted-mean filter to reduce the metal artifacts. In Equation 4.5, we considered $g_i = 1$ for all the sticks. In this case, the stick filter became a weighted-mean filter with a cubic neighborhood η (width of 2L-1):

$$I' = \frac{\sum_{i=1}^{|\eta|} n_i I_i}{\sum_{i=1}^{|\eta|} n_i} \qquad (3.22)$$

n_i is the weight of the neighboring voxels. For a given voxel in the neighborhood, its resulting weight depends on the number of sticks including it. We tipically used 5-voxels length sticks.

This filter could also be used to enhance small vessels, like coronary vessels, but it is not the concern here.

- Other structures

For the structures not specifically identified in the classification process, and labelled as "others" we apply the filtering process expressed by Equation 3.19, which also used in the case of vascular lumen. Calcifications which are high density structures are considered, among others, in the class "other structures".

To summarize we designed a filtering process to reduce noise while keeping details of thin structures like leaflets. It is mainly based on modified stick filtering. The neighboring of the current voxel is devided in a set of assymetric sticks

along which the distribution of gray levels is used to classify this voxel among one of five categories (vascular lumen, leaflets, impulse noise, metal artifacts, other structures). This process can reduce high level noise while keeping most of details of leaflets. Thanks to the adequation between stick partitioning in 3D space and distribution of gray levels due to metal artifacts, this filtering process is well adapted to the reduction of these artifacts, with no need of interpolation in the Radon space.

3.5 RESULTS

In this section we report and discuss our results of preprocessing. We firstly present the data and the failure mechanism for each studied case.

3.5.1 Degeneration assessment at reoperation

After reoperation explanted bioprostheses were analyzed by the surgeon in order to assess the real failure mechanism. Tab. 3.3 summarizes echocardiographic characteristics and failure mechanisms for studied bioprostheses.

Tab.3.3: Echocardiographic assessment and intra-operative evaluation of failure in studied bioprostheses.

Case	**Bioprosthesis type**	**Bioprosthesis Size**	**Echocardiographic assessment**	**Failure mechanism**
1 – HER	Edwards Perimount	23 mm	Mod-severe aortic regurgitation	Calcified leaflet prolapse
2– MAG	Edwards SAV	25 mm	Severe aortic steno-insufficiency	Calcified pannus and Leaflet tears
3 – BOU	Edwards SAV	23 mm	Severe aortic stenosis	Leaflet calcification
4 – DAV	Medtronic Mosaic	23 mm	Normal	Infection

The failure mechanism for each studied case is as follows:

Case #1. (HER) The pericardial degenerated bioprosthesis showed a calcified leaflet with associated prolapse as shown in Fig. 3.13.

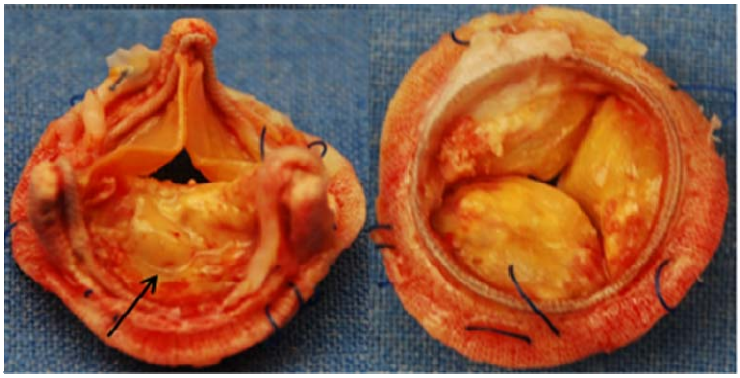

Fig. 3.13 : Case n°1 – explanted pericardial bioprosthesis showing a calcified leaflet prolapse.

Case #2. (MAG): The porcine degenerated bioprosthesis was characterized by leaflet tears but also and especially by the presence of a strongly calcified subvalvular pannus overgrowth, responsible for a non structural valve dysfunction as shown in Fig. 3.14. The pannus was absolutely not detected at standard preoperative assessment.

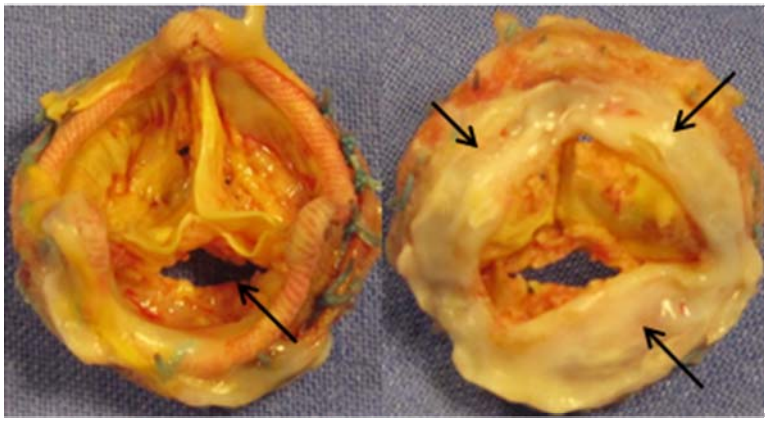

Fig. 3.14: Case n°2 – explanted porcine bioprosthesis showing leaflet tear and calcified pannus.

Case #3. (BOU) The porcine degenerated bioprosthesis showed one leaflet calcification (Fig. 3.15) responsible for high preoperative gradients.

Fig. 3.15：Case n°3 – explanted porcine bioprosthesis showing one leaflet calcification.

Case #4. (DAV) The porcine bioprosthesis showed leaflet thickening as starting process of infective endocarditis, absolutely not detected to preoperative assessment (Fig. 3.16).

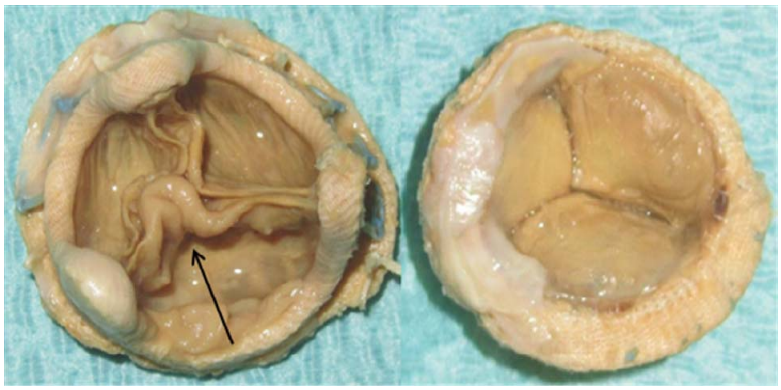

Fig. 3.16：Case n°4 – explanted porcine bioprosthesis showing leaflet infection.

We obtained in-vivo and ex-vivo acquisition for all databases. The main image resolution parameters derived from the CT acquisitions using the above mentioned protocols and retrospective reconstruction (in-vivo) are summarized in Tab. 3.4.

Tab.3.4: Image resolution parameters of in-vivo (IV) and ex-vivo (EV) acquisitions

Patient	Observation	Image size (voxels in X,Y,Z)	Image sampling (mm in X,Y,Z)
HER	IV	512 512 281	0.3125 0.3125 0.625
	EV	512 512 198	0.3125 0.3125 0.3125
MAG	IV	512 512 105	0.318 0.318 0.312
	EV	512 512 110	0.0966 0.0977 0.312
BOU	IV	512 512 153	0.3632 0.3632 0.625
	EV	512 512 120	0.0977 0.0977 0.312
DAV	IV	512 512 290	0.418 0.418 0.635
	EV	512 512 125	0.0977 0.0977 0.3125

3.5.2 Results of Denoising

Preprocessing to reduce noise is necessary only for in-vivo images. The structures of interest (stent, leaflets and calcification/pannus) were well contrasted in ex-vivo images. They did not need to be preprocessed. Examples of original in-vivo images for the four considered cases are shown in Fig. 3.17.

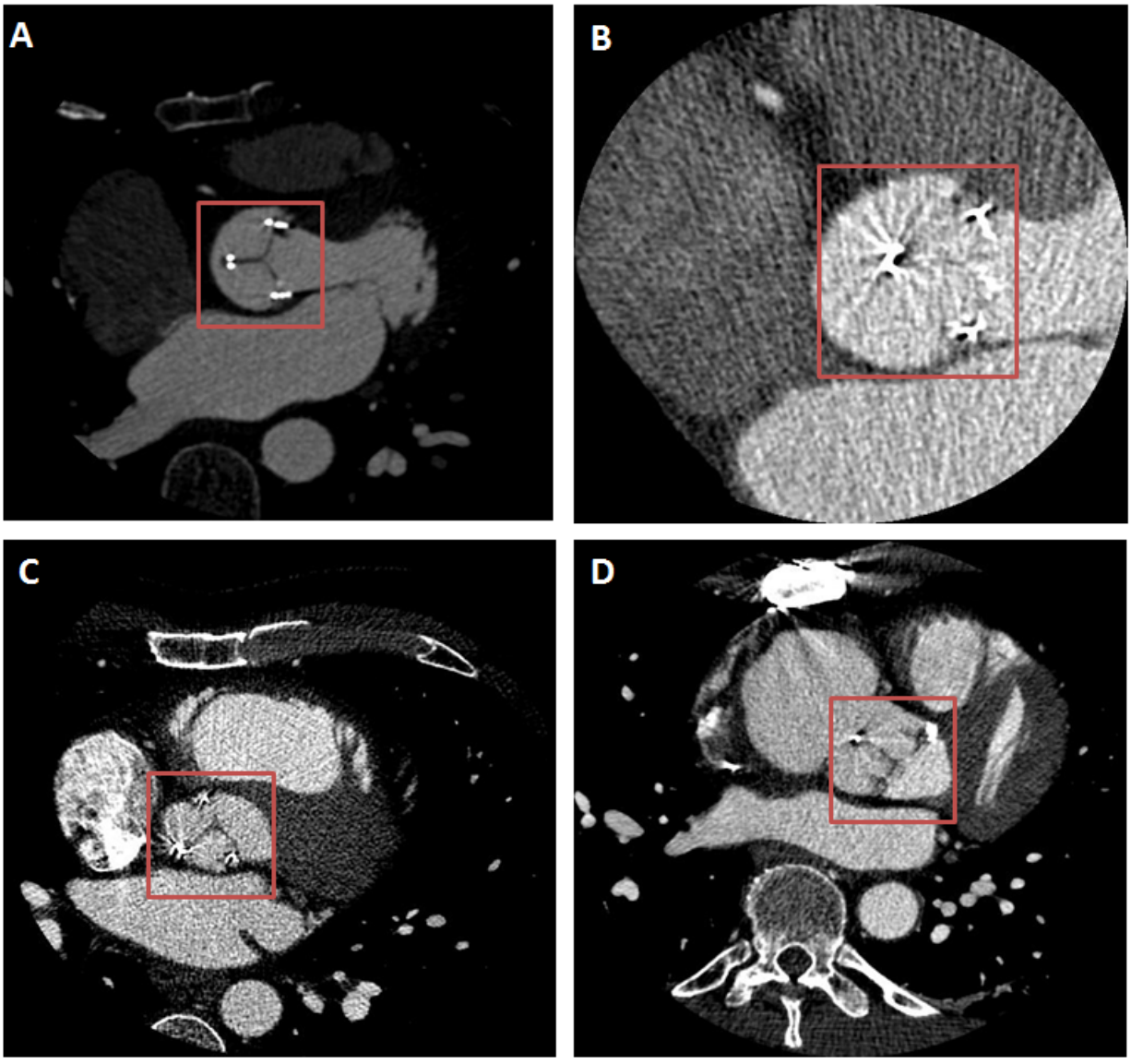

Fig. 3.17: Examples of original images: HER (A), MAG (B), BOU (C) and DAV (D). Regions located in the red square include the bioprosthesis.

The bioprosthesis volume was first isolated by considering the ROI defined by the stent in in-vivo images. Then, the preprocessing based on a simple classical median filter, on anisotropic diffusion filters (PM, Catté_PM, MmCF and ACD) and on stick filters (Original Stick, Modified Stick) was applied to the in-vivo CT volumes of the four patients. Resulting images obtained with the 7 different filters are reported in Fig. 3.18a-3.18d.

A first qualitative appreciation of the results lets appear that the approach based on the modified stick filter seems to best enhance the contrast between valve leaflets and surrounding structures.

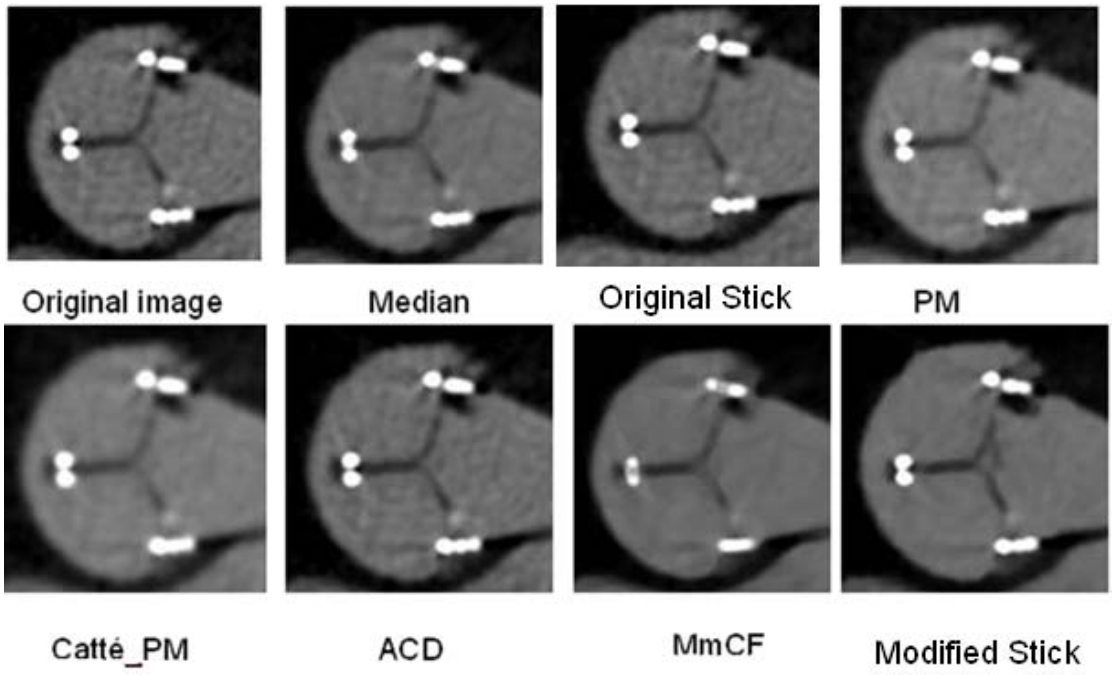

Fig. 3.18a: Filtering of case 1 - HER (original image and results obtained with the 7 different filters).

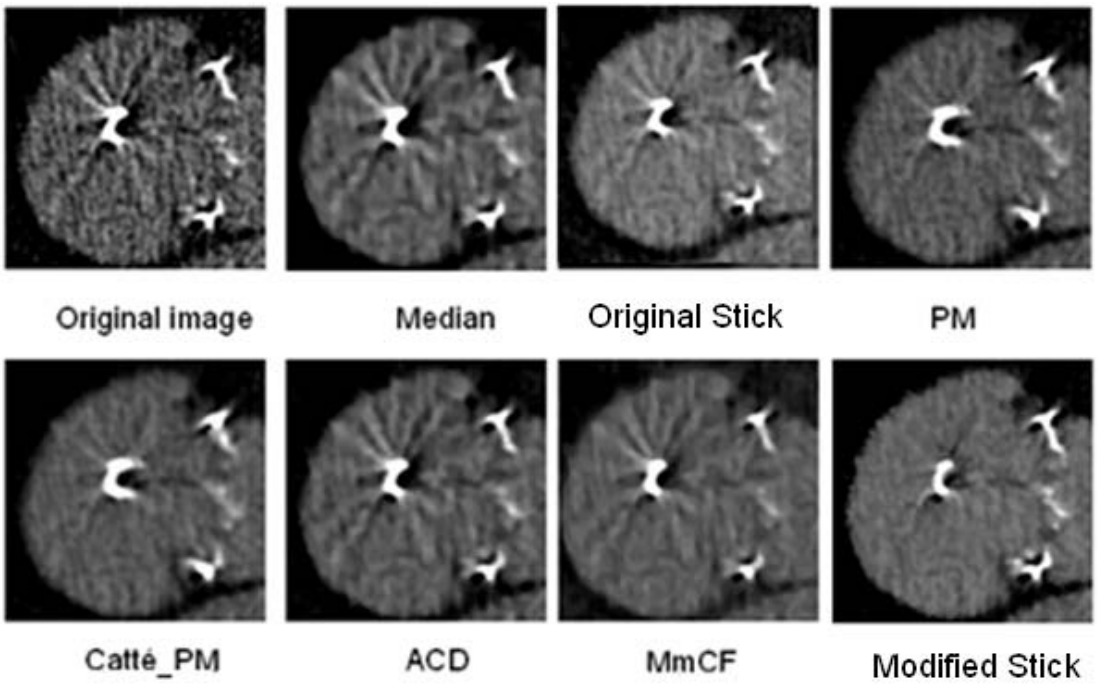

Fig. 3.18b: Filtering of case 2 - MAG (original image and results obtained with the 7 different filters).

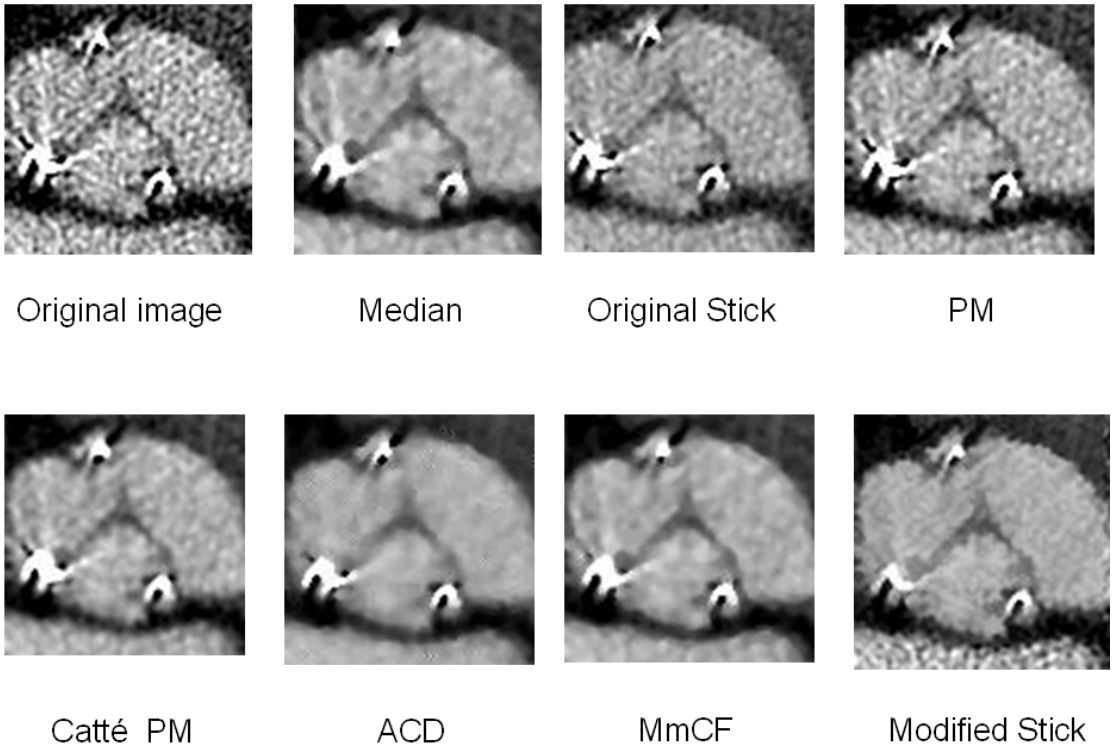

Fig. 3.18c: Filtering of case 3 - BOU (original image and results obtained with the 7 different filters).

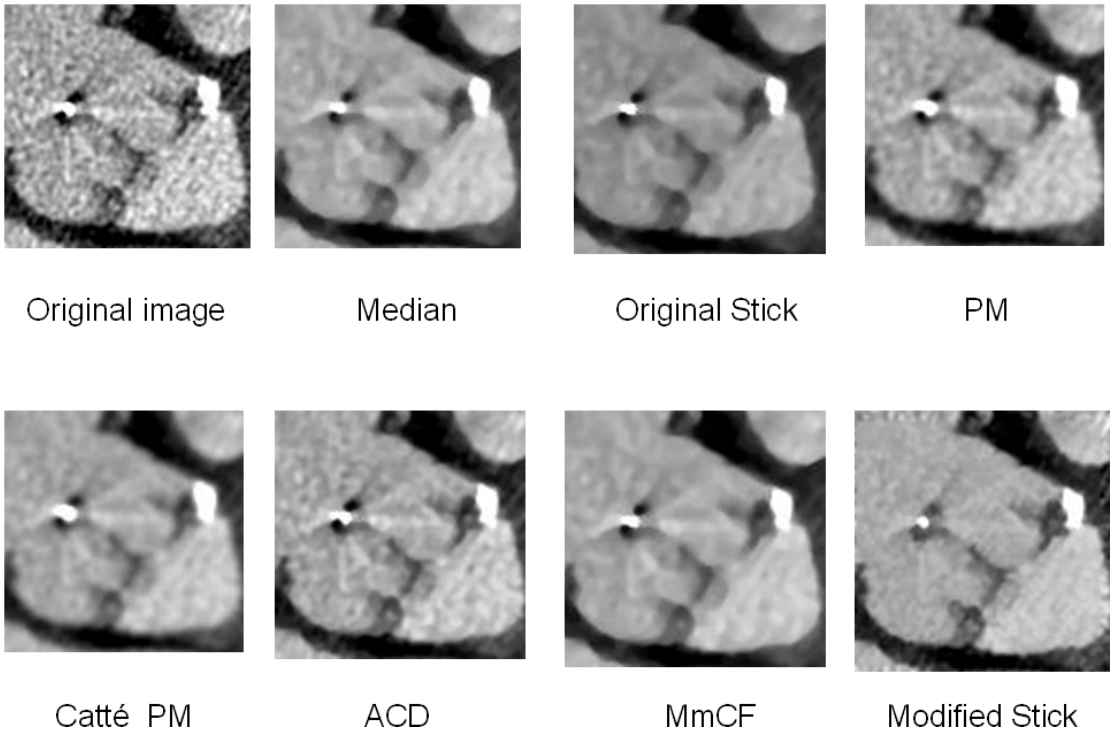

Fig. 3.18d: Filtering of case 4 - DAV (original image and results obtained with the 7 different filters).

In addition to this qualitative assessment of the results, SNR was computed on original images and resulting images (Tab. 3.5). This objective assessment shows (Fig. 3.19) that stick filtering shows the best SNR for the four patients and this is consistent with the subjective appreciation.

Tab. 3.5: SNR of original images and resulting images

	Original	Median	Original Stick	PM	Catté PM	ACD	MmCF	Modified Stick
HER	12.5	27.4	27	27.2	28	27.5	27.2	28
MAG	7.5	10	14.2	11	14	14.5	13.7	15.8
BOU	5.5	6.2	7.1	6.5	7.2	7.5	7.3	13.5
DAV	7.2	14	15.9	12.6	15.8	16.5	17.2	17.5

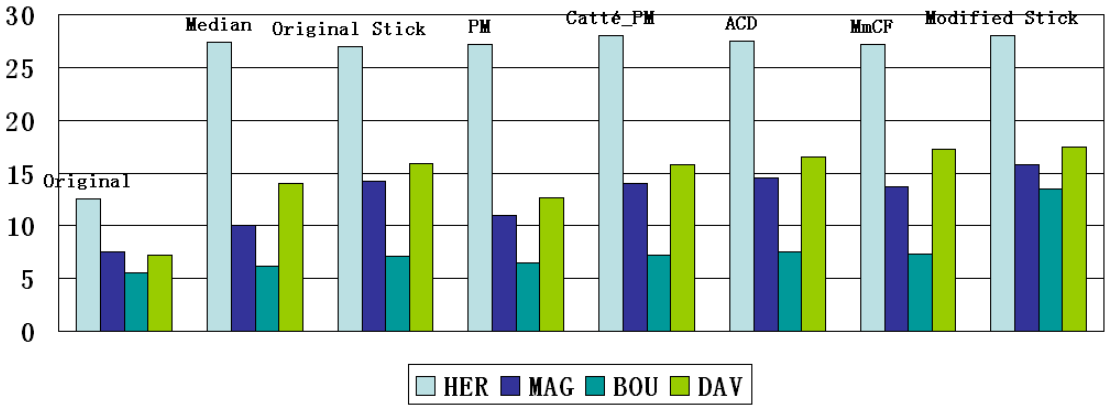

Fig. 3.19: SNR of original images and results after denoising with the different filters.

We can appreciate that in the case of high SNR images (HER) all of the filters can give good results.

The quality of filtering with Median filter depends on the size of the neighborhood. The median filter can keep object details larger than half of the considered neighborhood. Thus the best result was obtained when the size of the neighborhood was less than the thickness of leaflets (radius typically less than 3 voxels) and higher than the pattern of noise (such as in the case of DAV). This parameter is difficult to set when the thickness of leaflet is close to the thickness of noise pattern. It was the case for MAG and BOU. If a larger neighborhood is used, this may reduce the details of leaflets too much.

In the four models we considered for anisotropic diffusion filtering, the most sensitive parameter was the number of iterations. In our experiments the number of iterations was fixed according to the SNR. When SNR was not increased between two successive iterations, the filtering process was stopped. PM model have the worst performance. For instance in the case of BOU, it is

difficult to appreciate the enhancement obtained on the resulting image (even after more than 20 iterations).

Catté PM model gives better results than PM model, but the size of Gaussian convolution kernel is difficult to determine. Even when we use the smallest kernel (radius=1 voxel), details of the structures of interest are smoothed. Larger convolution kernel may cause much more smoothed result with residual noise due to the non Gaussian distribution of the original noise.

Anisotropic curvature diffusion and Min max curvature flow have similar performance, better than PM model and Catté PM model. Due to their directional filtering abilities these methods result in an undesired enhancement of metal artifacts. This drawback was also encountered with the original stick filter.

Modified stick filter show better results than others, in almost all cases. We used a stick length of 5 voxels in all cases. In the case of BOU (worst original SNR), it keeps most of the details of leaflets while reducing noise as well as ACD and MmCF. Thus, we can see that the SNR obtained with the modified stick filtering in the case of BOU is much better than the SNRs resulting from diffusion filtering. This is mainly because a “leafletness” measure was introduced in the classification process of modified stick filtering.

In addition, we can see that modified stick filter can reduce metal artifacts in the resulting images. This effect is specific to this filter.

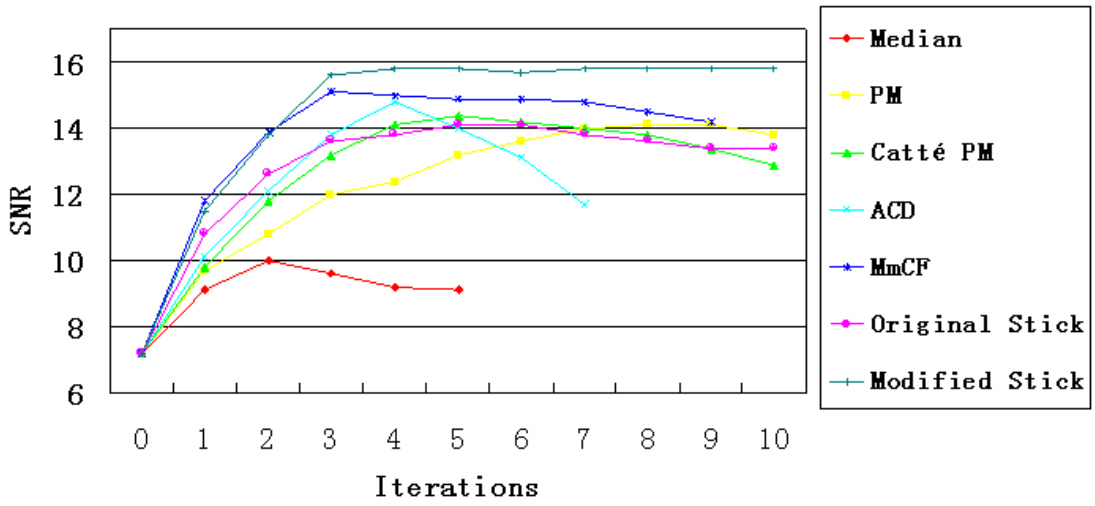

Fig. 3.20: SNR according to the number of iterations in the case n°2 - MAG.

The considered filters can be iteratively applied to the images we want to denoise. Fig. 3.20 illustrates the evolution of SNR, according to the number of iterations, during the denoising process of a low SNR image. From the curves we can see that the modified stick filter has a convergent behavior. The result converges after a few iterations (4 iterations). The same behavior was observed in the other cases (maximum of 4 iterations), with a minimum of 2 iterations in the case of HER.

The main drawback of the modified stick filter is the computation time. In the case of 5 voxels length stick, 386 sticks have to be analyzed for each voxel of the ROI. This analysis includes median value calculations which are time consuming but could be parallelized. Anisotropic diffusion filters, with same size of neighborhood, require the calculation of 728 discrete gradients or 364 curvatures, which are much less time-consuming operations.

3.6 CONCLUSION

Looking at CT preoperative images the problem was mainly represented by noise and artifacts. For this reason the pre-processing step to improve image quality represents a key point in the analysis of in-vivo databases. Different filters have been tested and proposed to reach the best leaflets enhancement. Among these, the modified Stick filter has shown the best results, confirmed by quantitative SNR analysis. This is certainly thanks to its better applicability to thin structures such as leaflets. Stick filter is performed using MatLab software and it can take time to be realized. In order to reduce its computing time, the selection of a region of interest, that takes into account only the bioprosthesis stent region including the leaflets, seems to represent a good and easy strategy.

REFERENCES

[3.1]. Gardiner G W, Zoller P Quantum noise. Second Edition.

[3.2]. Bartuschat D. A parallel patch-based approach for the reduction of quantum noise in CT images. Master's Thesis of Friedrich-Alexander-Universitat Erlangen, 2008.

[3.3]. Mayer M. A variational approach for the reduction of quantum noise in ct images. Master's thesis, Friedrich-Alexander-Universit¨at Erlangen, 2007.

[3.4]. Jung K., Lee K., Kim S., Kim T., Pyeun Y., Lee J. Low-dose, volumetric helical CT: image quality, radiation dose, and usefulness for evaluation of bronchiectasis. Invest Radiol 2000;35:557–63.

[3.5]. Matthew J. B., Stephan A., Roger S. Blumenthal et al. Assessment of Coronary Artery Disease by Cardiac Computed Tomography. Circulation. 2006;114:1761-1791.

[3.6]. Bartuschat D. A parallel patch-based approach for the reduction of quantum noise in CT images. Master's Thesis of Friedrich-Alexander-Universitat Erlangen, 2008.

[3.7]. Mayer M. A variational approach for the reduction of quantum noise in ct images. Master's thesis, Friedrich-Alexander-Universit¨at Erlangen, 2007.

[3.8]. Watzke O. and Kalender W. A. A pragmatic approach to metal artifact reduction in ct: merging of metal artifact reduced images, Eur Radiol Physics, 2004; 14: 849 – 856.

[3.9]. Bertram M., Rose F., Schfer D., Wiegert J., and Aach T., Directional interpolation of sparsely sampled cone-beam ct sinogram data, in Proceedings of IEEE International Symposium on Biomedical Imaging, 2004: 928 – 931.

[3.10]. Oehler M., Kratz B., Knopp T., Mueller J., and Buzug T. M., Evaluation of surrogate data quality in sinogram-based ct metal-artefact reduction, in SPIE Symposium on Optical Engineering - Image Reconstruction from Incomplete Data Conference, 2008:7076-07:1 – 10.

[3.11]. Zhao S., Robeltson D. D., Wang G., Whiting B., and Bae K. T., X-ray ct metal artifact reduction using wavelets: An application for imaging total hip prostheses, IEEE Transactions on Medical Imaging, 2000:19,12: 1238 – 1247.

[3.12]. Lemmens C., Faul D., and Nuyts J., Suppression of metal artifacts in ct using a reconstruction procedure that combines map and projection completion, IEEE Transactions on Medical Imaging, 2009: 28, 2: 250 – 260.

[3.13]. Yu L., Li H., Mueller J. Metal Artifact Reduction from reformatted projections for hip prostheses in

multislice helical computed tomography: Techniques and Initial Clinical Results. Investigative Radiology: November 2009: 44, 11: 691-696.

[3.14]. Lorenz C., et al. Multi-scale line segmentation with automatic estimation of width, contrast and tangential direction in 2D and 3D medical images. In J. Troccaz, E. Grimson, and R. M¨osges, eds., Proc. CVRMed-MRCAS'97, LNCS, 1997:233–242.

[3.15]. Frangi A.F., Niessen W.J., Vincken K.L., and Viergever M.A.. Multiscale Vessel Enhancement Filtering. W.M.Wells et al. (Eds.): MICCAI'98, LNCS 1496, 1998: 130–137.

[3.16]. Sato Y., et al. 3D multi-scale line filter for segmentation and visualization of curvilinear structures in medical images. In J. Troccaz, E. Grimson, and R. Mösges, eds., Proc. CVRMed-MRCAS'97, LNCS, 1997: 213–222.

[3.17]. Perona P., Malik J. Scale space and edge detection using anisotropic diffusion. IEEE Transactions on Pattern Analysis and Machine Intelligence, 1990, 12(7): 629-639.

[3.18]. Catté F., Lions P., Morel J., et al. Image selective smoothing and edge detection by nonlinear diffusion. SIAM Journal on Numerical Analysis, 1992, 29: 182-193.

[3.19]. You Y., Kaven M. Fourth-order partial differential equations for noise removal. IEEE Transactions on Image Processing, 2000, 9(10): 1723-1730.

[3.20]. Ling J., Bovik A.C. Smoothing low-SNR molecular images via anisotropic median-diffusion. IEEE Transactions on Medical Imaging, 2002, 21(4): 377-384.

[3.21]. Black M.J., Sapiro G. , Marimont D.H., et al. Robust anisotropic diffusion. IEEE Transactions on Image Processing, 1998, 7(3): 412-432.

[3.22]. Yu J.H., WANG Y.Y., SHEN Y.ZH. Noise reduction and edge detection via kernel anisotropic diffusion. Pattern Recognition Letters, 2008, 29(10): 1496-1503.

[3.23]. Yezzi A. Modified Curvature Motion for Image Smoothing and Enhancement, IEEE Transaction on Medical Imaging, 1998, 7 (3).

[3.24]. Qian Y., Zhang Y., Morgan M. A comparison of medical image segmentation methods for cerebral aneurysm computational hemodynamics. Biomedical Engineering and Informatics (BMEI), 2011 4th International Conference, 2011, 2: 901-904.

[3.25]. Brassel M., Bretin E. A modified phase field approximation for mean curvature flow with conservation of the volume, Mathematical Methods in the Applied Sciences 2011, 34(10): 1157–1180.

[3.26]. Manniesing R., Viergever M.A., Niessen W.J. Vessel enhancing diffusion: A scale space

representation of vessel structures. Medical Image Analysis, December 2006:10(6): 815–825.

[3.27]. Malladi R., Sethian J.A. Image Processing: Flows under Min/MaxCurvature and Mean Curvature. Graphical Models and Image Processing, March 1996:58(2): 127–141.

[3.28]. Yu H., Bennamoun M., Chua C.S. An extension of min/max flow framework. Image and Vision Computing March 2009: 27(4,3): 342–353.

[3.29]. Kalra M.K., et al. Can noise reduction filters improve low-radiation-dose chest CT images? Pilot study Radiology 2003: 228 257–64.

[3.30]. Martinsen A., Saether H., Olesen D., Wolff P. and Skaane P. Improved image quality of low-dose thoracic CT examinations with a new postprocessing software J. Appl. Clin. Med. Phys. 2010:11 250–58.

[3.31]. Chen Y. et al. Improving low-dose x-ray CT images by weighted intensity averaging over large-scale neighborhood Eur. J. Radiol. 2011: 80 e42–9.

[3.32]. Mendrik A.M. et al. Noise reduction in computed tomography scans using 3D anisotropic hybrid diffusion with continuous switch. IEEE Trans. Med. Imaging. 2009:28 1585–94.

[3.33]. Fernandes L, Oliveira M. Real-time line detection through an improved Hough transform voting scheme, Pattern Recognition, Elsevier, Volume 41, Issue 1, pp. 299–314 (January, 2008).

[3.34]. González R C, Woods U. Digital image processing. Prentice Hall (2008).

[3.35]. Czerwinski R N, Jones D L. Line and boundary detection in speckle images, IEEE Trans. Image Processing 1998;7: 1700–1714.

[3.36]. Xiao C, Su Z, Chen Y. A Diffusion stick method for speckle suppression in ultrasonic images, Pattern Recognition Letters 2004; (25)16:1867-1877.

IV - SEGMENTATION

The output of the pre-processing step based on stick approaches provides enhanced images with higher SNR. The segmentation issue is here more particularly focused on bioprosthetic leaflets and their degeneration. In this chapter, we first summarize the main algorithms of segmentation reported in the case of cardiac vascular structures, *i.e.* coronaries, ventricular, aortic dissection. Then, three kinds of region-based segmentation processes are described, with a decreasing level of user interactivity. They are applied to the pre-processed MSCT data set. Segmentation methods based on the consideration of stick neighboring are considered. Results of the different segmentation methods are reported and a volumetric analysis process is described.

4.1 STATE OF THE ART: CARDIAC SEGMENTATIONS

Image segmentation is the process of partitioning a digital image into multiple sets of pixels, or segments. The objective is to change the representation of the image into a description that is more meaningful and easier to analyze [4.1]. It plays a major role in many medical imaging applications, by automating or facilitating the delineation, localization and characterization of anatomical structures and other regions of interest. A lot of segmentation methods have been reported in the literature. They are based on different kinds of approaches such as region-based, boundary-based, model-based or a combination of these approaches.

In the following we do not draw up an exhaustive presentation of the different methods. We focus on some of these methods which have been reported or could be used to segment cardiovascular CT images.

4.1.1 Boundary-based (contour-based) methods

Active contour methods, often called snakes, are certainly the first solutions one might consider [4.2]. The snake-segmentation algorithm is an iterative contour -based approach introduced by Kass for the segmentation 3D images. A snake-contour is represented by a parametric curve v(s). The snake-contour is iteratively adapted by a dynamic process which minimizes the energy E(v(s)). This energy can be composed of different terms including internal (snake

curve) and external (image features) dynamic energies.

The main advantages of snake methods is that it allows for picking out a desired object in a collection of objects with similar attributes. With more or less interactivity, snakes minimize an energetic criteria in order to find the more accurate border of the object. This kind of algorithm was largely used for the segmentation of medical images, such as the segmentation of vascular structures in ultrasound and CT images. Unfortunately, the complex parameters that snakes include may lead to instability.

Other methods such as Live-wire [4.3-4.5] are included in this category. The user initially selects a point on the boundary of the object. All the possible minimum-cost paths from this point to all other points in the image are analyzed to extract a 2-D boundary. Subsequently, a live wire is displayed in real time from the initial point to any subsequent position taken by the cursor.

In the live-wire-on-the-fly method [4.3], the user-interaction process remains the same, a linear time complexity graph-search algorithm used to save a considerable amount of user time by avoiding the computation of all possible minimum-cost paths. When the user selects a point on the boundary, the live-wire segment is computed and displayed in real time from the selected point to any subsequent position of the cursor in the image.

Another kind of methods is based on watershed segmentation algorithm presented by Vincent *et al.* in 1991 [4.6 - 4.9]. Watershed segmentation decomposes an image into regions which represent the influence areas of the

intensity local minima. In analogy with topography, if the image is considered as an elevation map, each watershed region is a distinct catchment basin, separated from adjacent basins by higher intensity ridges. For this reason, applying the watershed to a gradient magnitude image is a means of separating objects by their contours. Watershed algorithm can deal with the segmentation of relatively large objects with smooth edges. In cardiac images, it was used to segment ventricular cavity.

Such approaches, focused on frontiers detection, may pose problems when the object to segment presents holes or discontinuities in its border (such as trabecular structures, which are present at the borders of the left ventricle).

4.1.2 Region based approaches

Region-based approaches have been privileged in segmentations for cardiac images. In this perspective, Level set, Fuzzy Connectedness and Graph-cut methodologies seem to provide the best results in medical contexts [4.10].

Although region based segmentation methods mentioned have been proposed to develop tools for cardiac imaging, giving access in the same time to different aortic structure (ventricles, aorta, vessels and dissections), more simple methods have also their value in the segmentation process especially in interactive segmentation for complex structures.

Thresholding is the most simple and widely used segmentation approach [4.11]. It uses single threshold (image is segmented as object and surround) or

multiple thresholds to segment voxels into different regions. These thresholds can be determined from the histogram of the image. The performance of this kind of approach is very limited in the presence of noise.

Approaches based on region growing compare features of neighboring voxels, such as local variance, difference of gray levels, texture, with those of current voxel to decide if the neighboring voxels could be included into the segmented region or not [4.12-4.14].

These approaches require one or several initial points (seeds) located inside the object of interest. In some cases (thin structures) the seeds must be precisely positioned. This initialization is usually manual. Neighboring voxels which are included into the segmented region are considered as new seeds and the process is iterated until no new seed can be included.

Region growing does not require the exploration of the whole image. The exploration process is driven by the data (seed points). If the criterion used for the aggregation of voxels is too selective a lot of seeds are required, especially in the presence of noise. In case of over-segmentation (small homogeneous sub-set) a fusion step has to be applied to recover the structures of interest.

The level-set segmentation algorithm was developed by Stanley Osher and James Sethian in the early 1987 [4.15], and has been the improved in 2003 [4.16].

The level-set is defined by a parameterized closed curve or contour. Curve propagation is controlled by an implicit function which is calculated from the positive values of the region outside the contour and the negatives values of the region inside the contour.

Although impressive results are reported in the literature, presenting this kind of approach as an adaptive, flexible and efficient method in the field of medical imaging and diagnostic applications, level-set methods with shape priors have also some limitations. They are often slow, do not always generalize well to 3D, and can be difficult to implement [4.17].

Fuzzy Connectedness methods [4.18] are fuzzy approaches which associate seed points (selected interactively) with each object to segment and then build a connectedness map which symbolizes the strengths of the link (connectedness) between each spell (generalization of the pixel or voxel notion) of the map and the seed point. The map is to be threshold to keep the area matching with the object of interest.

In Graph-cut methods [4.17, 4.19, 4.20], the user has to select one region of the background and one region of the object for the initialization of the process and the minimization of an energy criterion by graph-cut algorithm is applied.

4.1.3 Model based Methods

Much of the works done on 3D cardiac segmentation are model-based

[4.21-4.25]. One of the most important model-based methods is 3D geometrical moments [4.26]. It can be used to characterize images. Moments of order pqr are defined as:

$$M_{p.q.r} = \int_x \int_y \int_z x^p y^q z^r f(x,y,z) dxdydz \tag{4.1}$$

where x, y, z are the voxel coordinates, and f is the image function.

Voxels in different kinds of structures have different features that can be described with these moments. They were used for the segmentation of surfaces. This technique has also been to detect tubular structures in images. Analytical expressions have been developped to calculate features of local vessels in MRI [4.9]. In 2006, Bousse et al. applied these expressions to the characterization of vascular structures in CT.

4.1.4 Segmentation and visualization

In medicine, or in other areas, the objective is not only to give the perception of the data, but also to design tools to understand the underlying and relevant information they bring [4.27]. Two classes of rendering have been widely used in medical image visualization: surface rendering and volume rendering. In this section, results of segmentations are performed by surface rendering.

Surface rendering relies on a previous binarization, or segmentation, of the structures of the objects of interest and the tesselation of the surface initially described by sparse or dense 3D point sets, with our without organization

(scattered points or multiplanar arrays). Surface renderings can also use voxel-based techniques: surface elements are indifferently voxels, faces of voxels or triangles estimated from the examination of the voxel neighborhood topology (Marching cube algorithm [4.28]). Surface tracking is then performed within the volume, binary or not, to extract the surface components. The rendering is be carried out by using either depth shading, depth gradient or gradient shading [4.29].

4.2 METHODS

The issue of segmentation is more particularly focused here on bioprosthetic leaflets and their degeneration. According to surgical expertise, four main classes of tissues were identified. They were related to Hounsfield Units (HU) measured by CT. We considered, from high to low HU, the following classes: stent, calcification, vascular lumen and leaflets. The first element (stent), showing high CT values, can be easily segmented by thresholding.

Three kinds of region-based segmentation processes were implemented, with a decreasing level of user interactivity.

4.2.1 Isotropic Region Growing

The first segmentation technique was an interactive process in order to provide a reference approach for the assessment of the results. It was based on classical Isotropic Region Growing (IRG) method. Following a preprocessing step, as described above, it was applied using 3D Slicer software [4.25] (Fig. 4.1).

The bioprosthesis volume was interactively and roughly delineated from different CT slices. Multiple seed points (typically 20 seeds or more) were interactively selected for each component of the prosthesis. The region growing algorithm was started (26-neighbour connectivity) with automatic calculation of

the criterion used for the aggregation of voxels. This similarity criterion was based on mean and standard deviation of the voxel values within the considered cubic neighborhood [4.25-4.27]. The extraction and visualization of the resulting 3D surface meshes delineating the regions were performed by using the Marching Cube algorithm [4.30].

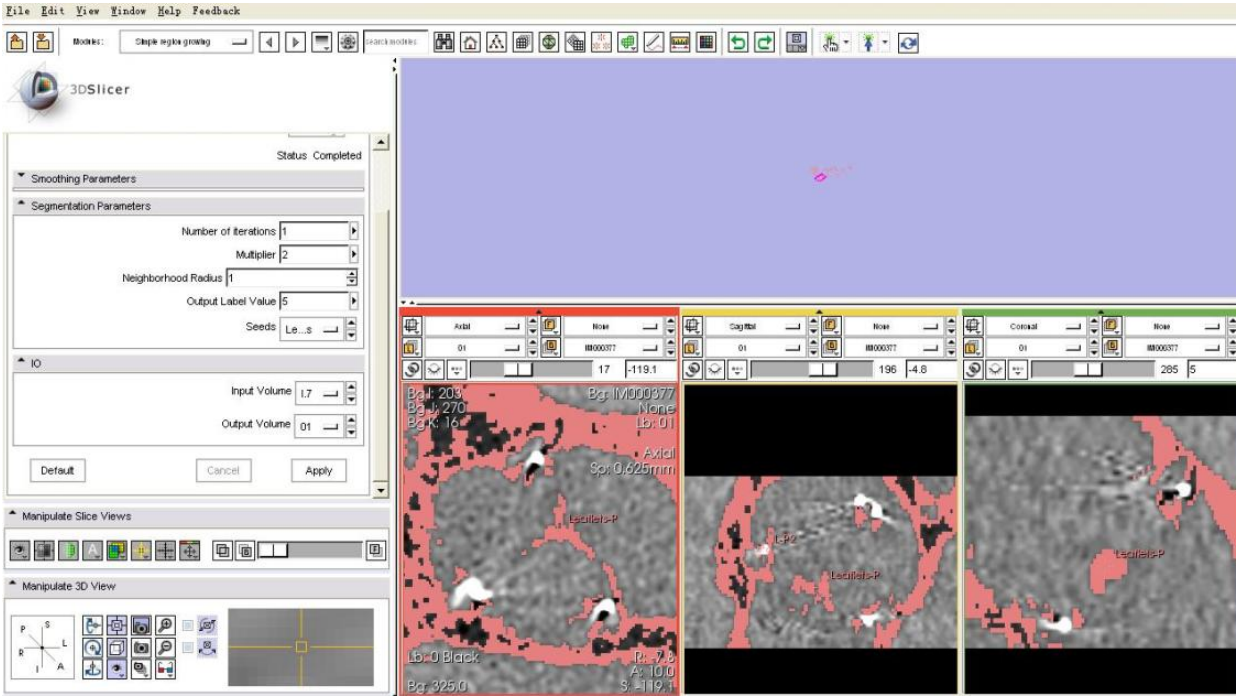

Fig. 4.1: Application example of Interactive Region Growing method by 3D slicer software.

4.2.2 Stick Region Growing

In the denoising step, we noticed that we can classify voxels inside thin structures such as aortic valve leaflets (both natural and bioprostheses) by considering gray level distribution along sticks. We also use features along sticks to determine the direction of region growing.

To deal with the segmentation of thin structures, like the components of a valve bioprosthesis and especially valve leaflets, we developed a directional region growing process based on stick neighborhood.

Some seeds were interactively selected inside the leaflets at different locations. A set of N voxels inside the leaflets was defined by considering for each seed the voxels belonging to their neighborhood.

To ensure region growth is not early stopped, or in other words to limit the number of seed points selection in some critical cases (highly noisy data), the size of the cubic neighborhood was chosen to be large enough to include space between homogeneous fragment of leaflets. We typically used a 342-connected neighborhood (7x7x7).

In order to examine each voxel in the cubic neighborhood of the seed, in the preselected and filtered ROI, the set of asymmetric sticks is analyzed.

We focus on two features, the normal direction to the edge and mean value along stick S_m (the stick with minimum value among local maximum differences along the set of sticks).

For each voxel of the region growing cubic neighborhood we consider a stick neighborhood (as defined previously) to calulate the two features. For each stick, associated with a seed, we calculate the local maximum absolute difference MG_i (defined in section 3.4.2.2) of gray levels between the seed voxel and j^{th} voxels along the i^{th} stick:

$$MG_i = \max_{j=1}^{L}\left(\frac{|I_{i,j} - I_{i,1}|}{dis_{i,j}}\right)$$

where $dis_{i,j} = \sqrt{(x_{i,j} - x_{i,1})^2 + (y_{i,j} - y_{i,1})^2 + (z_{i,j} - z_{i,1})^2}$ is the distance between current voxel and j^{th} voxel.*L* is the length of stick as already defined

In the set of sticks with high *MG* values (sticks crossing edge), we select the stick S_{Ms} with the maximum *MG* value along seed's stick set and S_{ms} as the stick with the minimum *MG* value of seed's stick set.

As we supposed in section 3.4.2.2, the direction of this stick S_{Ms} is orthogonal to an edge, and S_{ms} lies within a thin structure. We calculate the normalized direction vector V_{Ms} corresponding to S_{Ms}, and the local mean value along S_{ms}. Then, we select S_M and S_m for the i^{th} neighboring voxel of seed (marked as S_{Mi} and S_{mi}) and calculate normalized direction vector V_{Mi} of S_{Mi} and local mean value along S_{mi}.

We assume that a set of neighboring voxels located inside thin structures should have similar directions. According to this assumption, we calculate θ_i, which is the angle between V_{Mi} and V_{Ms}:

$$\cos\theta_i = \frac{V_{Ms} \cdot V_{M_i}}{|V_{Ms}| \cdot |V_{M_i}|} \qquad (4.1)$$

If i^{th} neighboring voxel is located in the same thin structure as its seed, this value should be close to 1, *i.e.* the neighboring voxel has similar S_M direction, or close to -1, *i.e.* the neighboring voxel has opposite S_M direction.

Leaflet may not be an ideal thin structure. The regions with large surface curvature (*i.e.* $\cos\theta_i$ is close to 0) might stop the process of region growing

(Fig. 4.2).

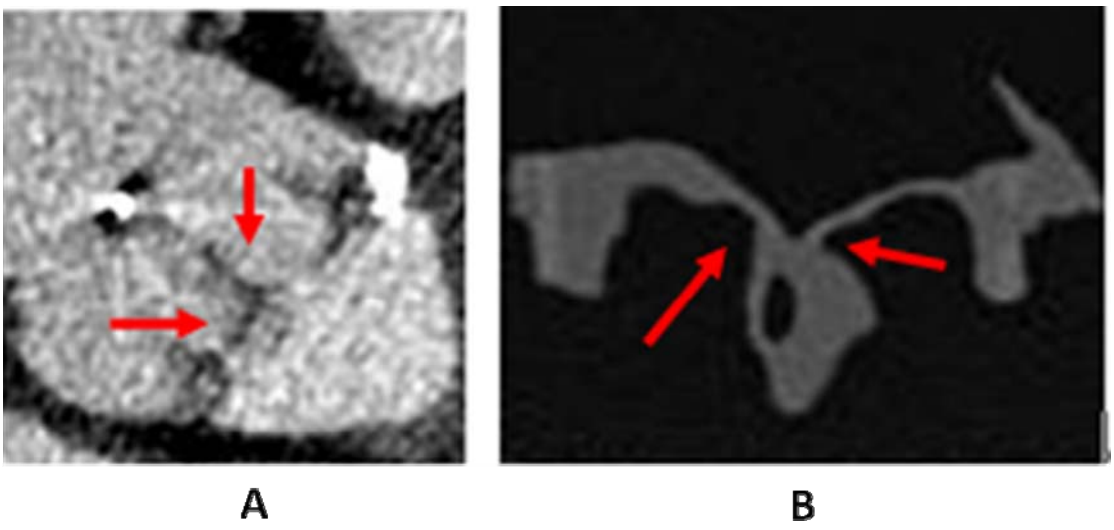

Fig. 4.2: Regions with large surface curvature (indicated by red arrows).

To ensure that the process of region growing is not stopped by this kind of regions, we set two or more seeds on each leaflet (on the commissure and bottom part).

As we discussed in section 3.4.2.2, vascular lumen voxels close to the leaflets could also show opposite directions between S_M and its seed, which is located in the leaflet. In this case, value of neighboring voxel should be considered.

Local mean values along the set of coplanar sticks $S_{MC,}$ which are used to classify structures in section 3.4.2.2, might be suitable to distinguish this kind of voxels from leaflet voxels, but it implies that all of S_{MC} sticks lye within the structure. Leaflet voxels close to edge may have a part of S_{MC} sticks crossing

the edge, and may not have low local mean value. To ensure most of details on leaflet could be detected, we consider S_m rather than S_{MC}.

Leaflet voxels should have low local mean value $\overline{I_m}$ along S_{mi}, (S_m of the ith neighboring voxel) and vascular voxel should have high local mean value along S_{mi}.

The classification of local mean values along sticks is obtained by a thresholding operation. In this case the threshold T_{mean} is determined interactively from the histogram of local mean values along all the sticks in the conformational ROI. It is located between the modes corresponding to vascular lumen and leaflets.

By calculating these features, the neighboring voxels are classified as belonging to the region of the seed voxel (*i.e.* as a voxel of leaflet tissue) when: (i) $\overline{I_m}$ belongs to the gray level range of normal leaflets (*i.e.* lower than T_{mean}); (ii) directions (S_M) orthogonal to the edge are similar or opposed to thoses of their seeds (*i.e.* θ_i has a value close to 0 or 180 degrees). In this case they constitute new seed voxels. This process is iterated until no new voxel can be marked as a seed. This segmentation referenced as Stick Region Growing (Stick RG) in the following is preceded by a Stick filtering preprocessing step. The flowchart of Stick RG is shown in Fig. 4.3.

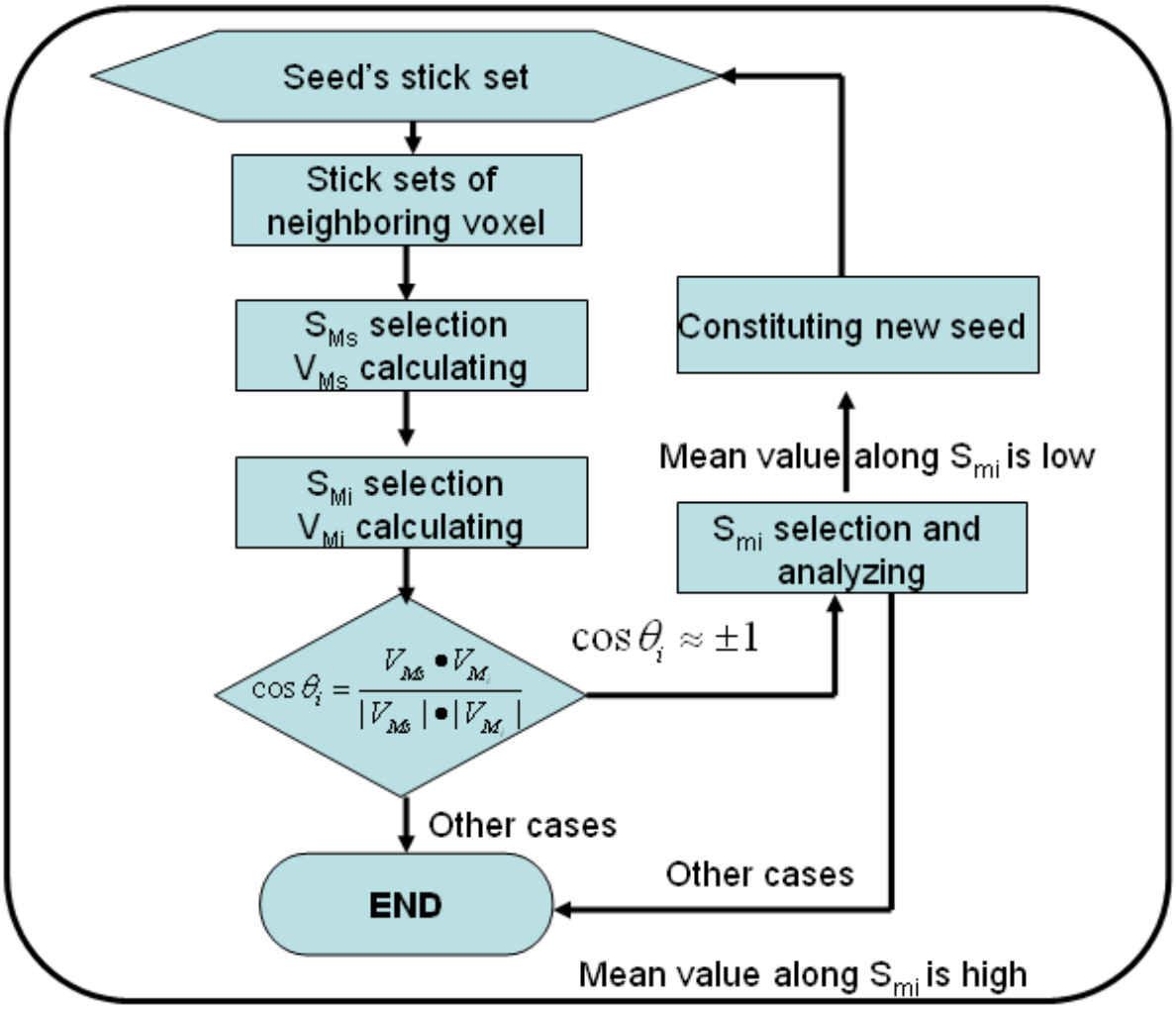

Fig. 4.3: Flowchart of stick region growing

In the segmention of other tissues, $\cos\theta_i$ may give no contribution because of their morphology: tubular shape of stent, unknown shape of vascular lumen and of leaflet alteration. In the case of leaflet alteration, including calcification, there is a poor prior knowledge about the shape of the structure and different gray level distributions can be observed (according to the calcification degree). In the region growing processs, we consider local mean value along S_m . If the stick S_m lies within the same structure, the local mean should be close to the value of the seed and the local variance should be low. The threshold

parameters, concerning mean and variance, are obtained interactively from the gray levels of stent, calcification and vascular lumen in the preselected and filtered ROI.

We designed a region growing process to segment tissues in MSCT data of bioprosthesis. It is mainly based on the consideration of stick neighboring. Local mean values along sticks lying within structures are used in this region growing process. In addition, direction vectors orthogonal to the edge of structures are considered in the case of leaflets.

4.2.3 Stick Exhaustive Search

To further reduce the level of interactivity in the segmentation process, a systematic exploration of the ROI was implemented with no need for seed point definition. This segmentation referenced as Stick Exhaustive Search (SES) in the following was preceded by a Stick filtering preprocessing step.

We divide the neighborhood (Radius=3 pixels, 7*7*7 connected) of each voxel inside the ROI into a set of asymmetric sticks and we automatically select S_M, S_{MC}, S_m, and S_{mc} as we did in section 3.4.2.2. Thus, T_{MG} can be determined automatically by the median of *MG* values along all the sticks in the conformational ROI. Tab 3.1 can be used to indentify voxels belonging to thin structures (including leaflets), vascular lumen, tubular structures (including complete metallic stent) and other structures (including calcifications and

incomplete metallic stent).

Looking at sticks located inside ROI, we determine the thresholds T_{means}. T_{means} is a set of three thresholds used to refine the previous classification and to segment the following components of the bioprosthesis: leaflets, complete metallic stent (high local mean value along S_m), calcifications and incomplete metallic stent (higher local mean gray level value along S_{mC} than vascular lumen). These thresholds are interactively determined from the gray level of stent, calcification and vascular lumen in the preselected and filtered ROI.

With SES it is not necessary to re-select seeds interactively when the segmentation is not validated by the user. SES reduces interactivity but the results can be more influenced by noise than with Stick RG, especially in case of streak artifacts inside vascular lumen.

4.3 RESULTS

Following the preprocessing step, the different segmentation methods (IRG, Stick RG, and SES) were applied to in-vivo (IV) and ex-vivo (EV) images.

In the following, we present the results obtained for each patient (HER, MAG, BOU and DAV) by considering the best CT volume (optimal phase) in the cardiac cycle at the end of the diastole when the aortic valve is closed. Results obtained on slices at different locations in the CT volume are shown. We then present the 3D visualization, with surface rendering, of the in-vivo and ex-vivo valve prosthesis description resulting from IRG, Stick RG and SES segmentations.

The first example is reported in the case of the pericardial bioprosthesis (HER). Thanks to image quality and sharp and regular boundaries of leaflet region, isotropic region growing, stick region growing and stick exhaustive search give qualitatively similar and satisfactory results (Fig. 4.4).

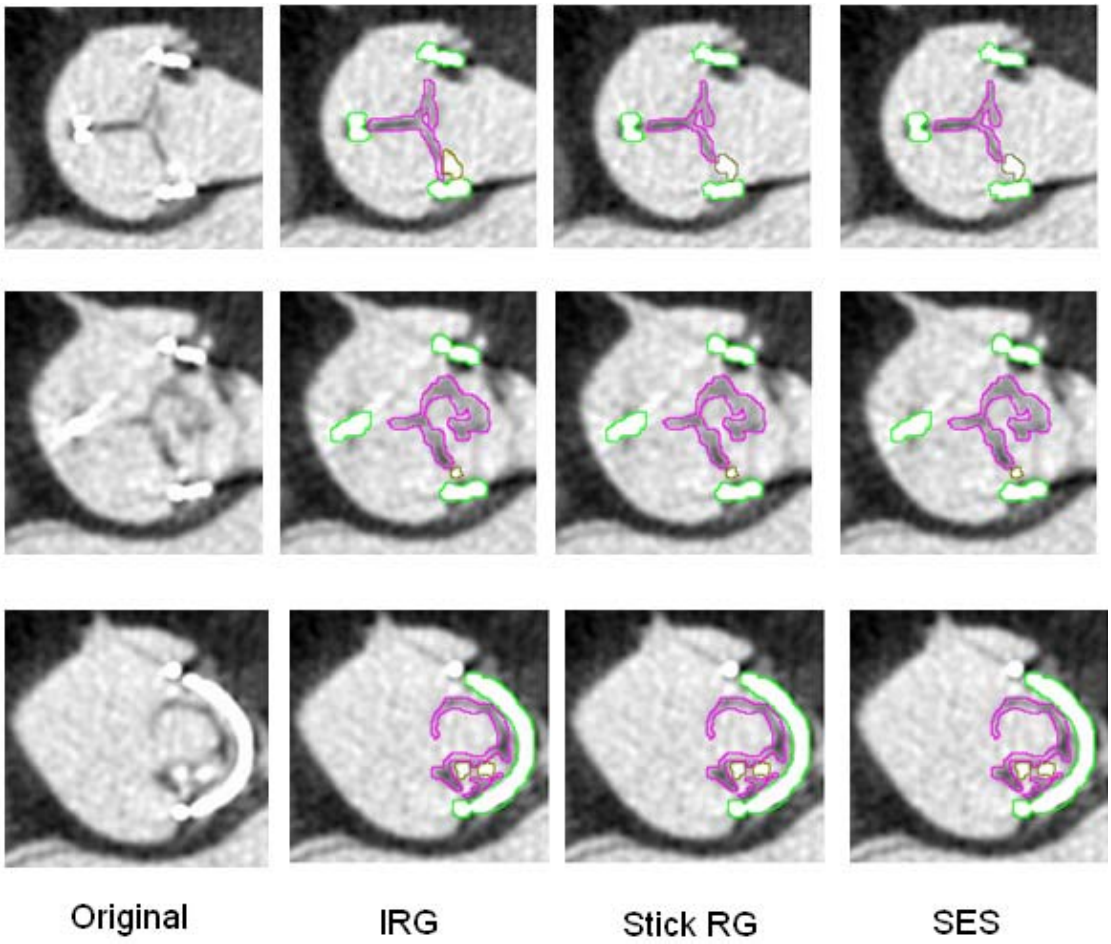

Fig. 4.4: Examples of segmented CT-Slices obtained in case 1 - HER: metallic stent, calcifications and leaflets are indicated by green, brown and purple border respectively.

The visualization of the segmented volume image performed by surface rendering is reported in Fig. 4.5. Mophological similarities between in-vivo and ex-vivo data, as the shape of the leaflets and the presence of a slight degeneration of these leaflets, can be easily appreciated. The leaflet prolapse resulting in no perfect coaptation appears as commissure lost (indicated in blue circle) in the segmented images.

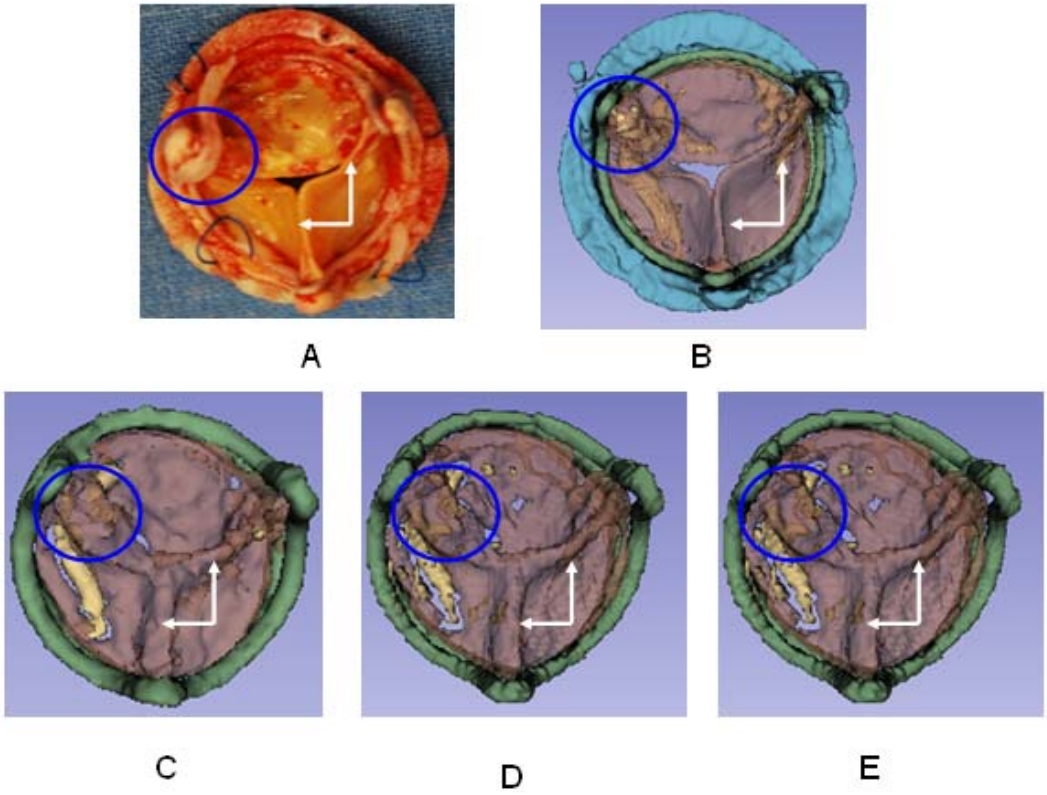

Fig.4.5: Visualization of the segmentation results obtained in case 1 - HER. Explanted bioprosthesis (A), ex-vivo segmented bioprosthesis (B), in-vivo segmented bioprosthesis with methods IRG (C), Stick RG (D) and SES (E). The commissure lost is indicated with blue circle and good leaflets cooptation with white arrows.

The second example illustrates the results obtained in the two cases of porcine bioprothesis (case 3 - BOU and case 4 - DAV). Although the contrasts of images are low, the leaflet boundaries seem to be detected (Fig. 4.6, Fig. 4.7). Nevertheless, compared to interactive segmentation (IRG), stick based segmentations (Stick RG, SES) do not allow in these cases a complete description of the leaflets, especially in the case BOU (Fig. 4.8).

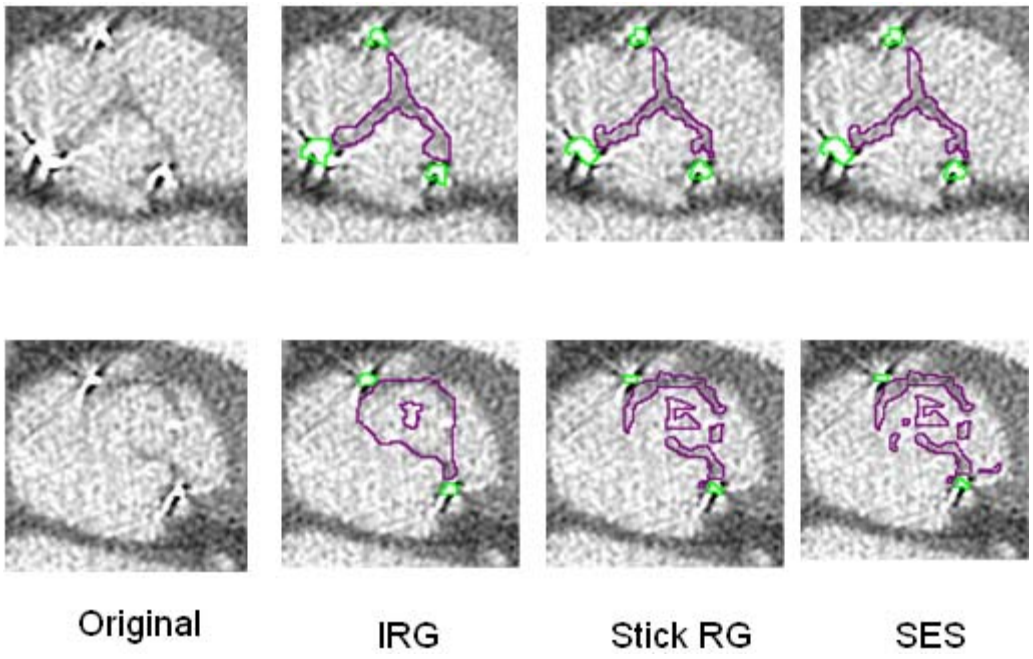

Fig. 4.6: Examples of segmented CT-Slices obtained in case 3 - BOU: metallic stent, calcifications and leaflets are indicated by green, brown and purple border respectively.

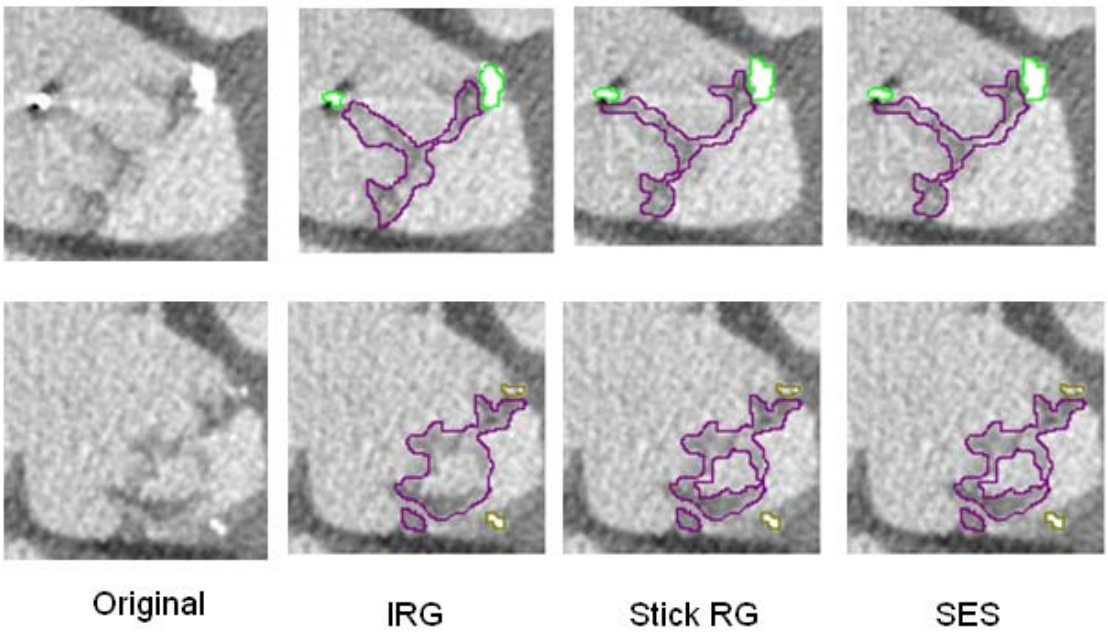

Fig. 4.7: Examples of segmented CT-Slices obtained in case 4 - DAV: metallic stent, calcifications and leaflets are indicated by green, brown and purple border respectively.

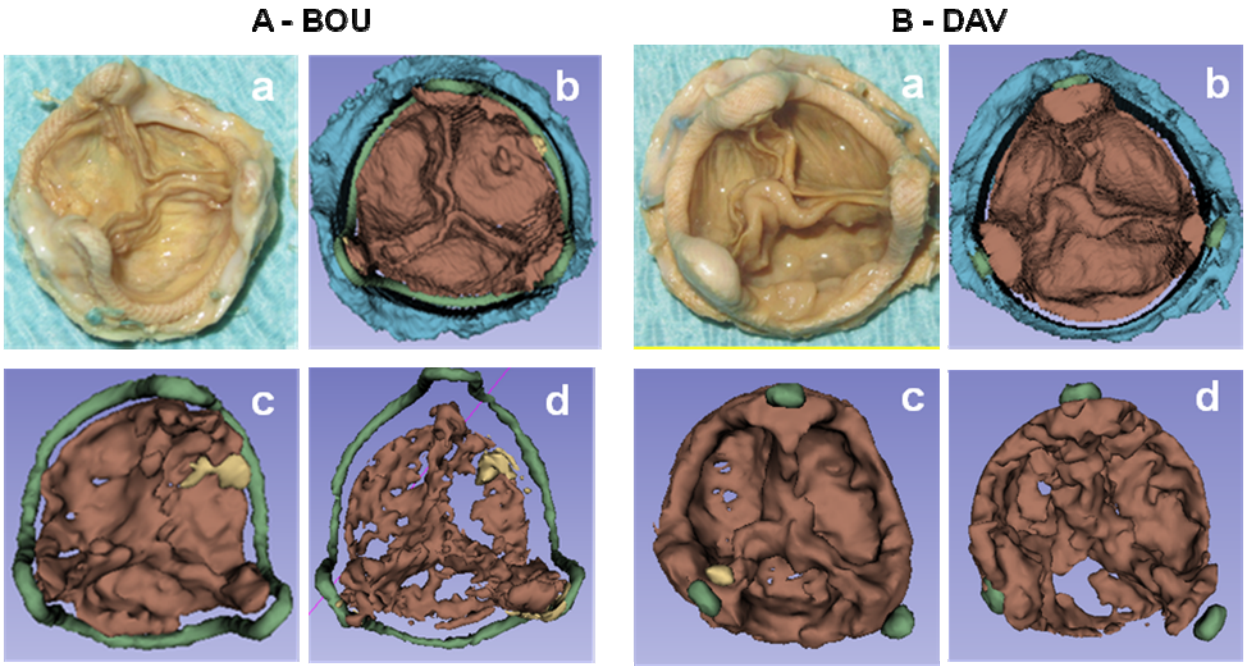

Fig. 4.8: Visualization of the segmentation results obtained in case 3 – BOU (A) and 4 – DAV (B). Explanted bioprosthesis (a), segmented ex-vivo bioprosthesis (b), segmented in-vivo bioprosthesis with methods IRG (c) and Stick RG (d).

From these results (BOU and DAV), we observed that leaflets were not fully segmented: they appear with holes or missing parts. The reason might be related to:

- Calcifications.

In some cases, calcifications are not developed too much (in HER, MAG and BOU). Their density, and therefore the value of the corresponding voxels in CT images, may have value close to that of voxels located in vascular lumen. Segmentations might classify these voxels into vascular lumen structure.

- Partial volume effect

Due to their orientation and their thin thickness, compared to original CT inter-slices distance, leaflets can be affected by partial volume effect,

especially for the part located in axial planes.

To overcome this segmentation default in some cases, the workflow could be composed of two steps:

i) Automatic segmentation based on stick RG (or SES) to describe the main components of the structures.

ii) Interactive segmentation (based on IRG for instance) to complete the description of the missing parts of the leaflets.

Examples of results of BOU and DAV (Fig. 4.9 and Fig. 4.10) obtained with this two-steps approach are reported.

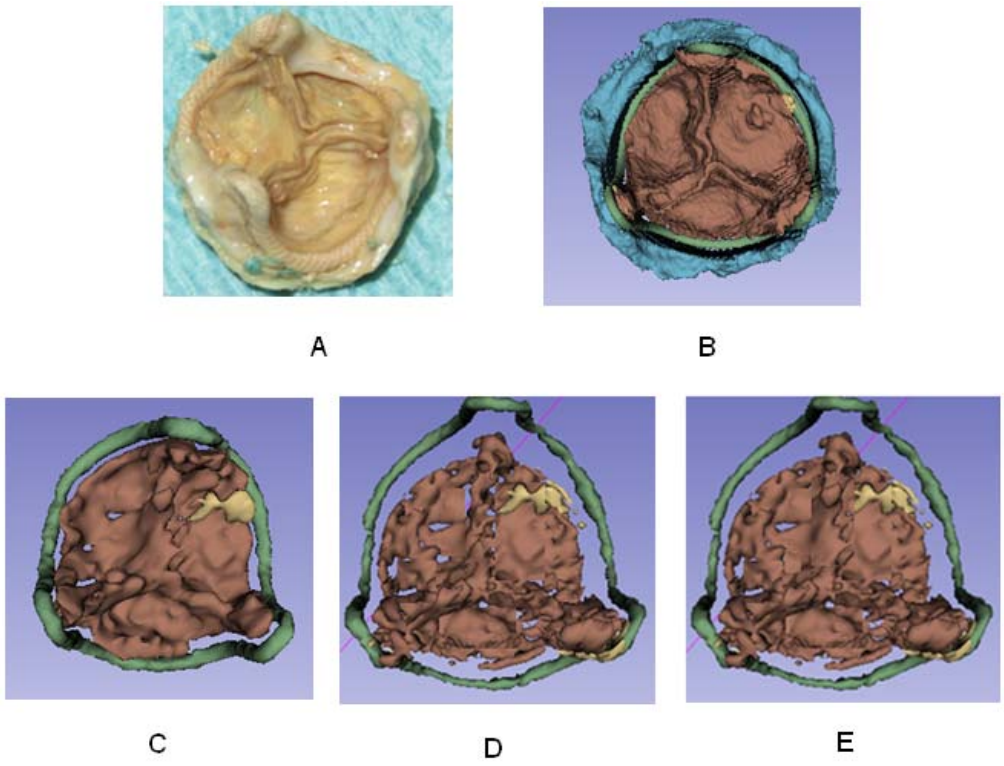

Fig. 4.9: Visualization of the segmentation correction performed in case 3 - BOU. Explanted bioprosthesis (A), ex-vivo segmented bioprosthesis (B), in-vivo segmented bioprosthesis with methods IRG (C), Stick RG with correction (D) and SES with correction (E).

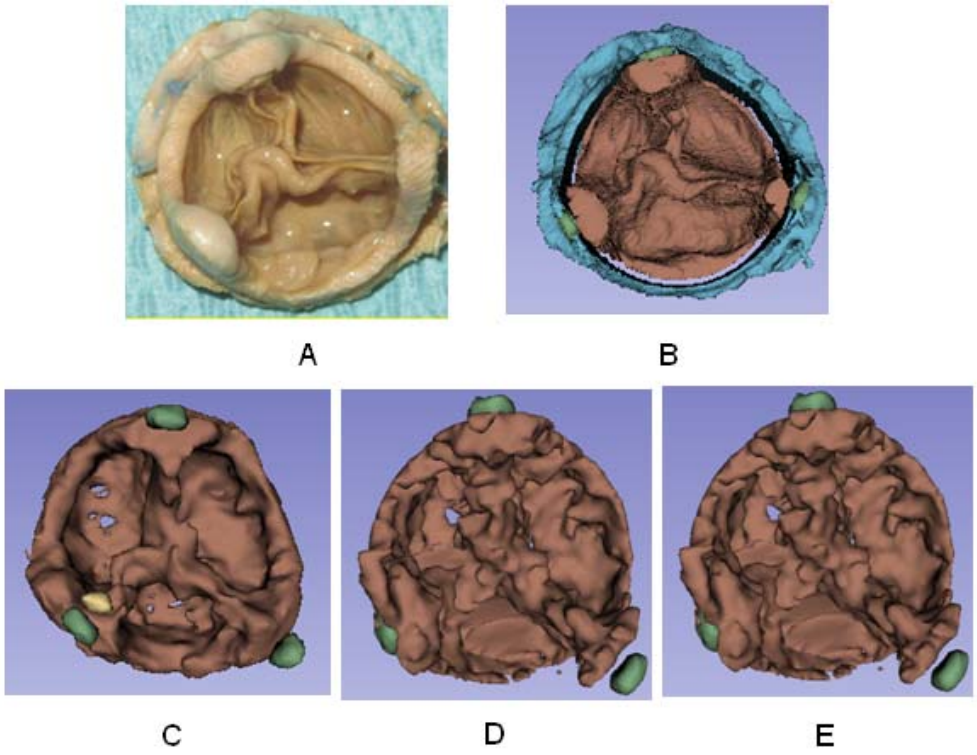

Fig 4.10: Visualization of the segmentation correction performed in case 4 - DAV. Explanted bioprosthesis (A), ex-vivo segmented bioprosthesis (B), in-vivo segmented bioprosthesis with methods IRG (C), Stick RG with correction (D) and SES with correction (E).

The last example illustrates the results obtained in case 2 (MAG) of a porcine bioprothesis. Due to the very-low-contrast structures, segmentation of leaflet was difficult. IRG gave the best but unsatisfactory results in this case. It had to be completed by a manual delineation.

The main difficulty of this kind of data sets is high level of noise and weak (somewhere missing) boundaries. All dark voxels located in the ROI have been classified as leaflets (Fig. 4.11). In addition, there are many incomplete regions in the leaflets.

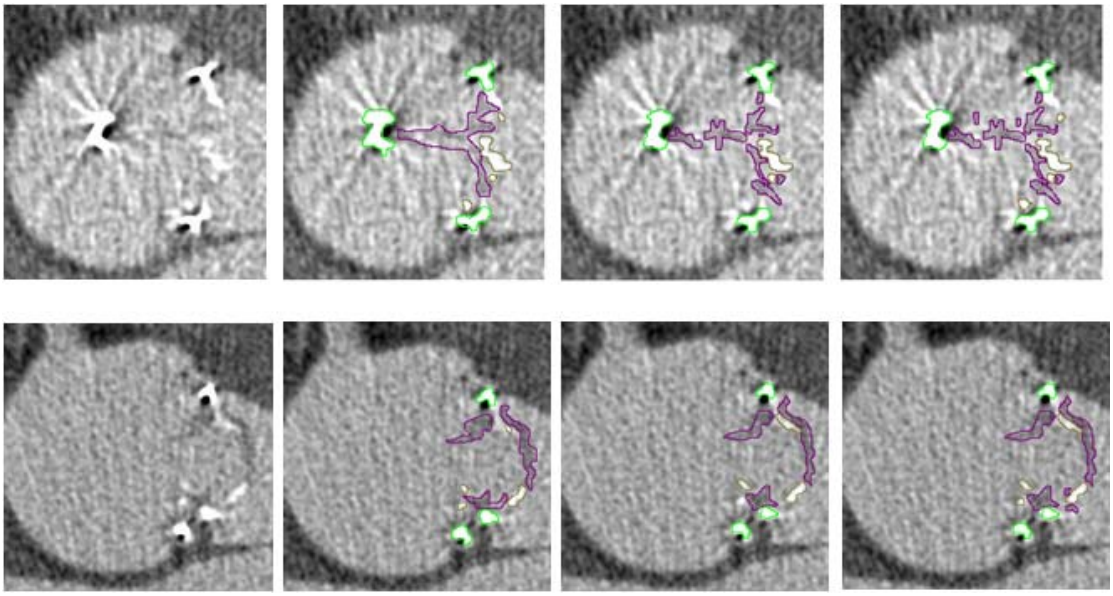

A B C D

Fig. 4.11: Examples of segmented CT-Slices obtained in case 2 - MAG. Original slices (A), results of segmentation performed by IRG (B), Stick RG (C) and SES (D). Metallic stent, calcifications and leaflets are indicated by green, brown and purple border respectively

The visualization of front and back side of bioprosthesis was performed by surface rendering with transparency effect (Fig. 4.12). A calcified pannus (indicated by black arrows) is characteristic in this case and responsible for valve obstruction. Leaflet tears (indicated by green arrows) was also observed and found in reconstructions.

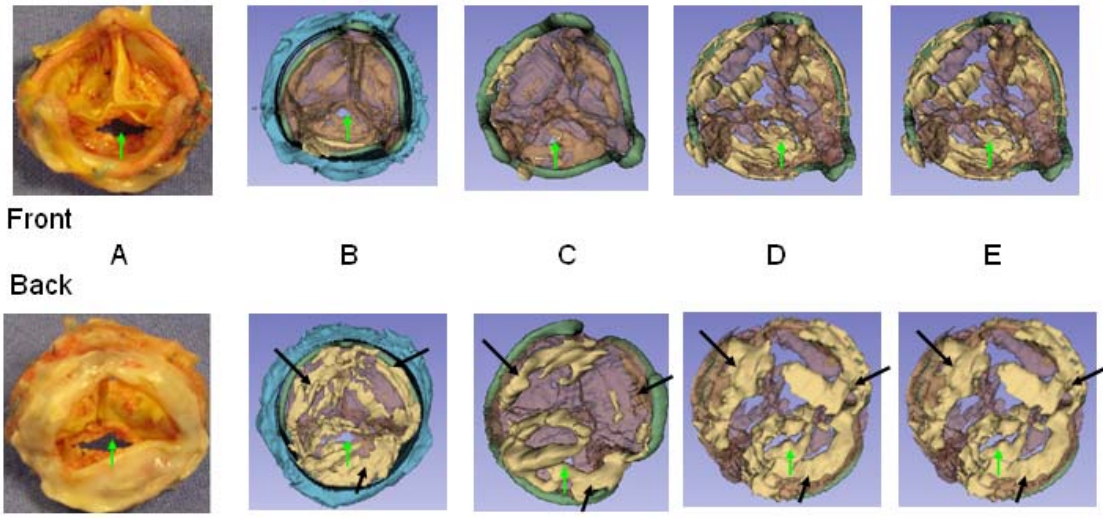

Fig 4.12: Visualization of the segmentation results obtained in case 2 - MAG (Front, i.e. view from aorta and Back, i.e. view from left ventricle). Explanted bioprosthesis (A), segmented ex-vivo bioprosthesis (B), in-vivo segmented bioprosthesis by IRG (C), Stick RG (D) and SES (E). Calcified pannus (indicated by black arrows) and leaflet tears (indicated by green arrows) are observed.

4.4 VOLUMETRIC ANALYSIS

A quantitative analysis was conducted to objectively compare the results obtained respectively by IRG, Stick RG, and SES on in-vivo (IV) and ex-vivo (EV) images. It was performed as following: the voxel volume was computed for each dataset (considering CT acquisition parameters showed in Tab. 3.4) and multiplied by the number of voxels of each bioprosthestic component resulting from the sgementation step. No correction was applied after Stick RG or SES.

The criterion used to evaluate the results was the volume of bioprothesis components. Results of this analysis are shown in Fig. 4.13 (volumes are expressed in mm^3).

This analysis seems to show that the 3 segmentation methods (IRG, Stick RG, SES), more or less automatic, allow to enhance bioprosthetic components including leaflets with similar results. In-vivo volumes are generally bigger than ex-vivo and it can be explained mostly by the moving artifacts. For sure, ex-vivo results are more reliable than in-vivo and represent the reference to assess the in-vivo results.

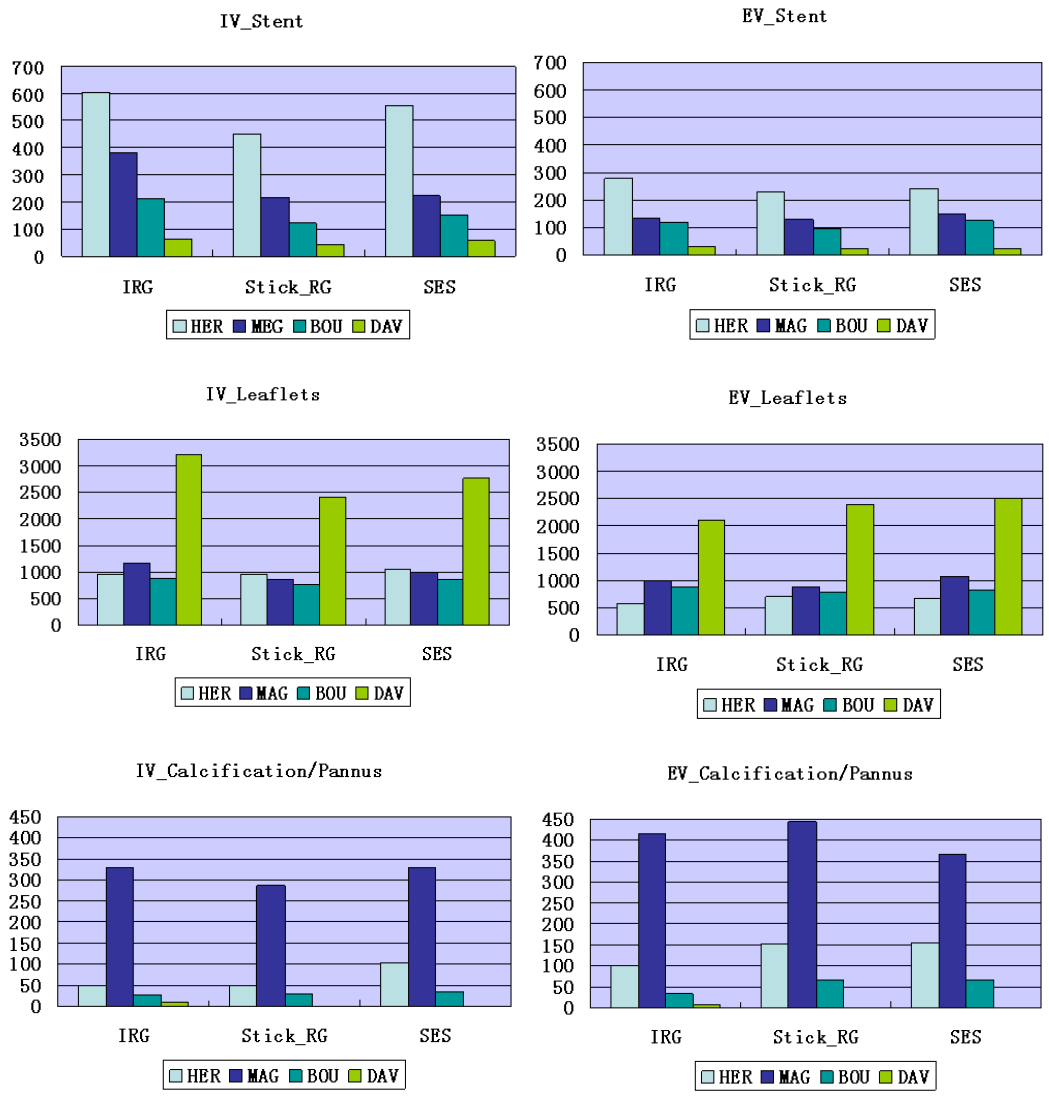

Fig 4.13: Volume analysis of bioprosthesis components

When we compare the results between in- vivo and ex-vivo for each method, the differences in volumes are generally less than 20%. Nevertheless, we can note that in the case HER, the in-vivo volumes are over-estimated for all the components, including stent, whereas the segmentation results were qualitatively (visually) considered better than those obtained in the other cases.

The over estimation of the volumes of the bioprosthesis components could be

corrected by considering the stent as a reference structure in in-vivo data. We just suggest here a possible way to perform such a correction. Thus, a volume correction ratio could be computed as follows:

$$K = V_{RS} / V_{IV-S}$$

where V_{RS} is the volume of the real stent, which could be known from stent manufacturer data, and V_{IV-S} is the volume of the segmented stent. The application of this correction ratio in case HER seems to reduce the differences between the in-vivo and ex-vivo volumes of leaflets (Fig. 4.14).

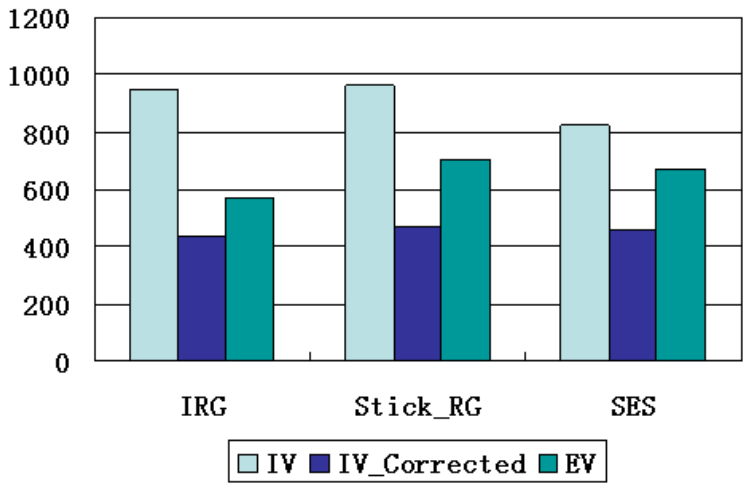

Fig 4.14: Stent based correction of leaflet volume in case HER.

4.4 DISCUSSION

We have tested three different methods for CT images segmentation of degenerated aortic bioprostheses. Considered methods, even if different in their approach, seem to be similar in terms of results. They are considered as semiautomatic segmentation methods.

The mean difference among these methods is that the Isotropic Region Growing method is performed using software for image analysis (3D Slicer), relatively easy to use, but needing heavy interaction by the user (manual selection of different seed points for the different components of the bioprosthesis). On the other hand, Stick Region Growing and Stick Exhaustive Search methods need, at this time, to be performed by means of specifically designed software tools, but their interactivity is lower. The reduced interactivity level results in some differences in terms of voxels volumes. It seems difficult to replace the user ability to recognize bioprosthesis different structures in CT transverse sections (IRG) by the automatic criteria based on CT density (Stick RG and SES).

Quantitative analysis shows these differences among the methods, but we can’t consider them significant because of the inability to perform a statistical analysis on few databases. Moreover, we don’t know at the moment if these small differences (generally less than 20%) could have a real interest for practical application. The aim of this study was first to assess the feasibility to

reconstruct leaflet morphology by preoperative CT images segmentation or/and visualization.

Additional comments have to be done concerning segmentations results. Among the analyzed datasets the best results have been obtained in the case of the pericardial bioprosthesis (Case #1 – HER). In this specific case the reason can be partially attributed to the thickness of the valve tissue. Pericardial leaflets are largely thicker than porcine with consequent better detection by CT. Results of all segmentation methods were satisfactory in this case and less interactive/more automatic methods based on stick segmentation should be considered and preferred for their efficacy.

The porcine bioprostheses (Case #2,#3,#4 – MAG, BOU, DAV) showed in general worst results. Porcine leaflets are quit thin and their thickness could be not the same along the leaflets because of their natural origin. The incomplete detection by CT results in leaflets defects in 3D reconstructions. In these cases interactive method allows manual adjustments to complete undetected leaflets and should be preferred.

Looking at quantitative analysis, there are different factors that could explain the volumes differences observed between in-vivo and ex-vivo reconstructions. Firstly, the image resolution is not the same. In-vivo acquisition protocol is represented by the standard protocol used for ECG gated coronary CT and specific acquisition for bioprosthesis analysis doesn’t exist at the moment. Concerning the ex-vivo images we chose a high resolution acquisition protocol

(temporal bone) to be as close as possible to reality and to use these images as reference. Other than image resolution, we can consider the presence of the heart motion and of blood superposition as important factor for volumes differences. To deal with this problem we propose a correction factor that could represent an interesting way to reduce the volume differences but need to be validate in larger series.

Computing of leaflets volumes can also be altered by the non-metallic part of bioprosthesis stent. Only the metallic stent can be used as spatial limitation for the leaflets because the non metallic part has the same density of the leaflets. For this reason leaflet volumes are higher than normal in the only case of bioprosthesis with incomplete metallic stent (Case #4 DAV). This problem can be translated to stentless bioprostheses analysis and need to be considered to avoid confusion in results.

Another point is that, in all studied cases, we observed in-vivo underestimation of leaflets degeneration. It should be said that, in these particular studied cases, leaflets are not severely calcified and most part of degeneration consists in leaflets thickening. These mild alterations of the leaflets don’t appear strongly dense such as calcifications and can be difficult to detect in in-vivo images. These results in a consequent underestimation of degeneracy compared to ex-vivo images, in which smaller differences in density can be easily appreciated.

REFERENCES

[4.1]. L.Pham D, Xu C, L.Prince J. A Survey of Current Methods in Medical Image Segmentation. Technical Report JHU/ECE 99-01, Johns Hopkins Univ., 1998.

[4.2]. Kass D. A., Chen C. H., Curry C., Talbot M., Berger R., Fetics B. and Nevo, E. Improved left ventricular mechanics from acute vdd pacing in patients with dilated cardiomyopathy and ventricular conduction delay. Circulation, 1999(12):1567–1573.

[4.3]. Falcão AX, Udupa JK, Miyazawa FK An ultra-fast usersteered image segmentation paradigm: live wire on the fly, IEEE Trans. on Medical imaging, 19:55-62

[4.4]. Mortensen E.N. and Barrett W. A., “Interactive segmentation with intelligent scissors,” Graphical Models Image Processing, vol. 60, no. 5, pp. 349–384, Sept. 1998.

[4.5]. Cormen T., Leiserson C., and Rivest R., Introduction to Algorithms. Cambridge, MA: MIT Press, 1991.

[4.6]. Vincent L., Soille P. Watersheds in Digital Spaces: An Efficient Algorithm Based on Immersion Simulations. IEEE TRANSACTIONS ON PATTERN ANALYSIS AND MACHINE INTELLIGENCE, 13(6):583-598, 1991.

[4.7]. Pohlman S., Powell K.A., Obuchowski N.A., Chilcote W.A., and Grundfest-Broniatowski S.. Quantitative classification of breast tumores in digitized mamograms. Medical Physics, 23:1337–1345, 1996.

[4.8]. Cheng J., Foo S.W., and Krishnan S.M. Watershed-Presegmented Snake for Boundary Detection and Tracking of Left Ventricle in Echocardiographic Images. Information Technology in Biomedicine, IEEE Transactions, April 2006:10(2) : 414 – 416.

[4.9]. Cheng J., Foo S.W., and Krishnan S.M. Watershed-Presegmented Snake for Boundary Detection and Tracking of Left Ventricle in Echocardiographic Images. Information Technology in Biomedicine, IEEE Transactions, April 2006:10(2) : 414 – 416.

[4.10]. Fleureau J, Garreau M, Boulmier D, and Hernandez A. 3D Multi-Object Segmentation of Cardiac SCT Imaging by using a Multi-Agent Approach. Conf Proc IEEE Eng Med Biol Soc. 2007; 1: 6003–6006.

[4.11]. Sahoo P.K., Soltani S., Wang A.K.C., and Chen Y.C. A Survey of Thresholding Techniques. Computer Vision, Graphics and Image Processing, 1988, 41:233-260.

[4.12]. Boskamp T., Rinck D., Link, F., Kummerlen B., Stamm G., Mildenberger P. New vessel analysis tool for morphometric quantification and visualization of vessels in CT and MRI imaging data sets. Radiographics, 2004 24(1) :287–297.

[4.13]. Adams R. and Bischof L. Seeded region growing, IEEE Trans. Pattern Anal. Machine Intell. 1994, 16: 641-647.

[4.14]. Fan J., Yau D.Y., Elmagarmid A.K., Aref WG. Automatic image segmentation by integrating color-edge extraction and seeded region growing. IEEE Trans Image Process. 2001;10(10):1454-66.

[4.15]. Osher S. and Sethian, J.A. Fronts propagating with curvaturedependent speed: algorithms based on Hamilton-Jacobi formulations, J. Comput. Phys., 79(1):12–49, 1988.

[4.16]. Osher S. and Fedkiw R. Level set methods and dynamic implicit surfaces, vol. 153 of Applied Mathematical Sciences, New York, 2003.

[4.17]. Duquette A.A., Jodoin P.M., Bouchot O., Lalande A.. 3D segmentation of abdominal aorta from CT-scan and MR images Computerized Medical Imaging and Graphics 36 (2012) 294 – 303

[4.18]. Udupa JK**,** Saha PK**,** Grevera GJ**,** Zhuge Y. Methodology for evaluating image-segmentation algorithms. *Proc. SPIE* 4684, Medical Imaging 2002: Image Processing, 266 (May 15, 2002)

[4.19]. Boykov Y, Funka-Lea G. Graph Cuts and Efficient N-D Image Segmentation, International Journal of Computer Vision November 2006, Volume 70, 2: 109-131

[4.20]. reiman M, Esses S, Joskowicz L, Sosna J. An iterative model-constraint graphcut algorithm for abdominal aortic aneurysm thrombus segmentation. In: International symposium on biomedical imaging. 2010. 672 – 675.

[4.21]. Frangi AF, Niessen WJ, Viergever MA. Three-dimensional modeling for functional analysis of cardiac images: A review. IEEE Trans on Medical Imaging. 2001;20(1):2–25.

[4.22]. McInerney T, Terzopoulos D. Deformable models in medical image analysis: A survey.

Medical Image Analysis. 1996;1(2)

[4.23]. Chen T, Metaxas DN, Axel L. 3D cardiac anatomy reconstruction using high resolution CT data. MICCAI. 2004;1:411–418.

[4.24]. Lorenzo-Valdes M, Sanchez-Ortiz GI, Elkinton AG, Mohiaddin RH, Rueckert D. Segmentation of 4D cardiac MR images using a probabilistic atlas and the EM algorithm. Medical Image Analysis. 2004;8(3):255–265.

[4.25]. Sermesant M, Forest C, Pennec X, Delingette H, Ayache N. Deformable biomechanical models: application to 4D cardiac image analysis. Medical Image Analysis. 2003;7(4):475–488.

[4.26]. Reuze, P., Coatrieux, J.-L., Luo, L., and Dillenseger, J.-L. A 3d moment based approach for blood vessel detection and quantification in mra. Technology and Health Care, 1993:1 :181–188.

[4.27]. Levoy M. Display of surfaces from volume data. Computer Graphics and Applications, IEEE May 8(3):29-37, 1988.

[4.28]. Boskamp T, Rinck D, Link, F, K¨ummerlen B, Stamm G, Mildenberger P.. New vessel analysis tool for morphometric quantification and visualization of vessels in ct and mr imaging data sets. Radiographics, 2004 24(1) :287–297.

[4.29]. Luo L. Surface normal of 3D object display in cuberille environment. Engineering in Medicine and Biology Society, 1988: 1: 420-421.

[4.30]. Ibáñez L. The ITK Software Guide –Second Edition November 21,2005.

V - VISUALIZATION

In addition to structural deterioration, an aortic bioprosthesis can have functional degradation and prosthesis dysfunction over time [5.1, 5.2]. Understanding the precise mechanism of bioprosthesis dysfunction would thus be important to direct clinical management. Multi detector CT images, thanks to their high spatial resolution, would potentially allow better visualization of the bioprosthetic valve leaflets after aortic valve replacement than echocardiography (TTE, TOE). Moreover, visualization could be used to complete the set of computer-vision tools required to improve the understanding of the failure mechanism and facilitate the medical decision about the therapeutic option. Thus, the visualization process could be considered both to overcome some difficulties encountered in the segmentation of MDCT images, and to fully render the information included in the 3D+T CT volume images to improve and accelerate the general understanding of vascular pathologies. The ultimate goal is to allow a more realistic preoperative planning of surgery/interventional procedure.

In the previous chapters, we considered standard visualization of valve structures from a single phase, *i.e.* during the diastole, in the 3D+T cardiac data set. The input of the visualization process was provided by the output of the segmentation process.

In this chapter, we reconsider the issue of visualizing 3D+T data sets acquired

at different phases of the cardiac cycle. The underlying assumption is that, according to the visualization technique used, the contribution of pre-processing / segmentation can be more or less critical to provide the user with information to better interpret the motion of valve leaflets.

In the following we first summarize the main techniques of visualization in medical imaging, by considering both rendering and camera positioning issues, including virtual navigation (endoscopy). We then describe the method proposed to visualize 3D+T CT volumes, by considering pre-processing and rendering issues as well as motion compensation required to control, during the cardiac cycle, the positioning of the virtual camera within the moving aortic root. We then report preliminary results. Although our work was mainly dedicated to aortic valve bioprothesis, we also report first results obtained on native valve to illustrate the interest of the proposed methodology.

5.1 STATE OF THE ART

Visualizing techniques have had a great development in the last years. They allow exploring pre-operative volumes in order to detect and understand abnormal features and further to assist the physician in prior planning of intra-operative interventions.

In this section, we present the techniques which could be used in order to design a tool to explore aortic valve leaflets motion. They mainly deal with visual rendering and virtual camera positioning.

5.1.1 Rendering

Visual rendering is generally defined as the process of generating an image from a model or from a description of a scene. The model or the description of the scene can be obtained from a volume data set [5.3].

Visual rendering techniques have been commonly used to visualize medical data, such as cardiac MSCT data. For instance, they have been used to understand the vascular structures [5.4, 5.5].

In the field of aortic valves, although recent works, dealing with the issue of computer assistance to transcatheter aortic valve implantation (to treat native valve stenosis), have been presented [5.6, 5.7], they do not address specifically the visualization issue. To our knowledge, visualization techniques dealing with aortic valve (both native and bioprosthesis) specifically were not

reported.

Two classes of visual rendering techniques have been widely used in medical image visualization: surface rendering and volume rendering.

Surface rendering (as we introduced in section 4.1.7) relies on a previous binarization, or segmentation, of the structures of the objects of interest and the tessellation of the surface initially described by sparse or dense 3D point sets.

The quality of surface rendering is depending on the segmentation results. From the previous results (section 4.3), we observed some defaults in the visualization obtained with surface rendering due to the imperfection of the segmentation. This tends to show that surface rendering may not be the most suitable technique for visualizing the 3D + T data sets.

Volume rendering does not demand a previous binarization of the images. It provides the ability to display either surface, volume values or both. In this case spatial circumscription (plane cutting for example), set operations (union, intersection, difference) and multistructure transparency effects can be easily done.

5.1.1.1 Ray Tracing

In computer graphics, ray tracing [5.8-5.10] is well known. This scheme requires assignment of classification coefficients (opacity values) to each voxel. Geometric rays (view rays) are traced from the virtual camera to explore the volume along the ray direction. This approach combined with the radiosity, i.e. color, transparency, refractivity and reflectivity (defined by a transfer function), of each voxel of the volume data set allows the rendering to be more accurate (Fig 5.1).

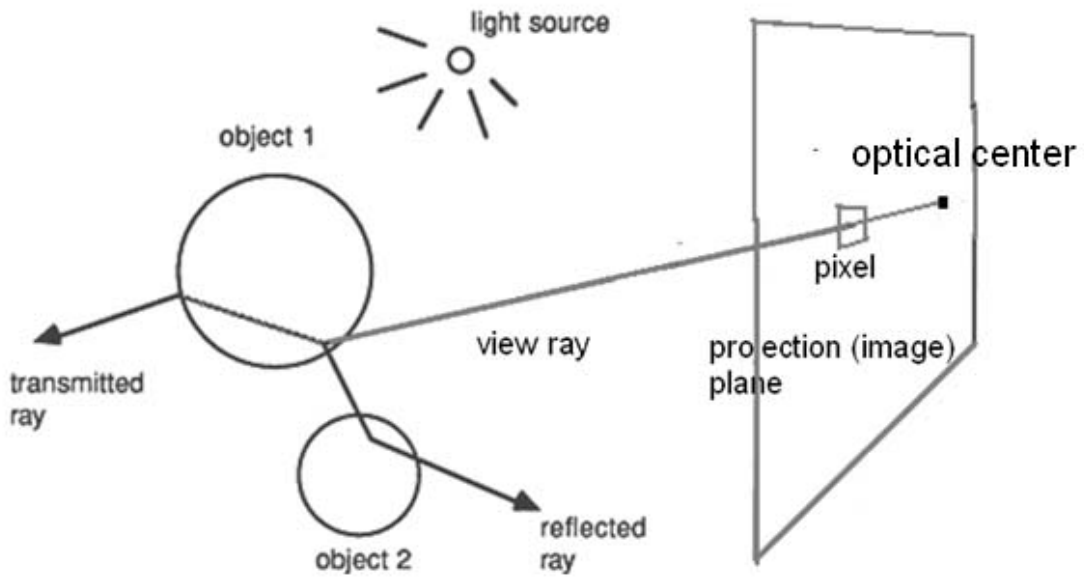

Fig 5.1: Volume rendering by ray tracing model.

The main limitation of this kind of algorithms is that they can involve the computation of multiple rays to deal with light refraction and reflection, especially in case of shadow. Noise and artifacts may influence its

performance by causing complex light paths.

5.1.1.2 Maximum intensity projection（MIP）

In the MIP algorithm, the highest-attenuation voxels along lines projected through the volume data set are selected [5.11]. The subset of these high-attenuation voxels from the volume is then incorporated into a 2D image.

MIP is a widely used rendering tool and has proved particularly useful for evaluation and display in CT angiography [5.11, 5.12], especially for the visualization of coronaries [5.13].

However, there are two main limitations of the technique: (i) the evaluation of the vascular structures of interest may be obstructed by the presence of external high-attenuation voxels, and (ii) the 3D relationships among the structures are not visible in the display [5.14].

5.1.1.3 Direct Volume Rendering

The Direct Volume Rendering (DVR) technique is a very common tool in the analysis of volumetric data [5.3]. Transfer Functions (TFs) are used to map intensities in the CT data with color and opacity.

Volume ray casting [5.3, 5.4, 5.13, 5.15, and 5.16] is one of most common used DVR techniques. The idea of ray casting is very similar as ray tracing. Rays are determined by the optical center of virtual camera and the pixel on

the projection plane. The values of voxels (transferred by TFs) along the rays are sampled and combined to define the value of the pixels.

In ray casting, refraction and reflection are not considered. This reduces the computation complexity.

DVR techniques are commonly used to visualize the CTA data [5.17]. For this, with efficiency being a dominant problem in the clinical workflow [5.18, 5.19], clinical tools commonly provide predefined TFs (presets) for CTA.

Researchers did many works on TFs designing. Common tools are based on local neighborhood analysis. Objects can also be described on a higher abstraction level by shape, size and connectivity.

For the visualization of medical data, it is advantageous to use domain knowledge in the TF design. Additional information can be encoded when different TFs are considered, depending on the tissues they are meant to visualize. One example is to take into account the spatial relations between tissues in order to distinguish different kinds of structures appearing with the same density [5.19， 5.20]. The works presented share a similar approach. In the TFs, vessels are treated differently than other tissues. To our knowledge, this kind of approach has not been yet tested and reported in the context of aortic valve structures visualization.

5.1.2 Camera positioning

The virtual camera, which is defined in visual rendering, could be similar to an optical device (*e.g.* endoscopy). Its position, orientation and displacement have to be controlled to display the scene from a suitable point of view. Virtual navigation allows exploring pre-operative volumes in order to detect and characterize abnormal features and further to assist the physician in prior planning of intra-operative interventions [5.21].

In navigation systems, virtual camera positioning (path planning) is mainly based on vascular centerline extraction. A lot of studies have been devoted to the extraction of vascular centerline of arteries in CT data [5.22]. These methods are based on direct centerline tracking [5.23], model-based approaches [5.24, 5.25], minimum cost path techniques [5.26, 5.27], or mathematical morphology (thinning algorithm) [5.28-5.30].

In this work, we are concerned with the issue of visualization of structures observed at different phases of the cardiac cycle, i.e. sampled at different times in the 3D+T CT data set. In order to get a satisfactory exploration of the motion of some sub-structures, such as valve leaflets, the compensation of the main structure motion (bioprosthesis, native valve) has to be considered. The pose parameters of the virtual camera (position, direction, and rotation around optical axis) have to be controlled to keep the virtual camera in a static position relatively to the aortic valve.

Motion compensation requires spatial references to control the camera.

Unfortunately, the model of aortic valve motion is difficult to establish for a given patient [5.6]. Motion compensation for virtual navigation in aortic valve structures, observed through 3D+T cardiac CT data sets, is an open issue (both for bioprosthesis and native valve).

5.2 METHODS

In previous chapters, we designed and discussed different methods of preprocessing and segmentation. We improved the SNR with preprocessing algorithms, and obtained segmentations of aortic valve bioprosthesis. These results can be visualized to understand the underlying and relevant information from the CT data sets: the calcification severity, the position of calcifications.

From the 3D+T data sets, we can get a set of rendering from volumes reconstructed at different times of the heart beat. To allow the user to interpret easily the visualization of these data, and to understand and analyze the motion of the structures of interest only (i.e. the leaflets), the virtual camera pose has to be slaved to the valve movement. This motion compensation may depend on stent, aortic center line, or tricuspid annulus.

Assuming the different MSCT volumes have been preprocessed, the overall approach (Fig 5.2) proposed to visualize aortic valve leaflets (bioprosthesis or native valve), is composed of: (a) Motion artifacts correction and grey level normalization, (b) Transfer functions designing for direct volume rendering, and (c) Motion compensation, mainly depending on stent (bioprosthesis) and tricuspid annulus (native valve).

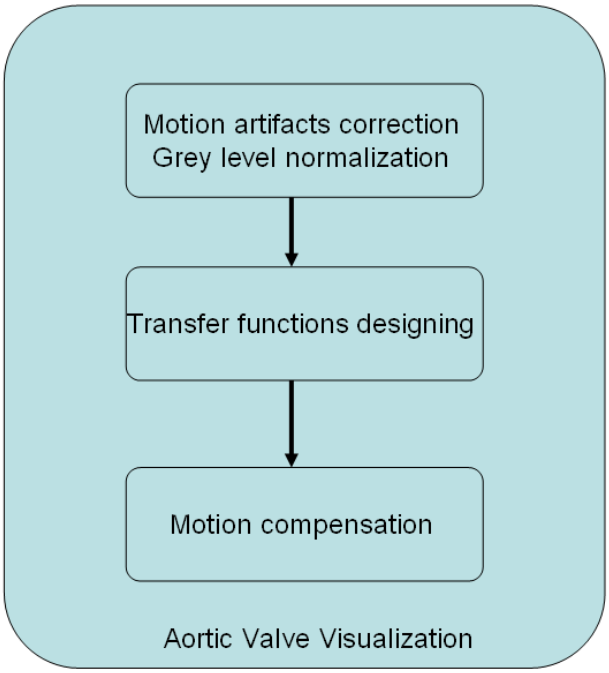

Fig 5.2 : Aortic valve visualization.

The output of the proposed visualization process is a virtual video showing the motion of aortic valve leaflets, like the video output we could get with trans-blood angioscopy in the aortic root (note that this technique is not yet available). This might contribute to the better understanding of valve dysfunction.

5.2.1 Motion Correction and Grey Level Normalization

In chapter IV, we only analyzed the volume sampled at a single phase during the diastole. In fact, due to the limitation we discussed in section 3.1, the quality of the volumes at the different phases of the cardiac cycle may be altered in different ways.

Typically, 8-10 volumes (marked as volume V_i) are reconstructed at different phases (marked as phase P_i) of the cardiac cycle. As we mentioned in section 2.4.1.2 (MSCT gating), phases are not evenly distributed in the cardiac cycle. 3-4 volumes are reconstructed during systole, with leaflets opened, while 5-6 volumes are reconstructed during diastole, with leaflets closed.

The motion artifacts, especially in phases with important motion of the leaflets, may drive to structural inconsistencies and to hardly interpretable visualization. For a same structure, the deviation of the grey levels between the different cardiac phases may also distort the visualization of the CT data sets. Fig 5.3 shows some motion artifacts, due to the gating time during systole, observed in cardiac 3D+T CT images.

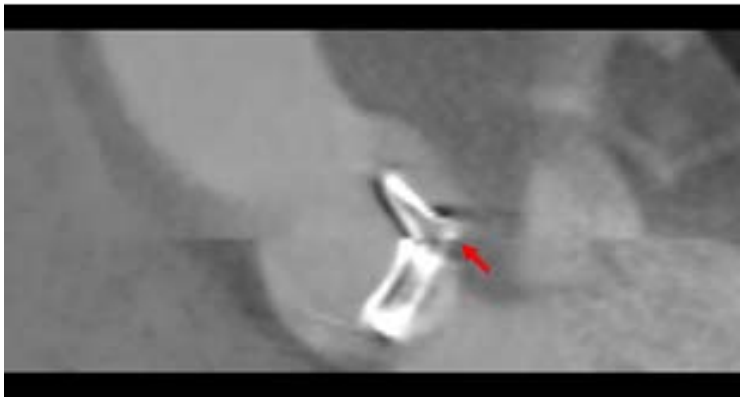

Fig 5.3: Motion artifact between slices during systole.

In our data sets, motion artifacts appear during systole as sudden shifts of slices. The correlation between consecutive slices could be used to correct these artifacts. We used Normalized Correlation Coefficient (NCC) between the two consecutive slices located on the different sides of the artifact to

correct the images.

NCC is defined as [5.31]:

$$NCC_{i,j} = \frac{\sum_{u,v}(I_1(u,v)-\overline{I_1})(I_2(u,v)-\overline{I_2})}{\sqrt{\sum_{u,v}(I_1(u,v)-\overline{I_1})^2 \sum_{i,j}(I_2(u,v)-\overline{I_2})^2}}$$

(5.1)

where $I_1(u,v), I_2(u,v)$ are the intensities of voxels in the overlapping areas of the first and second slice located at i, j, and $\overline{I_1}$ and $\overline{I_2}$ are the mean grey levels of the overlapping areas, respectively. The NCC measure depends on the overlap between slices. We compute NCCs for $i_0 < i < i_1, j_0 < j < j_1$ where i_0, i_1, j_0, j_1 define the range of the shift. The (i, j) with maximum NCC value is used to correct the motion artifacts.

In some conditions, the presence of the stent (as illustrated by Fig 5.4) can cause some correction errors, especially in the region of the leaflets. In such case, we did not consider the voxels located in the stent to estimate the correction.

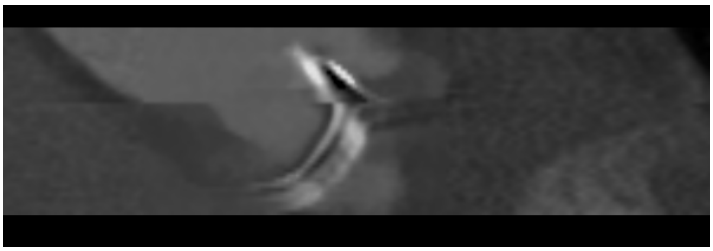

Fig 5.4: Different motion artifacts on stent and vascular lumen.

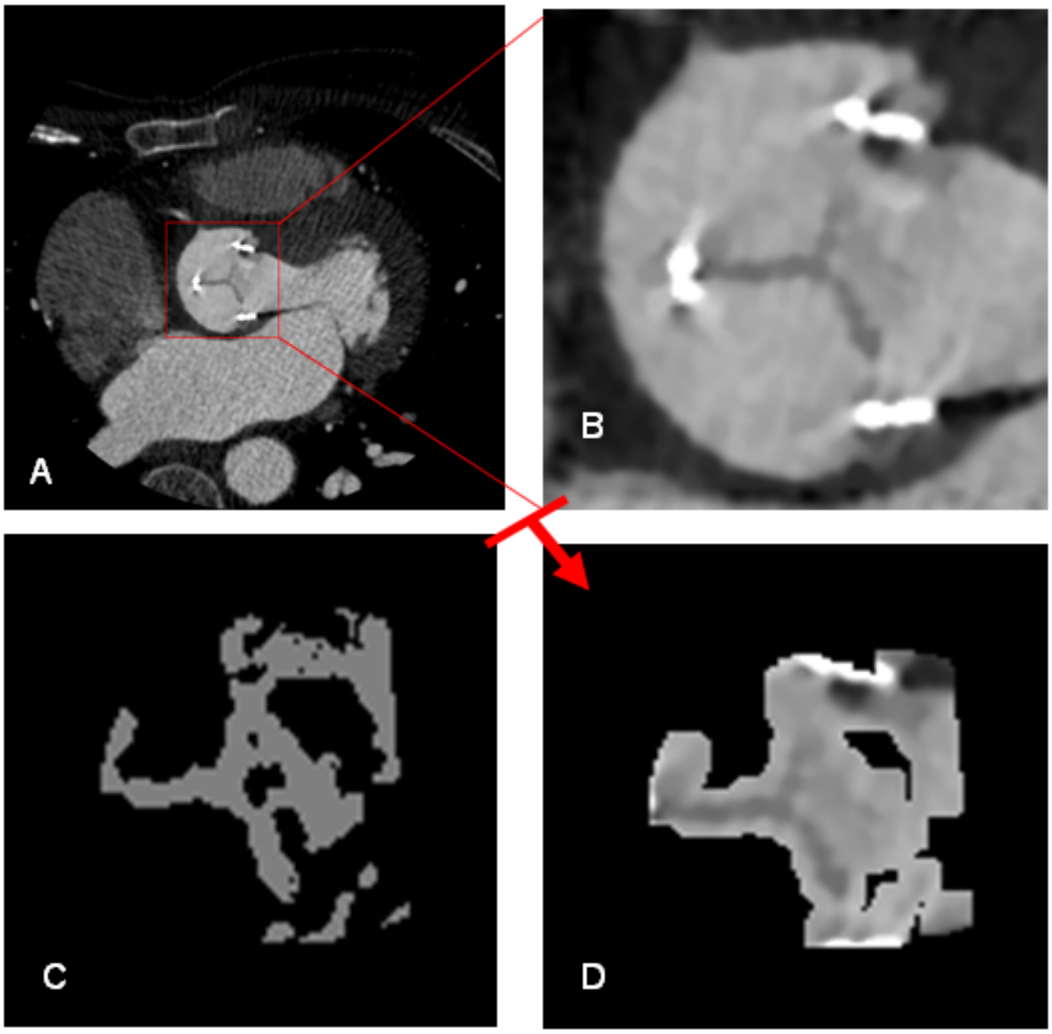

Fig 5.5: CT slice after preprocessing (A) and the region of interest including aortic valve (B). By dilating the region of voxels classified as leaflets (C), we get a region including leaflets (D).

Visual rendering has to preserve the consistency of the representation of a same object between the different phases. Unfortunately, the concentration of contrast agent in the vascular structures varies along time. Grey levels of voxels located in a same structure are different from each others for volume images acquired at different phases.

To correct time-variation of voxel values we first define a sub-region SR close to the leaflets (Fig 5.5). This region SR is obtained by dilating the region of

voxels classified as leaflets in the pre-processing step. Typically, we dilate the region with a spherical structuring element of 3 voxels radius. We find the range of grey level of tissues located inside the sub-region for each volume. The maximum and minimum grey level values are used to normalize voxels values. For each volume we compute the normalized grey level I_0 as follows:

$$I_0 = \frac{(I_n - I_{mn})(I_{M0} - I_{m0})}{I_{Mn} - I_{mn}} + I_{m0} \qquad (5.2)$$

I_n is the grey level of the considered voxel in the volume V_n. I_{mn} and I_{Mn} are the minimum and maximum grey level values of structures in volume V_n.

5.2.2 Rendering

We use volume ray casting, which is more suitable than MIP and ray tracing, for visualizing the prosthesis and native valve. Fig 5.6 shows the result of a preliminary test preformed on valve bioprothesis data by using common volume ray casting model. It is difficult to understand the morphology of the bioprosthesis. To improve visualization TFs have to be defined specifically for aortic valve.

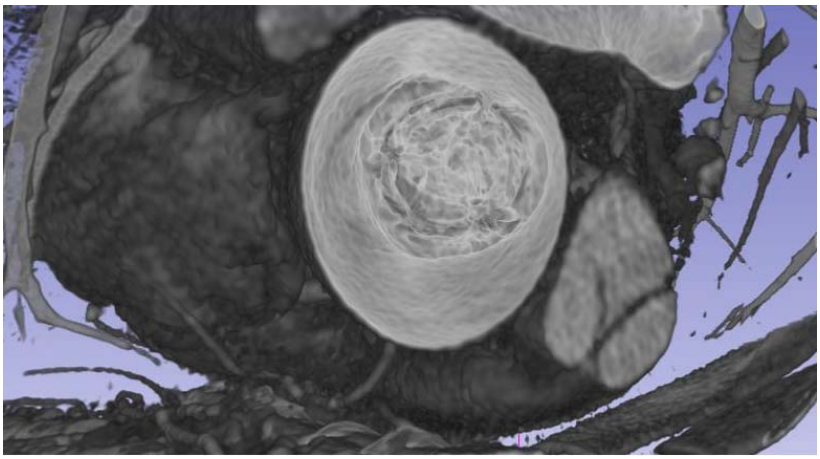

Fig 5.6: Standard volume rendering of aortic valve bioprothesis.

At first, we use the result of classification (section 3.4.2.2) to characterize the distributions of gray level values in the different structures (leaflets, vascular lumen, calcification and stent). Transfer functions (TFs) are designed based on this gray level features.

Transfer function for bioprosthesis is designed as:

- $f(x,y,z)=0$ when the voxel is located in the region classified as vascular lumen.
- $f(x,y,z)=1$ when the voxel is located in a region classified as stent, *i.e*. when $I(x,y,z) \gg I_{\max C}$ where $I_{\max C}$ is the maximum value of grey levels of calcification.
- $f(x,y,z)=k_C * (\frac{I(x,y,z)-I_{\min C}}{I_{midC}-I_{\min C}})^{0.5}$ when $I_{\min C} \le I(x,y,z) \le I_{midC}$ where $I_{\min C}$ is the minimum value and I_{midC} is the median value of grey levels for voxels located in region classified as other structures (which include calcifications). k_C is the coefficient which determines the transparency of calcification. Typically, $k_C = 0.5$.

- $f(x,y,z) = k_C * (\frac{I_{\max C} - I(x,y,z)}{I_{\max C} - I_{midC}})^{0.5}$ when $I_{midC} \le I(x,y,z) \le I_{\min C}$ where $I_{\max C}$ is the maximum value of grey levels for voxels located in region classified as other structures (which include calcifications). In some cases, motion artifacts of stent, which have similar gray level as calcification, might be rendered with this TF.
- $f(x,y,z) = k_L * (\frac{I(x,y,z) - I_m}{I_{mid} - I_m})^{0.5}$ when $I_m \le I(x,y,z) \le I_{mid}$ where I_m is the minimum value of grey levels and I_{mid} is the median value of grey levels for voxels located in region classified as leaflet. k_L is the coefficient which determines the transparency of leaflets. Typically, $k_L = 0.25$.
- $f(x,y,z) = k_L * (\frac{I_{mid} - I(x,y,z)}{I_M - I_{mid}})^{0.5}$ when $I_{mid} \le I(x,y,z) \le I_M$ where I_M is the maximum value of grey levels for voxels located in region classified as leaflet. Some tissues located outside the region of interest, such as vascular wall, are classified in the way.

Compared to surface rendering of segmented structures, for which some information can be lost, volume rendering with transparency may improve the general understanding of valve leaflets. We use different colors to render the different structures, *i.e.* leaflets, calcification and stent. Fig 5.7 shows TFs used in a case of bioprosthesis, and the result of volume rendering of bioprosthesis. In the case of native valve, the same transfer functions have defined to visualize the structures. Because there is no stent in such case, the TF for stent is not required.

The TFs used in the case of native valve and the result of volume rendering are shown in Fig 5.8. Because of the thickness of native valve leaflets, the transparency is less noticeable than in the case of bioprosthesis.

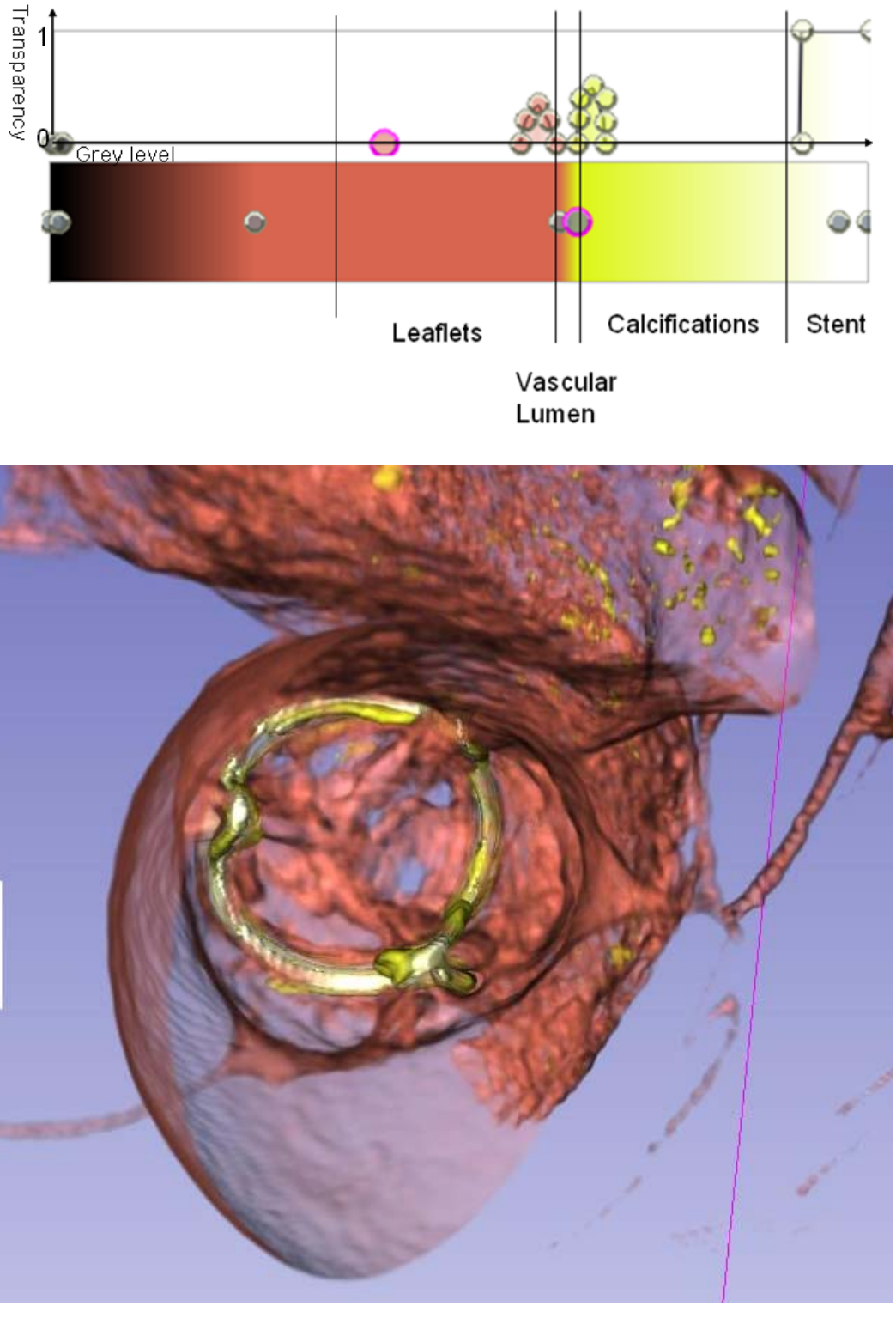

Fig 5.7: TFs used in a case of bioprosthesis and the result of volume rendering.

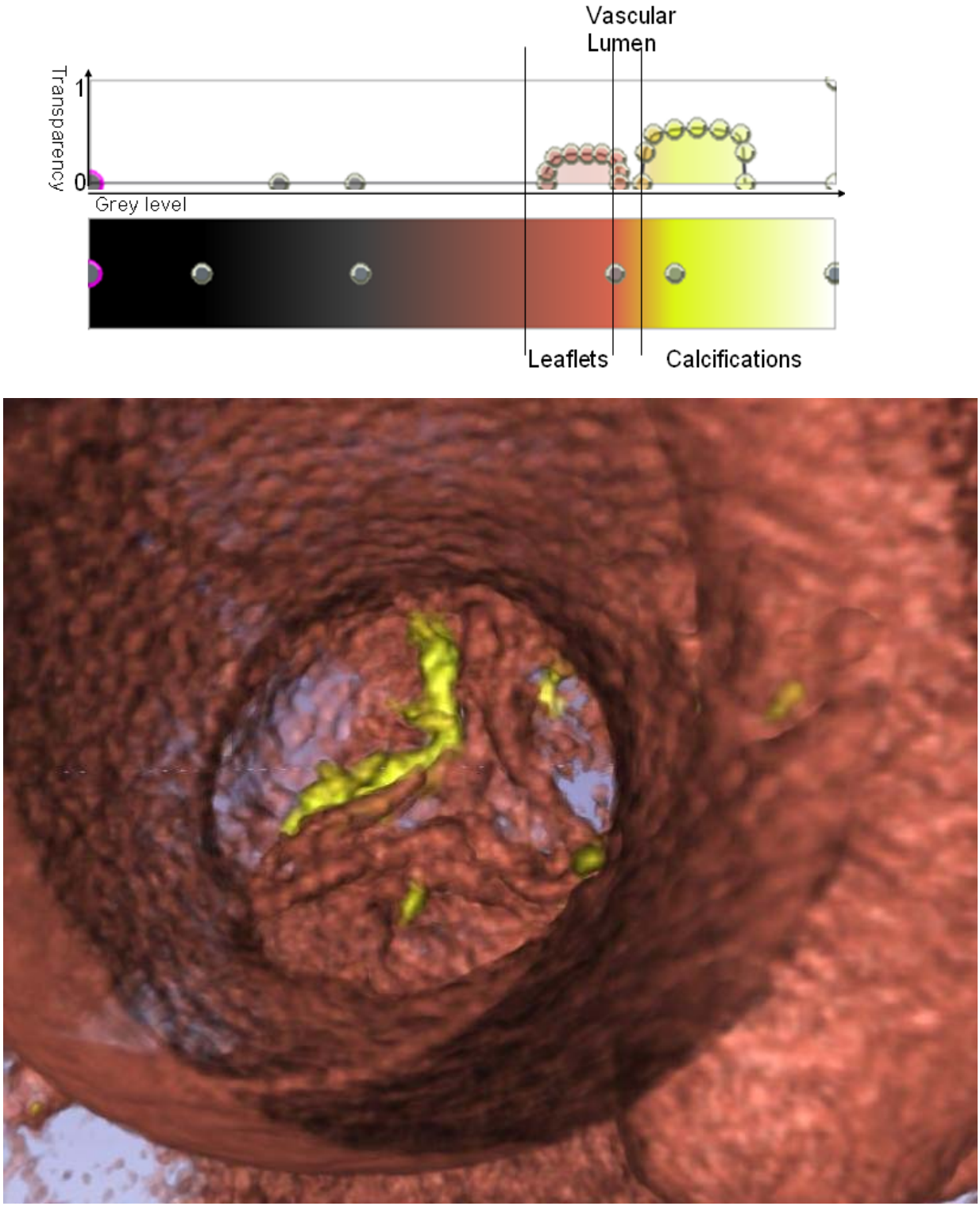

Fig 5.8: TFs used in a case of native valve and the result of volume rendering.

5.2.3 Motion Compensation

We describe the motion compensation to visualize 3D+T CT volumes. During the cardiac cycle, the virtual camera should be within the moving aortic root. Due to the short axial length of the ascending aorta, its centerline in the region close to aortic valve has a great curvature. This may give wrong pose of the virtual camera. We need to consider other reference objects to compensate the motion.

We used aortic centerline, coronaries and stent (bioprosthesis)/ tricuspid annulus (native valve) to fix the parameters determining the pose of the virtual camera.

In the case of bioprosthesis, we assume that the stent, either with complete metal or incomplete metal structure, is not deformed by the heart beat. It bounds (includes) the valve leaflets, which have their own motion. We consider it as a good reference object. The coronary ostia can also be used to define the distance between virtual camera and valve.

For the bioprosthesis with complete metal stent, we can detect the center O of the circular structure of the stent and vector D orthogonal to the circular structure plane (Fig 5.9). This vector D can be used as the viewing direction of the virtual camera. Using the vector D and the start points of the 2 coronaries (marked interactively), we can define the position of the camera.

We define the position P of the projection (or image) plane along D. This plane is located at equal distance to the two coronary ostia. The position of the

optical center C of the camera is defined along D. The focal length of the virtual camera (distance between C and P) is determined by the length PO. The rotation of the virtual camera around its optical axis is fixed by considering the coronary ostia.

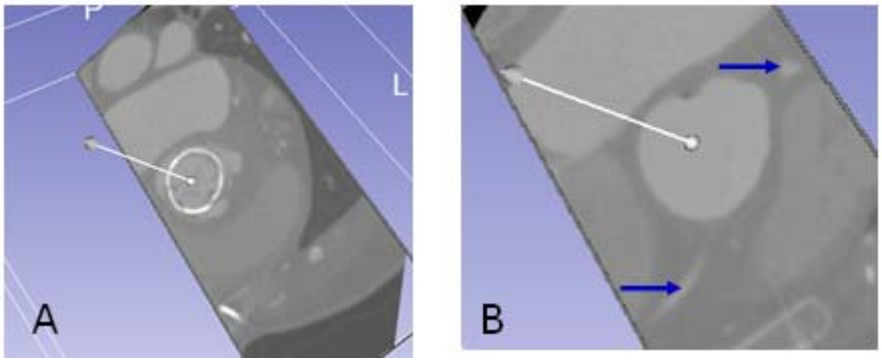

Fig 5.9: The direction orthogonal to the complete metal stent plane (A) and the position of virtual camera (B). Coronaries are marked by blue arrows.

For the bioprosthesis with incomplete metal stent, we can use the 3 metal points (top of stent) to compute the vector D and then the position and rotation of the virtual camera (Fig 5.10).

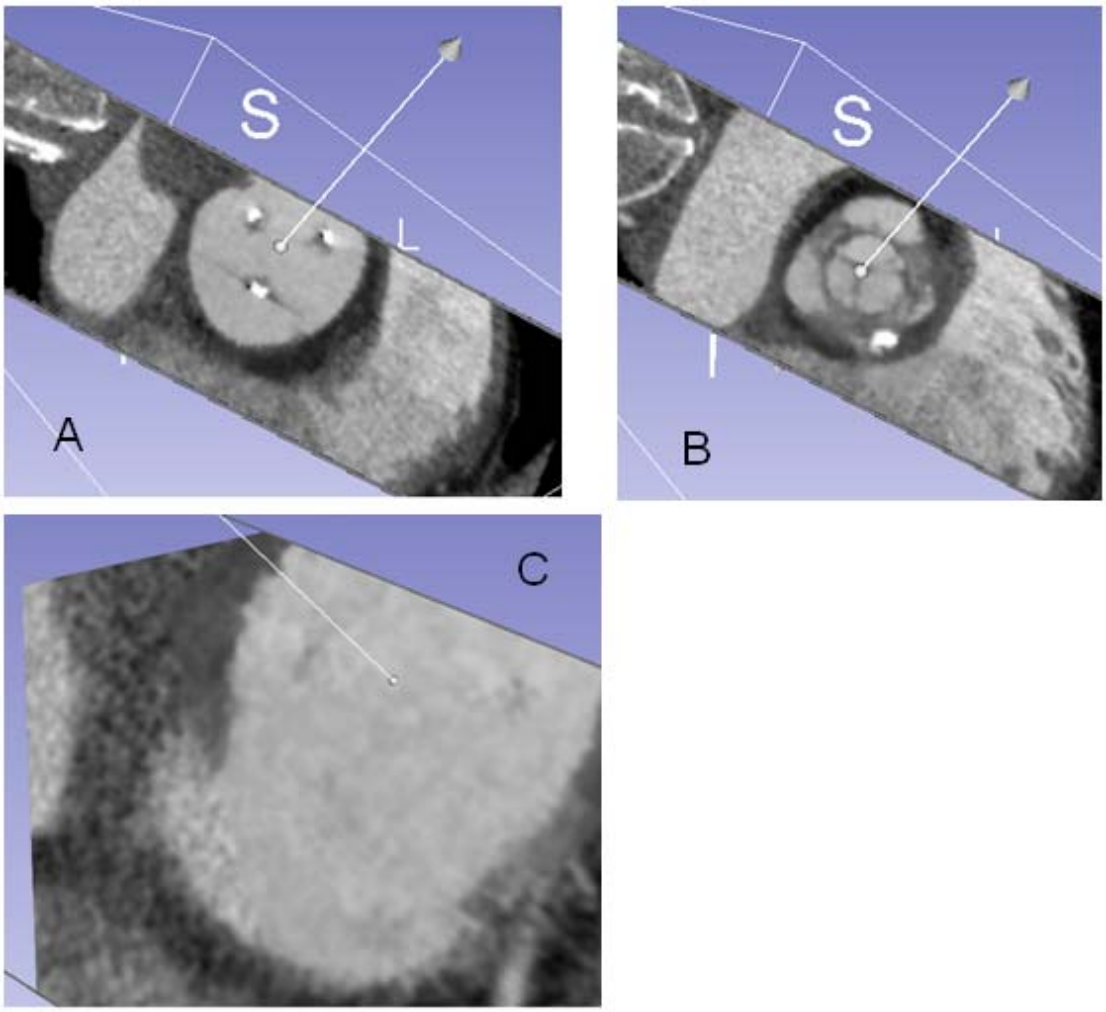

Fig 5.10: Direction defined by metal parts of incomplete metal stent (A), which is actually directed towards the center of the valve prosthesis (B), and the position of the camera (C).

If the motion artifacts of the metal stent are too serious, the positions and directions given by stent might be erroneous. In this case, the aortic centerline is used to help determining the pose of the virtual camera.

The determination of the aortic centerline was obtained by a method based on the computation of a distance map [5.32] from the binary volume of the ascending aorta. The segmentation process was based on the methods presented in section 4.2.

We extract the centerlines in the current volume V_n. We assume the previous

volume V_{n-1} has been processed and that the pose of the virtual camera has been determined as described above.

In V_{n-1}, we find the intersection K_{n-1} of the centerline and the camera image plane, and compute the vector KP_{n-1} determined by K_{n-1} and P_{n-1}. We count voxels, along centerline in V_{n-1}, between K_{n-1} and the leaflet. This value is used to locate K_n in V_n (Fig 5.11).

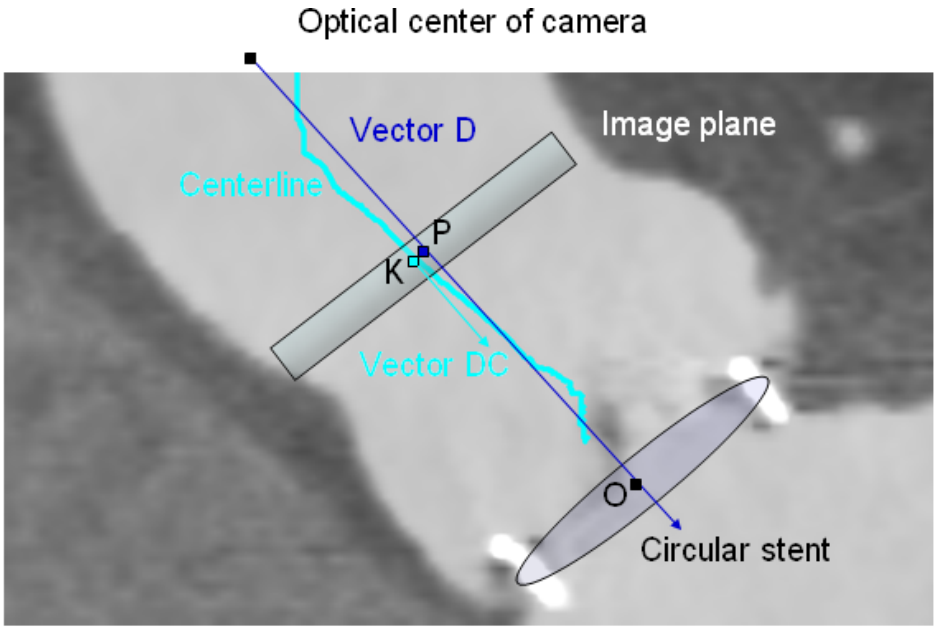

Fig 5.11: Pose of the virtual camera and the centerline.

We compare the direction vectors DC_n and DC_{n-1} of centerlines at K_n and K_{n-1}. DC_n and DC_{n-1} define an angle α and DC_n, DC_{n-1} and K_n define an axis A. K_n belongs to axis A and A is orthogonal to DC_n and DC_{n-1}. A rotation R of angle α around an axis A is thus determined.

Direction vector of the virtual camera D_n in current volume is obtained by applying to D_{n-1} the rotation R.

The direction of KP_n is obtained by applying to KP_{n-1} the rotation R. Its length is determined by value of KP_{n-1} and distances between coronary ostia do_n and do_{n-1}:

$$\|KP_n\| = \|KP_{n-1}\| \cdot \frac{do_n}{do_{n-1}}$$

Then we can determine the position of projection plane P_n.

$$P_n = K_n + KP_n$$

The rotation and focal length of the virtual camera are determined with the same process as in V_{n-1}.

The rotation and focal length of the virtual camera are determined by the coronary ostia as described previously.

In the case of native valve, there is not a reference object such as the stent in the bioprosthesis. Tricuspid annulus can be used in motion compensation in this case, as stent is used in bioprosthesis. It appears as a circular and continuous structure attached to the aortic valve leaflets. Unfortunately, tricuspid annulus can not be distinguished easily from surrounding structures in MSCT data. We had to mark it interactively (Fig 5.12 A – C). The tricuspid annulus is not an exact circle, like stent of bioprosthesis. We selected 2 groups of points (3 points at the top of commissure of leaflets, and 3 points at the bottom of leaflet, shown in Fig 5.12 A and C) to define the vector D. Other parameters are determined with the same process as in the case of bioprosthesis (Fig 5.12, D and E).

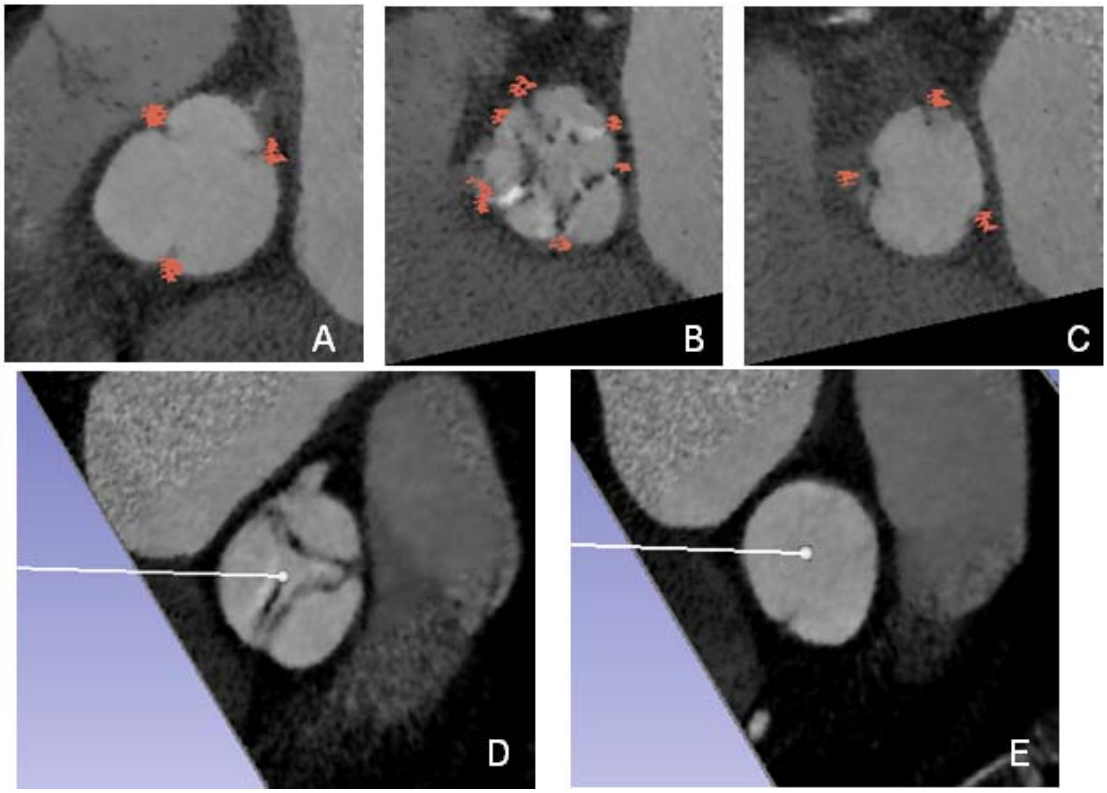

Fig 5.12: Voxels located in tricuspid annulus (A -C). Points at the top of commissure of leaflets (A) and at the bottom of leaflet determine the direction orthogonal to tricuspid annulus (D) and the position of virtual camera (E).

5.3 RESULTS

In this section we report the visualization results obtained with 2 MSCT patient data sets, one with bioprothesis and one with native valve. The main image parameters are summarized in Tab. 5.1.

Tab. 5.1 Image resolution parameters of MSCT data sets

Patient	Type of valve	Volume size(voxels in X,Y,Z)	Volumes reconstructed	Volume sampling (mm in X,Y,Z)
HER	Bioprosthesis	512,512,181	10	0.3125,0.3125.0.625
YVE	Native	512,512,212	8	0.344,0.344,0.625

In the following, we present the 3D visualization with volume rendering by considering all the volumes in the 3D+T data sets.

The first example is reported in the case 1 of the pericardial bioprosthesis (HER). Volumes V_1-V_4 are reconstructed during systole phases and volumes V_5-V_{10} are reconstructed during diastole phases.

Although the image quality is not as good as in the data set we used in section 4.3, volume rendering and motion compensation give satisfactory results, denoted as R_1 - R_{10} (Fig. 5.13). Nevertheless, the visualization does not provide a complete description of the structures when the magnitude of the leaflets motion is high (volumes V_2-V_4). We can see a commissure lost and good leaflets cooptation in diastole volumes, as this has been already observed from segmentation result in section 4.3. Furthermore, here, we can

see the commissure lost can alter the perception of leaflets opening in systole volumes (R_2).

Calcifications (yellow structures) can also be observed in renderings of V_7-V_9. In volumes with motion artifacts of stent (V_2-V_6, V_{10}), artifacts (yellow structures near white stent) with densities close to calcifications might influence understanding of leaflets.

As comparison, we show the results of volume rendering obtained with no gray level normalization and with a rough motion compensation process (R_{1bis} – R_{10bis}). For every volume (V_1-V_{10}) in the original data-set, a sub-volume of predefined size and bounding the valve (stent) has been extracted interactively. Parameters of volume ray casting and camera poses are determined from the sub-volume V_8, which was used for segmentation and volumetric analysis in chapter IV. In R_{1bis}, R_{6bis} and R_{10bis}, leaflets are more transparent. Some drift of virtual camera pose can be observed in R_{3bis}, R_{4bis}, R_{9bis} and R_{10bis}.

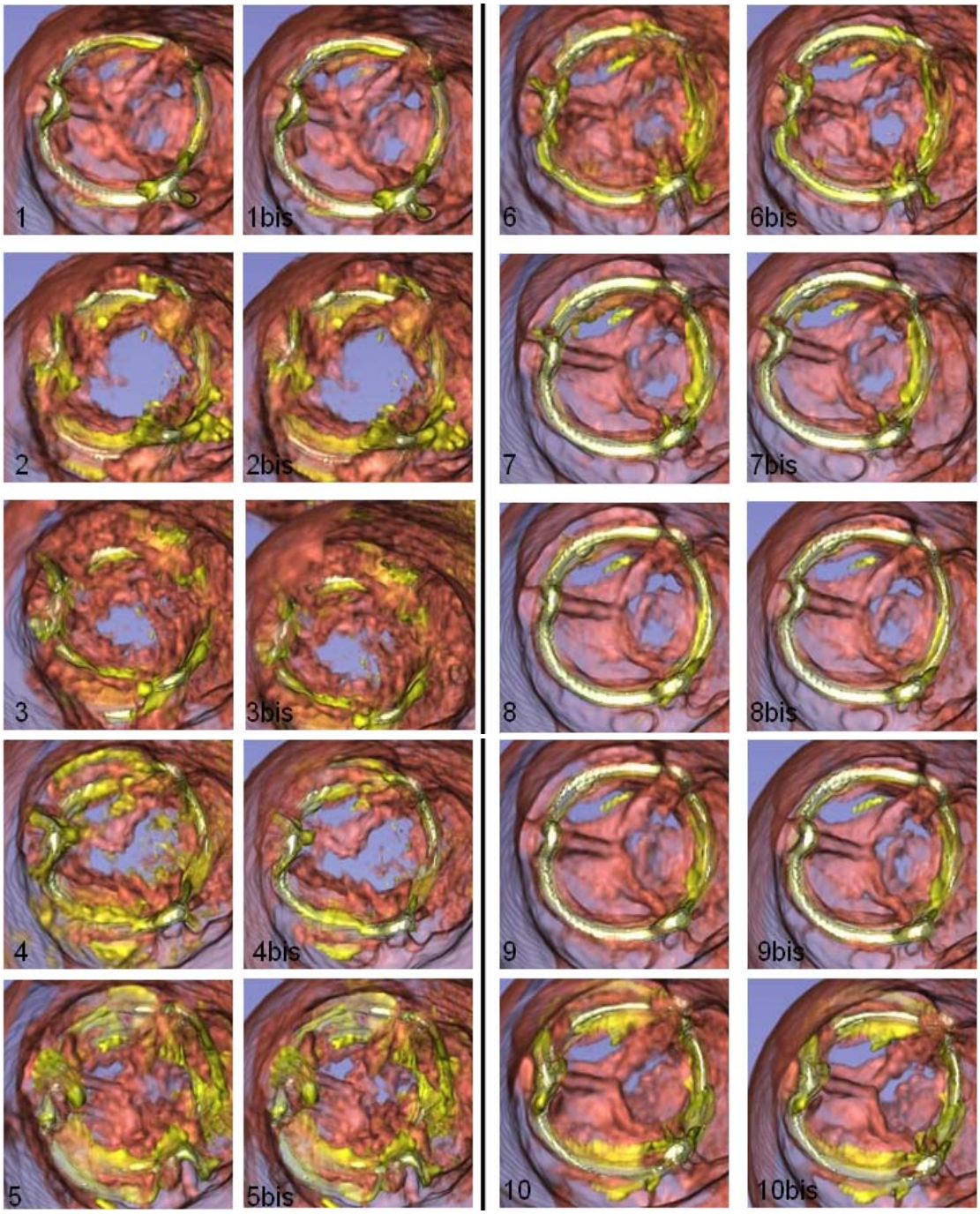

Fig 5.13: Visualization of the 3D+T data set in HER case: 4 systole volumes (R_1 - R_4) and 6 diastole volumes (R_5 – R_{10}). The commissure lost and the good leaflets cooptation can be seen in rendering. Visualization results obtained without gray level normalization and with rough motion compensation (R_{1bis} – R_{10bis}).

The second example illustrates the results obtained with a native valve (Fig 5.14). Volumes V_1-V_3 are reconstructed during systole phases and volumes V_4-V_8 are reconstructed during diastole phases. Thanks to the thickness of native valve leaflets, the gray level values of voxels located inside the leaflets are much darker than in the case of bioprosthesis. In the virtual images the transparency of the leaflets is much lower than in the case of HER. We can clearly observe different kinds of structures including valve leaflets, calcifications as well as vessel wall. These preliminary results show that the proposed method could also be applied to visualize native valve 3D+T CT data.

The motion of leaflet seems to be altered in the temporal sequence of virtual images (R_1-R_8). It is coherent with the development of calcifications on the leaflets (yellow structures).

As comparison, we show the results of volume rendering obtained with no gray level normalization and with a rough motion compensation process (R_{1bis} – R_{8bis}). For every volume (V_1-V_8) in the original data-set, a sub-volume of predefined size and bounding the valve annulus has been extracted interactively. Parameters of volume ray casting and camera poses are determined from the sub-volume V_7.

Thanks to the thickness of native valve leaflets, there are much less differences, *i.e.* transparency voxels located in leaflets, between visual renderings performed with and without gray level normalization.

Some drift of the virtual camera pose can be observed in R_{1bis}, R_{5bis}, and R_{8bis}.

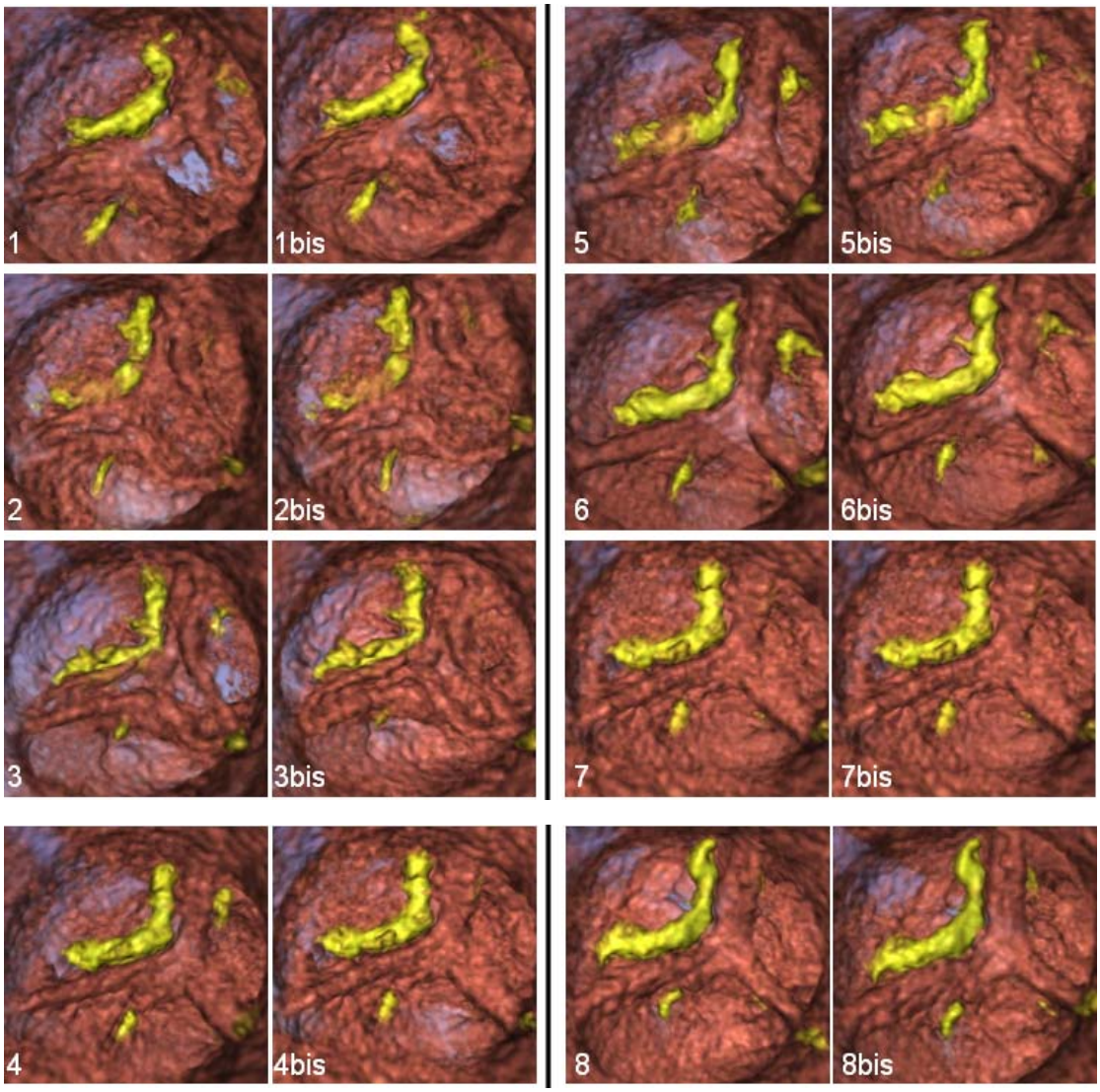

Fig 5.14: Visualization of the phases in YVE data set: 3 systole volumes (1-3) and 5 diastole volumes (4-8). The motion of one leaflet is altered due to calcifications on it. R_{1bis} – R_{8bis} without motion compensation and gray level normalization are comparison group.

In both cases (bioprosthesis, native valve), we observed that leaflets were not fully displayed (some parts were missing and some were transparent), but the whole temporal sequence of volumes can be visualized based on the results of a pre-processing process (including a classification step). The main difficulty in

the case of bioprosthesis is the high level of motion artifacts. The motion artifacts of stent (high grey level, similar with calcifications in visualization result) often alter the visual rendering of thin leaflets (low grey level).

In the case of native valve, defect has been found in motion compensation. The pose of the virtual camera was roughly linked to the moving aortic root. This is mainly because the tricuspid annulus was marked interactively. Unlike the metal stent, the tricuspid annulus can be confounded with the base of leaflets. Moreover, tricuspid annulus deforms over the different phases. This also might affect the virtual camera setting.

5.4 CONCLUSION

Visualization could be used to overcome the difficulties encountered for the segmentation of MDCT images, and to fully render the information included in the 3D+T CT volume images to improve and accelerate the general understanding of vascular pathologies and allows a more realistic preoperative planning of surgery/interventional procedure.

We retained direct volume ray casting technique to visualize 3D+T CT volumes, by considering pre-processing and rendering issues. Moreover motion compensation was required to control, during the cardiac cycle, the pose of the virtual camera within the moving aortic root. The input of the visualization process was provided by the output of the pre-processing step.

Preliminary results showed that the proposed spatio-temporal visualization provides additional information on the dynamical behavior of bioprosthesis structures during cardiac cycle. These visualizations could be used to improve the understanding of the failure mechanism and facilitate the medical decision about the therapeutic option.

Although our work was mainly dedicated to aortic valve bioprothesis, we also reported first results obtained on native valve to illustrate the interest of the proposed methodology.

REFRENCES

[5.1]. Bloomfi eld P , Wheatley DJ , Prescott RJ , Miller HC . Twelve-year comparison of a Bjork-Shiley mechanical heart valve with porcine bioprostheses . N Engl J Med 1991 ; 324 : 573 – 579 .

[5.2]. Hammermeister KE, Sethi GK, Henderson WG, Oprian C, Kim T, Rahimtoola S. A comparison of outcomes in men 11 years after heart-valve replacement with a mechanical valve or bioprosthesis. Veterans Affairs Cooperative Study on Valvular Heart Disease . N Engl J Med 1993 ; 328 : 1289 – 1296 .

[5.3]. R. A. Drebin, L. Carpenter, and P. Hanrahan. Volume Rendering. In SIGGRAPH '88: Proceedings of the 15th annual conference on Computer graphics and interactive techniques, pages 65–74, New York, NY, USA, 1988. ACM.

[5.4]. Smelyanskiy, M. Holmes, D. Chhugani, J Larson, A. Mapping High-Fidelity Volume Rendering for Medical Imaging to CPU, GPU and Many-Core Architectures Visualization and Computer Graphics, IEEE Transactions Nov 2009 Vol15(6): 1563 - 1570

[5.5]. Xiong Z., Wu X., Cheng S., and Hua J.. Lossy-to-lossless compression of medical volumetric data using three-dimensional integer wavelet transforms. Medical Imaging, IEEE Transactions on, 22(3):459–470, 2003.

[5.6]. Zheng Y, John M, Liao R. Automatic Aorta Segmentation and Valve Landmark Detection in C-Arm CT: Application to Aortic Valve Implantation. Medical Image Computing and Computer-Assisted Intervention – MICCAI 2010: 476-483

[5.7]. John M, Liao R. Zheng Y System to Guide Transcatheter Aortic Valve Implantations Based on Interventional C-Arm CT Imaging. Medical Image Computing and Computer-Assisted Intervention – MICCAI 2010 Lecture Notes in Computer Science Volume 6361, 2010: 375-382

[5.8]. Wald I, Slusallek P, Benthin C, and Wagner M. Interactive rendering with coherent raytracing. In Computer Graphics Forum/Proceedings of EUROGRAPHICS 2001, 153–164, 2001.

[5.9]. Abert O., Geimer M., Müller S.: Direct and fast ray tracing of NURBS surfaces. In Proceedings of the 2006 IEEE Symposium on Interactive Ray Tracing (2006), 161–168.

[5.10]. Reshetov A.: Faster ray packets-triangle intersection through vertex culling. In Proceedings of the 2007 IEEE/Eurographics Symposium on Interactive Ray Tracing (2007), 105–112.

[5.11]. Khan MF, Herzog C, Landenberger K, Maataoui A, Martens S, Ackermann H, Moritz A, and Vogl T.J. Visualisation of non-invasive coronary bypass imaging: 4-row vs. 16-row multidetector computed tomography. Eur Radiol (2005) 15:118–126

[5.12]. Şaylısoy S, Atasoy C, Ersöz S, Karayalçın K, Akyar S. Multislice CT angiography in the evaluation of hepatic vascular anatomy in potential right lobe donors. Diagn Interv Radiol 2005; 11:51-59

[5.13]. Meyer-Spradow, J. Ropinski, T. Mensmann, J. Hinrichs, K. Voreen: A Rapid-Prototyping Environment for Ray-Casting-Based Volume Visualizations Computer Graphics and Applications, IEEE Nov. 2005, Vol29 (6):6-13

[5.14]. Calhoun P S., Kuszyk B S., Heath D G., Carley J C., Fishman E K., Three-dimensional Volume Rendering of Spiral CT Data: Theory and Method. RadioGraphics, May 1999 , 19, 745-764.

[5.15]. Haigron P., Berre G. L., and Coatrieux J. L., “3-D navigation in medicine,” IEEE Eng. Med. Biol., vol. 15, pp. 70–78, Mar.-Apr. 1996.

[5.16]. Haigron P., Bellemare M. E., Acosta O., Göksu C., Kulik C., Rioual K., and Lucas A. Depth-Map-Based Scene Analysis for Active Navigation in Virtual Angioscopy. IEEE TRANSACTIONS ON MEDICAL IMAGING, NOVEMBER 2004 23(11): 1380-1390

[5.17]. Lathen G, Lindholm S., Lenz R., Persson A., and Borga M., Automatic Tuning of Spatially Varying Transfer Functions for Blood Vessel Visualization IEEE TRANSACTIONS ON VISUALIZATION AND COMPUTER GRAPHICS, DECEMBER 2012 18(12): 2345-2354

[5.18]. Andriole K. P., Morin R. L., Arenson R. L., Carrino J. A., Erickson B. J., Horii S. C., Piraino D. W., Reiner, B. I. Seibert J. A., and Siege E. l. Addressing the coming radiology crisis-the Society for Computer Applications in Radiology transforming the

radiological interpretation process (TRIP) initiative. Journal of digital imaging the official journal of the Society for Computer Applications in Radiology, 17(4):235–243, 2004.

[5.19]. Lundstrom C. and Persson A.. Characterizing visual analytics in diagnostic imaging. International Workshop on Visual Analytics, 2011.

[5.20]. Lindholm S. Ljung P. Lundstrom C., Persson A., and Ynnerman A. Spatial conditioning of transfer functions using local material distributions. Visualization and Computer Graphics, IEEE Transactions on, 16(6):1301–1310, nov.-dec. 2010.

[5.21]. Coatrieux J.L, Rioual K, Göksu C, Unanua E.,and Haigron P. Ray Casting With "On-the-Fly" Region Growing: 3-D Navigation Into Cardiac MSCT Volume. IEEE TRANSACTIONS ON INFORMATION TECHNOLOGY IN BIOMEDICINE, APRIL 2006 10(2): 417-420

[5.22]. Garcia M.P., Velut J., Boulmier D., Leclercq C., Garreau M., Haigron P., Toumoulin C., Coronary Vein Extraction in MSCT Volumes Using Minimum Cost Path and Geometrical Moments. IEEE JOURNAL OF BIOMEDICAL AND HEALTH INFORMATICS, MARCH 2013 17(2): 336-345

[5.23]. Lundstrom C. and Persson A.. Characterizing visual analytics in diagnostic imaging. International Workshop on Visual Analytics, 2011.

[5.24]. Lindholm S. Ljung P. Lundstrom C., Persson A., and Ynnerman A. Spatial conditioning of transfer functions using local material distributions. Visualization and Computer Graphics, IEEE Transactions on, 16(6):1301–1310, nov.-dec. 2010.

[5.25]. Frangi AF, Niessen WJ, Viergever MA. Three-dimensional modeling for functional analysis of cardiac images: A review. IEEE Trans on Medical Imaging. 2001;20(1):2–25.

[5.26]. Velut J., Toumoulin C., and Coatrieux J.L., 3D coronary structure tracking algorithm with regularization and multiple hypotheses in MRI, in Proc. IEEE Int. Biomed. Imag. Nano Macro Symp., Apr. 2010, 37–40.

[5.27]. Wong W. and Chung A., Augmented vessels for quantitative analysis of vascular abnormalities and endovascular treatment planning, IEEE Trans. Med. Imag., 25(6): 665–684, Jun. 2006.

[5.28]. Wang Y, Li J, Chen S. A Novel Method of Extracting 3D Blood Vessel Images Axis Based on Energy Constraint Equation Journal of Computational Information Systems 7:4 (2011) 1319-1327

[5.29]. Lohou C., Bertrand G. A 3D 12-subiteration thinning algorithm based on P-simple points. Discrete Applied Mathematics 139:1 – 3(2004) 171 – 195

[5.30]. Lohou, C. Dehos, J. Automatic Correction of Ma and Sonka's Thinning Algorithm Using P-Simple Points. Pattern Analysis and Machine Intelligence, IEEE Transactions 32:6 (2010) 1148-1152

[5.31]. Yaniv, Z. Joskowicz, L. Long bone panoramas from fluoroscopic X-ray images. IEEE TRANSACTIONS ON MEDICAL IMAGING, 23(1): 26-35, JAN 2004

[5.32]. Schaap, M.; Metz, C.; van Walsum, T.; van der Giessen, A.; Weustink, A.; Mollet, N.: Standardized Evaluation Methodology and Reference Database for Evaluating Coronary Artery Centerline Extraction Algorithms. Medical Image Analysis, 2009, 13/5, 701-714

VI CONCLUSION AND PERSPECTIVES

Although echocardiography remains the gold standard for functional analysis of bioprosthesis failure, in the last years an increasing number of groups are looking with particular interest at CT images for anatomo-morphological analysis of the aortic valve. In this thesis, we proposed a new approach for the morphological analysis of degenerated aortic valve bioprosthesis based on CT images segmentation and visualization.

Different methods for noise reduction were tested and proposed. 3D reconstruction of bioprostheses components was achieved using stick based region segmentation methods. Noise reduction obtained by improved stick filter showed best results in terms of signal to noise ratio compared to anisotropic diffusion filters. The segmentation methods applied to the best phase of in-vivo images allowed 3D bioprosthetic leaflets reconstruction. Explanted bioprostheses CT images were also processed and used as reference. Qualitative analysis revealed a good concordance between the in-vivo images and the bioprostheses alterations. Results from different segmentation methods were compared by means of volumetric criteria and discussed. Volume rendering and motion compensation techniques were also applied to visualize different phases of the CT data set. A first approach for spatio-temporal visualization of 3D+T CT images of valve bioprosthesis has been proposed.

Our preliminary results suggest the feasibility to enhance and visualize aortic bioprosthesis leaflets by applying the proposed processing methods for noise reduction and segmentation to preoperative CT images. Because today such visualization of bioprosthesis leaflet morphology is intricate or impossible with other imaging techniques, we believe that in the next future high resolution CT images exploration may play an important role to improve the understanding of the dysfunction mechanism in patients with a degenerated aortic valve bioprosthesis.

Additional studies are necessary to improve and validate these results. Subject to further validation of proposed image processing methods, presumably accompanied by an adaption of acquisition protocols, the analysis of the degeneration in bioprosthesis could be considered in larger series. In addition, 3D reconstruction and description of bioprostheses structures could represent in next future an important tool to improve the planning of the valve-in-valve procedure or could be used to preoperatively simulate this kind of procedure.

Appendix 1 - Figures legend

Fig 2.1: Second generation bioprostheses.....8

Fig 2.2: Third generation bioprostheses. 9

Fig 2.3: Stentless bioprostheses.....10

Fig 2.4: Aortic homograft.....11

Fig 2.5: Mechanisms of bioprosthesis failure.....14

Fig 2.6: Leaflet tears in degenerated porcine bioprosthesis.....16

Fig 2.7: Edwards Sapien transcatheter valve deployed into a bioprosthesis.....20

Fig 2.8: Medtronic CoreValve transcatheter valve.....21

Fig 2.9: Edwards Sapien transcatheter valve.....21

Fig 2.10: Valve-in-valve procedure using Edwards Sapien transcatheter valve. Intraoperative fluoroscopy during (A) device positioning, (B) valve deployment and (C) control aortography.....21

Fig 2.11: Bioprosthesis different diameters change according to valve type.....22

Fig 2.12: Drawings show helical projections from MDCT. A, Detectors follow 3D helical path, with table advancing at constant speed while gantry is rotating. Tube emits X-ray radiation (yellow) that is recorded by detectors. Resulting set of projections has helical configuration in space. B, Images are reconstructed from projection data by linear interpolation from projections closest to image plane. Advanced algorithms correct for cone-beam geometry.....26

Fig 2.13: Drawings show that relation of table movement with respect to gantry rotation is described by beam pitch. A, Pitch of 0.5:1 indicates 50% overlap in projection data. B, Pitch of 1:1 indicates neither overlap nor gap in data. C, Pitch of 1.5:1 indicates 50% gap in data.....27

Fig 2.14: Temporal window for reconstruction from projection data is approximately 250 msec. Drawing shows that center of window can be located anywhere during heart cycle. Left box has its center at 10% of R-R interval, which is during systole. Right box has its center at 70% of R-R interval, which is during diastole and is most common motion-free imaging temporal window for heart.....30

Fig 2.15: Drawings show two types of retrospective reconstruction algorithms. A, In partial scanning algorithm, continuous segment of projection data at single heartbeat is used to reconstruct image. B, In segmented adaptive algorithm, different segments of projection data from same phase of cardiac cycle at successive heartbeats are used to reconstruct image. Cardiac cycle and gantry rotation must not be synchronized for different segments to

cumulatively cover large enough range of projection angles to reconstruct image from data.....32

Fig 2.16: Bioprosthetic aortic valve analysis from MSCT data.....34

Fig. 3.1: Two MSCT slices of aortic valve prosthesis with high level noise, showing stent (A), leaflets (B), calcification (C) and pannus (D).....39

Fig 3.2 Noises in MSCT images of bioprosthesis. We can see noise and metal artifacts in both images. Image B shows strong directional noise.....40

Fig 3.3: Curve of Tukey's Biweight function.....50

Fig. 3.4 Radiological images of bioprostheses with complete metallic stent (A and B) and incomplete metallic stent (C).....55

Fig. 3.5: Regions of interest: a slice in a classical cubic ROI (A), Cylindrical (B) and conformational (C) stent defined ROI, and illustration of the corresponding CT observations (D and E respectively) within one of the original CT slices.....56

Fig 3.6: Circle of the metallic stent used to determine the features of the conformational ROI.....58

Fig 3.7: Slices form MSCT data sets: HER (A), MAG(B), BOU(C) and DAV(D).....60

Fig. 3.8: impulse noises amplified during diffusion filtering.....63

Fig. 3.9: 7 voxels-length 2D symmetric sticks set.....66

Fig. 3.10: 4 voxels-length 2D asymmetric sticks set.....66

Fig. 3.11: Sticks perform in thin structure (SM /SMC)(A) and in tubular structure (Sm / SmC)(B).....69

Fig. 3.12: The flowchart of classification of different structures in images.....70

Fig. 3.13 : Case n°1 – explanted pericardial bioprosthesis showing a calcified leaflet prolapse. 76

Fig. 3.14: Case n°2 – explanted porcine bioprosthesis showing leaflet tear and calcified pannus. 76

Fig. 3.15： Case n°3 – explanted porcine bioprosthesis showing one leaflet calcification.....77

Fig. 3.16： Case n°4 – explanted porcine bioprosthesis showing leaflet infection.....77

Fig. 3.17: Examples of original images: HER (A), MAG (B), BOU (C) and DAV (D). Regions located in the red square include the bioprosthesis.....79

Fig. 3.18: Filtering of case 1-4 (original image and results obtained with the 7 different filters).....80-82

Fig. 3.19: SNR of original images and results after denoising with the different filters..83

Fig. 3.20: SNR according to the number of iterations in the case n°2 - MAG.....85

Fig. 4.1: Application example of Interactive Region Growing method by 3D slicer software. 100

Fig. 4.2: Regions with large surface curvature (indicated by red arrows).....103

Fig. 4.3 : Flowchart of stick region growing.....105

Fig. 4.4: Examples of segmented CT-Slices obtained in case 1 - HER: metallic stent, calcifications and leaflets are indicated by green, brown and purple border respectively....109

Fig. 4.5: Visualization of the segmentation results obtained in case 1 - HER. Explanted bioprosthesis (A), ex-vivo segmented bioprosthesis (B), in-vivo segmented bioprosthesis with methods IRG (C), Stick RG (D) and SES (E). The commissure lost is indicated with blue circle and good leaflets cooptation with white arrows.....110

Fig. 4.6: Examples of segmented CT-Slices obtained in case 3 - BOU: metallic stent, calcifications and leaflets are indicated by green, brown and purple border respectively....111

Fig. 4.7: Examples of segmented CT-Slices obtained in case 4 - DAV: metallic stent, calcifications and leaflets are indicated by green, brown and purple border respectively....111

Fig. 4.8: Visualization of the segmentation results obtained in case 3 – BOU (A) and 4 – DAV (B). Explanted bioprosthesis (a), segmented ex-vivo bioprosthesis (b), segmented in-vivo bioprosthesis with methods IRG (c) and Stick RG (d).....112

Fig. 4.9: Visualization of the segmentation correction performed in case 3 - BOU. Explanted bioprosthesis (A), ex-vivo segmented bioprosthesis (B), in-vivo segmented bioprosthesis with methods IRG (C), Stick RG with correction (D) and SES with correction (E).....113

Fig 4.10: Visualization of the segmentation correction performed in case 4 - DAV. Explanted bioprosthesis (A), ex-vivo segmented bioprosthesis (B), in-vivo segmented bioprosthesis with methods IRG (C), Stick RG with correction (D) and SES with correction (E).....114

Fig. 4.11: Examples of segmented CT-Slices obtained in case 2 - MAG. Original slices (A), results of segmentation performed by IRG (B), Stick RG (C) and SES (D). Metallic stent, calcifications and leaflets are indicated by green, brown and purple border respectively..115

Fig 4.12: Visualization of the segmentation results obtained in case 2 - MAG (Front, i.e. view from aorta and Back, i.e. view from left ventricle). Explanted bioprosthesis (A), segmented ex-vivo bioprosthesis (B), in-vivo segmented bioprosthesis by IRG (C), Stick RG (D) and SES (E). Calcified pannus (indicated by black arrows) and leaflet tears (indicated by green arrows) are observed.....116

Fig 4.13: Volume analysis of bioprosthesis components.....118

Fig 4.14: Stent based correction of leaflet volume in case HER.....119

Fig 5.1: Volume rendering by ray tracing model.....131

Fig 5.2: Aortic valve visualization.....137

Fig 5.3: Motion artifact between slices during systole.....138

Fig 5.4: Different motion artifacts on stent and vascular lumen.....139

Fig 5.5: CT slice after preprocessing (A) and the region of interest including aortic valve (B). By dilating the region of voxels classified as leaflets (C), we get a region including leaflets (D).....140

Fig 5.6: Standard volume rendering of aortic valve bioprothesis.....142

Fig 5.7: TFs used in a case of bioprosthesis and the result of volume rendering.....144

Fig 5.8: TFs used in a case of native valve and the result of volume rendering.....145

Fig 5.9: The direction orthogonal to the complete metal stent plane (A) and the position of virtual camera (B). Coronaries are marked by blue arrows.....147

Fig 5.10: Direction defined by metal parts of incomplete metal stent (A), which is actually directed towards the center of the valve prosthesis (B), and the position of the camera (C).....148

Fig 5.11: Pose of the virtual camera and the centerline.....149

Fig 5.12: Voxels located in tricuspid annulus (A -C). Points at the top of commissure of leaflets (A) and at the bottom of leaflet determine the direction orthogonal to tricuspid annulus (D) and the position of virtual camera (E). 151

Fig 5.13: Visualization of the 3D+T data set in HER case: 4 systole volumes (R_1 - R_4) and 6 diastole volumes (R_5 – R_{10}). The commissure lost and the good leaflets cooptation can be seen in rendering. Visualization results obtained without gray level normalization and with rough motion compensation (R_{1bis} – R_{10bis}).....154

Fig 5.14: Visualization of the phases in YVE data set: 3 systole volumes (1-3) and 5 diastole volumes (4-8). The motion of one leaflet is altered due to calcifications on it. R_{1bis} – R_{8bis} without motion compensation and gray level normalization are comparison group.....156

Appendix 2 - Tables legend

2.1: Grading of calcification in bioprostheses degeneration.....15

2.2: Grading of tears in bioprostheses degeneration.....15

2.3: Grading of pannus in bioprostheses degeneration.....17

2.4: Measure variations in different types of bioprostheses with 23 mm labeled valve size 28

3.1**:** Possible patterns in 2*D* and 3*D*, depending on the value of the eigenvalues (H=high, L=low, N=noisy, usually small). The eigenvalues are ordered as: $|\lambda_1| \leq |\lambda_2| \leq |\lambda_3|$ 46

3.2: Possible structures depending on *MG* values along S_M, S_{MC}, S_m and S_{mC} sticks (H=high, L=low).....70

3.3: Echocardiographic assessment and intra-operative evaluation of failure in studied bioprostheses.....75

3.4: Image resolution parameters of in-vivo (IV) and ex-vivo (EV) acquisitions.....78

3.5: SNR of original images and resulting images.....82

5.1. Image resolution parameters of MSCT data sets.....152

Appendix 3 - Thesis related publications

Wang Q., Ruggieri G. V., Verhoye J.P., Lucas A., Miguel B., Shu H., Luo L., and Haigron P., 'Method for Narrow Vascular Structure Segmentation in Ct Data', in RITS 2011 (Colloque National Recherche en Imagerie et Technologies pour la Santé), Rennes, France 2011.

Ruggieri VG, **Wang Q**, Esnault S, Madeleine R, Luo L, Leguerrier A, Verhoye JPh, Haigron P. Analysis of degenerated aortic valve bioprosthesis by segmentation of preoperative CT images. IRBM (Journal of Biomedical Engineering and Research). 2012 Nov; 33:287-97.

Ruggieri VG, **Wang Q**, Madeleine R, Esneault S, Haigron P, Verhoye JP. CT scan images processing by semi-automatic segmentation to analyse aortic bioprostheses. 47th Congress of the European Society for Surgical Research; 2012 Nov; Lille (France). p.67-76.

Ruggieri VG, Anselmi A, **Wang Q**, Esnault S, HaigronP, Verhoye JPh. Computed Tomography Image Processing to Detect the Real Mechanism of Bioprosthesis Failure. Implication for valve-in-valve implantation. J Heart Valve Dis. 2012 Mar; 22(2):236-238.

Ruggieri VG, Haigron P, **Wang Q**, Esnault S, Madeleine R, Heautot JF, Leguerrier A, Verhoye JPh. CT-scan images preprocessing and segmentation to improve bioprosthesis leaflets morphological analysis. Medical Hypotheses. 2013 Jul;81(1):86-93.